Simulation of Catalyst Layer and Membrane Durability in Polymer Electrolyte Membrane Fuel Cells under Real-World Vehicle Operation

by

Mohammad Soroush Shojayian

M.Sc. (Mechanical Engineering), Amirkabir University of technology, 2018

B.Sc. (Mechanical Engineering), University of Tehran, 2015

Thesis submitted in Partial Fulfillment of the

Requirements for the Degree of

Doctor of Philosophy

in the

School of Mechatronic Systems Engineering

Faculty of Applied sciences

SIMON FRASER UNIVERSITY

Spring 2024

Declaration of Committee

Name:	**Mohammad Soroush Shojayian**
Degree:	**Doctor of Philosophy**
Title:	**Simulation of Catalyst Layer and Membrane Durability in Polymer Electrolyte Membrane Fuel Cells under Real-World Vehicle Operation**
Committee:	**Chair: Ahad Armin** Lecturer, Mechatronic Systems Engineering
	Erik Kjeang Supervisor Professor, Mechatronic Systems Engineering
	Patrick Palmer Committee Member Professor, Mechatronic Systems Engineering
	Gary Wang Examiner Professor, Mechatronic Systems Engineering
	Nadia Yousfi Steiner External Examiner Professor, Energy department University of Franche-Comté

Abstract

Addressing climate change has become a prominent focus, leading to the implementation of regulations aimed at reducing greenhouse gas emissions by fossil fuel vehicles. While the polymer electrolyte membrane fuel cells (PEMFCs) have been proven as a promising candidate to replace internal combustion engines, their commercialization has been impeded by high costs and uncertainties related to their durability in vehicle applications. In this thesis, degradation models for membrane and cathode catalyst layer of PEMFCs are developed separately due to their distinct degradation mechanisms to study the possibilities of enhancing the overall fuel cell lifetime with respect to fuel cell cost and hydrogen consumption. Widely calibrated with experimental data from accelerated stress test cycles, the catalyst degradation model is utilized to study the degradation of a fuel cell transit bus under use-level conditions in the city of Victoria, B.C., Canada. The model is coupled with the performance degradation by calculating the voltage degradation and updating the polarization curve. The recorded bus drive cycle is converted to a cell voltage profile considering fuel cell stack specifications and vehicle dynamics. Next, the membrane degradation is modeled considering the fibrillar morphology of the membrane and is calibrated with experimental stress test results. Coupled with the catalyst degradation model to include the voltage drop impact over time, the membrane degradation model is used to estimate the lifetime under the same drive cycle. The reduction in the stack size and temperature were found to significantly increase the fuel cell lifetime. Next, a number of degradation mitigation strategies are evaluated such as lowering the cell temperature and hybridizing with the battery. A multi-objective optimization is implemented using the genetic algorithm to optimize fuel cell lifetime and mitigate the rise in hydrogen consumption resulting from hybridization. It is discovered that hybridization leads to more durable stacks and reducing their cost; however, it comes at the expense of increased hydrogen consumption. Finally, following a comparison between the results of the present modeling framework and a realistic transit bus operation, a favorable agreement is observed. The modeling framework can be used to estimate the fuel cell lifetime and hydrogen consumption and optimize stack based on these considerations.

Keywords: Fuel cell; Catalyst Layer; Membrane; Durability; Transit Bus Operation

Acknowledgements

First and foremost, I am profoundly grateful to my senior supervisor, Prof. Erik Kjeang, for his unwavering guidance, expertise, and invaluable support throughout my research journey. His insightful feedback, encouragement, and dedication have been instrumental in shaping this work and pushing me to achieve my full potential. This research would not have been possible without his mentorship, and I am truly fortunate to have had the opportunity to work under his supervision. Then, I would like to express my gratitude toward my labmates at SFU fuel cell research lab (FCReL) with whom I had amazing and memorable time. Specifically, I am truly grateful to Dr. Heather Baroody, Dr. Narinder Singh Khattra and Dr. Mohamed El Hannach for providing technical details and insights into the modeling frameworks. I also thank Dr. Mohsen Mazrouei Sebdani for his collaboration and sharing the results from his cross pressure accelerated mechanical stress tests. I am also deeply grateful to Dr. Patrick Palmer, a valued member of my committee, for his insightful guidance and constructive feedback throughout my research journey.

This research was supported by the Natural Sciences and Engineering Research Council of Canada, Canada Research Chairs, and Simon Fraser University Community Trust Endowment Fund. I am grateful to these funding agencies. This work also made use of the 4D LABS core facility at Simon Fraser University (SFU) supported by the Canada Foundation for Innovation (CFI), British Columbia Knowledge Development Fund (BCKDF), and Pacific Economic Development Canada (PacifiCan). I express my gratitude toward the 4D labs staff members for their training and for providing access to the facilities including ultramicrotomy and electron microscopes.

Finally, I would like to thank my parents, my brother, and my wife. I would not have come to this point without their support.

Table of Contents

List of Tables

List of Figures

List of Acronyms

AST	Accelerated Stress Test
AMDT	Accelerated Membrane Durability Test
AMST	Accelerated Mechanical Stress Test
BOL	Beginning of Life
CCM	Cathode Coated Membrane
DMFC	Direct Methanol Fuel Cell
DOE	Department of Energy
EOT	End of Test
FCEV	Fuel Cell Electric Vehicle
LPL	Lower Potential Limit
OCV	Open Circuit Voltage
PEMFC	Polymer Electrolyte Membrane Fuel Cell
PFSA	PerFluoroSulfonic Acid
PITM	Platinum In The Membrane
RH	Relative Humidity
SHE	Standard Hydrogen Electrode
SOFC	Solid Oxide Fuel Cell
SU/SD	Start-Up/Shut-Down
UPL	Upper Potential Limit

Chapter 1: Introduction

1.1. Motivation

Reducing greenhouse gas emissions from the transportation sector is vital to mitigate the detrimental impacts of climate change. To achieve a substantial reduction in greenhouse gas emissions in the coming years, governments across different countries have implemented regulations to enforce a ban on the sales of internal combustion engines vehicles within the next 20-30 years [1], [2]. As a result, a focused endeavor has been made to investigate clean energy technologies as substitutes for conventional combustion engines. In this pursuit, batteries and fuel cells have emerged as particularly promising alternatives, demonstrating great potential in the ongoing search for sustainable energy solutions. While utilizing batteries in hybrid gasoline-electric vehicles and fully electric vehicles for light duty applications shows promise, their adoption for heavy duty vehicles is less prevalent due to limitations concerning energy density, charging infrastructure, and cost [3]. Hydrogen-powered fuel cell electric vehicles (FCEVs) present a promising zero-emission solution for heavy duty vehicles, offering the potential for higher energy density compared to batteries. There are various types of fuel cells, each of which is better suited for specific applications depending on their characteristics and capabilities. The polymer electrolyte membrane fuel cell (PEMFC) is widely recognized as one of the most prevalent types of fuel cells. It generates electricity by hydrogen oxidation and oxygen reduction through two catalysts, which are kept apart by a perfluorosulfonic acid polymer membrane. In contrast to the PEMFC, other fuel cell types employ different fuels and components. For example, direct methanol fuel cells (DMFC) utilize methanol as the fuel, while solid oxide fuel cells (SOFC) use ceramics for the electrodes and electrolyte. FCEVs typically utilize PEMFCs due to their advantageous features, including high power density and low operating temperatures [4]. Despite their advantages, broad utilization of PEMFCs in FCEVs has faced challenges due to factors such as low durability, high cost, and limited hydrogen infrastructure. These impediments have hindered the widespread commercialization of PEMFC-based FCEVs thus far.

Ensuring the durability of heavy duty fuel cell systems is extremely critical due to their extended operational lifespan. According to the target set by the US Department of Energy (DOE), fuel cell transit buses were expected to operate for 18,000 hours by 2016. However, the DOE's ultimate lifetime target for transit buses was raised to 25,000 hours by the year 2020 [5]. The major degradation processes that significantly limit the lifetime of fuel cells are membrane

degradation, cathode catalyst degradation, and carbon corrosion [5]. Among these, cathode catalyst degradation alone accounts for approximately 30-40% of fuel cell failures [6]. The catalyst degradation was found to be more significant than the gas diffusion layer (GDL) degradation under normal operation [7]. The cathode also exhibits more substantial degradation than the anode, primarily due to the higher potentials at the cathode [8]. The observed larger platinum particle growth at the cathode is a clear indication of the higher degradation levels experienced at the cathode [9]. Carbon-supported platinum catalysts are widely employed in PEMFC applications. Under harsh operating conditions such as high cell voltages and temperatures, platinum gradually undergoes degradation mechanisms, leading to a reduction in the activity of the cathode catalyst and a subsequent decline in fuel cell performance. Platinum degradation processes include platinum dissolution and redeposition, as well as the diffusion and migration of platinum ions within the ionomer and their transfer into the membrane. Platinum dissolution refers to the conversion of platinum into ions, while redeposition involves the subsequent deposition of those ions back onto the platinum surface. The dissolved platinum ions move within the ionomer through diffusion and migration mechanisms. Some of these ions may eventually enter the membrane and be deposited there [10]. While electrocatalyst degradation (i.e., platinum degradation) is the dominant degradation mechanism at lower potentials (which are more commonly encountered during vehicle operation), carbon corrosion has been observed to occur at high potentials, typically above the open circuit voltage (OCV) [11], [12]. Carbon corrosion gives rise to the detachment of platinum particles, resulting in the separation of platinum particles from the carbon support. After detachment from the carbon support, the separated particles have the propensity to reattach to the remaining particles that are still connected to the carbon support. This reattachment process is known as coagulation [13]. Figure 1.1 shows a schematic of the catalyst degradation mechanisms.

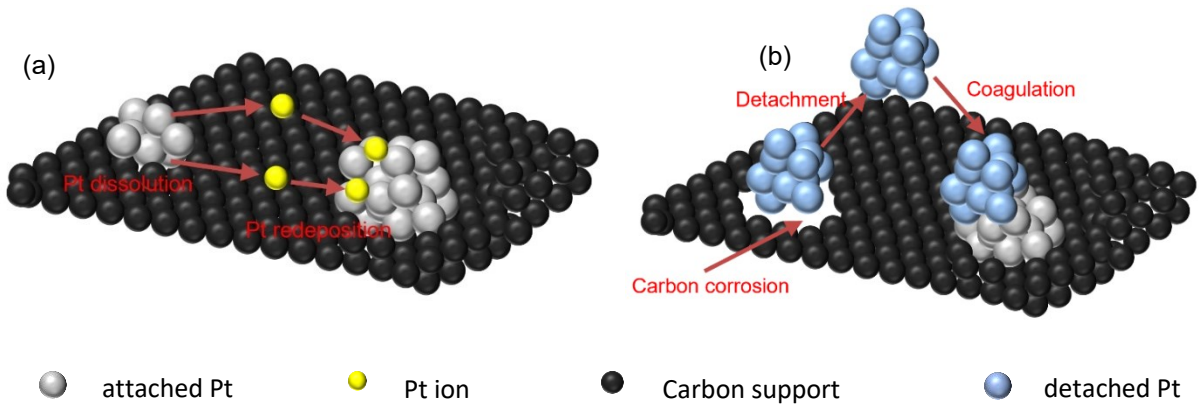

Figure 1.1: Schematic representation of platinum degradation mechanisms. (a) Platinum dissolution and redeposition through electrocatalyst degradation. (b) Platinum detachment and coagulation due to carbon corrosion.

Membrane degradation is also recognized as another detrimental phenomenon, frequently resulting in fuel cell failure. The performance of the membrane is significantly impacted by the interaction of various progressive degradation phenomena, ultimately resulting in a decline in membrane integrity. Membrane failure is identified through various phenomena, with perforation, cracks, and pinholes being among the most common occurrences. These issues arise as a result of accumulated membrane degradation, ultimately leading to significant hydrogen crossover [14].

Platinum degradation, carbon corrosion and membrane degradation have been subject to extensive theoretical and experimental research in the past decades. To streamline the degradation testing process and minimize testing time, accelerated stress tests (ASTs) have been developed and widely utilized. These tests are designed to simulate and accelerate degradation mechanisms, which would typically take several years to occur under normal operating conditions. ASTs involve subjecting the system to severe stress cycles that are specifically designed based on extreme operating conditions. These stress cycles are carefully designed to simulate and intensify the effects of harsh conditions on the system, allowing for accelerated degradation and assessment of performance under challenging conditions [15], [16].

1.2. PEMFC fundamentals

PEMFCs generate electrical energy by initiating an electrochemical reaction between hydrogen and oxygen, which allows them to convert chemical energy into usable power. This reaction occurs within the fuel cell, with hydrogen undergoing oxidation at the anode, resulting in the production of protons and free electrons. The protons move through a polymer electrolyte membrane, which serves as an electronically insulating but proton-conducting medium while the electrons are transferred through an external electrical circuit to generate power. The perfluorosulfonic acid (PFSA) ionomer membrane, commonly known as Nafion, is the state-of-the-art membrane material typically employed in PEMFC applications. This membrane material, developed from perfluorosulfonic acid, has been proven to be highly effective and is widely used in the field of PEMFC technology. At the cathode side of the fuel cell, oxygen undergoes reduction by combining with the migrated protons and electrons, leading to the formation of water and the release of heat as byproducts. The main and primary function of both the anode and cathode catalyst layers is to accelerate the hydrogen oxidation reaction (HOR) and oxygen reduction reaction (ORR) by reducing the activation energy required for these reactions to occur. Platinum has been widely recognized as the most optimal catalyst material for PEMFCs to date. It exhibits excellent electrochemical activity and stability, making it highly effective in facilitating HOR and ORR. Due to the naturally slower reaction rate of the ORR compared to the HOR, it is recommended to increase the platinum loading in the cathode catalyst. By doing so, a higher concentration of platinum is available to facilitate the ORR and compensate for its slower kinetics. Platinum nanoparticles are typically dispersed and supported on larger carbon nanoparticles. This configuration facilitates increased surface area and improved catalytic activity, as well as enhanced stability and durability of the platinum catalyst in PEMFCs. The ionomer, an essential component of catalyst layers, plays a crucial role by providing a medium for the movement of protons. It acts as a binder for the catalyst ingredients, contributing to the stability and integrity of the catalyst layer. Additionally, the ionomer facilitates water transport within the catalyst, further enhancing its functionality [15], [17]. A schematic illustrating the operation of a PEMFC is depicted in Figure 1.2.

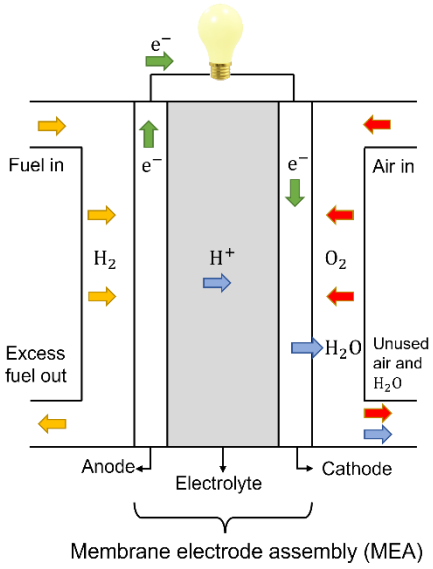

Figure 1.2: A schematic representation of the PEMFC operation.

The electrochemical reactions taking place in PEMFC are as follows.

$$\text{Anode: } H_2 \longrightarrow 2H^+ + 2e^- \qquad E^0 = 0 \text{ vs. SHE}$$

$$\text{Cathode: } \frac{1}{2}O_2 + 2H^+ + 2e^- \longrightarrow H_2O \qquad E^0 = 1.23 \text{ V vs. SHE}$$

$$\text{Overall: } H_2 + \frac{1}{2}O_2 \longrightarrow H_2O \qquad E^0_{cell} = 1.23 \text{ V} \qquad (1.1)$$

The uniform distribution of gases across the entire surface of the Membrane Electrode Assembly (MEA) is essential for maintaining optimal performance of a fuel cell. The GDL plays a critical role in achieving this by ensuring an even distribution of gases throughout the fuel cell system. GDLs are positioned between the electrodes (cathode or anode) and the flow field or bipolar plate. GDL not only allows for the effective removal of water vapor produced during the electrochemical reactions, but also serves as a conductive medium, enabling the flow of electrons through the electrode and the external circuit [18], [19]. Bipolar plates are essential components in maintaining the desired performance of PEMFCs. Positioned on one side of an MEA, a bipolar plate acts as the anode side for one cell. On the opposite side of the same bipolar plate, another MEA is positioned, forming the cathode side of the adjacent cell. This arrangement continues for multiple cells within a fuel cell stack, with bipolar plates alternating between anode and cathode

sides. Increasing the number of cells arranged in series within the stack will increase the voltage while enlarging the cell area leads to a higher current. In general, increasing the stack size will provide greater power output, making it suitable for demanding applications like heavy-duty automotive. The main functions of bipolar plates include providing electrical conductivity, facilitating gas distribution, water and thermal management, and offering mechanical support for individual cells within the fuel cell stack. By connecting the cells and ensuring efficient pathways for electron and gas flow, bipolar plates significantly contribute to the overall performance of the PEMFC system [20], [21].

1.3. Cathode catalyst layer degradation

The degradation of the MEA has an adverse impact on the durability and lifespan of PEMFCs. Gaining a comprehensive understanding of the degradation mechanisms associated with the MEA is crucial for developing effective strategies to address and minimize these issues. As discussed earlier, the degradation mechanisms in the membrane and cathode catalyst layer are more severe than those in GDL and anode, suggesting cathode and membrane lifetimes control and dominate the overall MEA lifetime. Therefore, the focus of this thesis will be given to the degradation mechanisms of the cathode and membrane to estimate the MEA lifetime. Cathode catalyst layer performance and durability is highly affected by platinum degradation and carbon corrosion. In the next sections, these phenomena will be discussed in detail.

1.3.1. Platinum degradation

As discussed earlier, under severe operating conditions characterized by high cell voltages and temperatures, platinum gradually undergoes dissolution, leading to a decrease in the activity of the cathode catalyst and a subsequent decline in the performance of the fuel cell. Extensive experimental and theoretical research has been conducted to investigate platinum degradation in PEMFCs. In a study by Wang et al. [9], fuel cell operation was analyzed for a duration of 2,250 hours at a current density of 160 $mA.cm^{-2}$. Transmission electron microscopy (TEM) analysis of the degraded samples indicated an increase in the average diameter of the platinum particles at the cathode, from 2.6 to 7.3 nm. These findings provide insights into the structural changes occurring during platinum degradation in fuel cell systems. However, conducting lifetime testing for fuel cells under real-world operating conditions can be a lengthy and expensive process. Therefore, ASTs have been designed to gather valuable data and

insights within a shorter timeframe, providing a more efficient and cost-effective means of evaluating the system's response to extreme operating conditions. These tests encompass subjecting the fuel cell to repetitive cycles of intense stress, deliberately designed to imitate the extreme operating conditions it may encounter. DOE has established standard AST protocols for various operating conditions, including load cycles and start-up/shut-down (SU/SD) cycles. These protocols aid in accelerating the degradation processes and offer valuable insights into the long-term performance and durability of fuel cells. For load cycles, the DOE recommends an AST protocol that involves alternating between an upper potential limit (UPL) and a lower potential limit (LPL) for a total of 30,000 cycles. The UPL and LPL values recommended by the DOE for load cycles are 0.98 V and 0.6 V, respectively. In this protocol, the fuel cell is subjected to 30,000 cycles, with each potential limit being held for a duration of 3 seconds [5]. For SU/SD cycles, the DOE suggests a protocol involving 5,000 cycles. In this combined SU/SD protocol, the fuel cell is held at each start-up or shut-down condition for 20 seconds [5]. This protocol is designed to replicate the repeated start-up and shut-down processes that the fuel cell may undergo in real-world applications. Messing and Kjeang [22] conducted experiments to investigate the impact of the SU/SD and load cycle protocols recommended by DOE on platinum degradation. They utilized a square voltage cycling profile with three LPLs and a fixed UPL with a 3-second hold at each level for the load cycle experiments. These experiments were performed at a temperature of 80℃ and a relative humidity (RH) of 90%. Additionally, a combined protocol that incorporated both SU/SD cycles and load cycles was employed. This combined protocol aimed to simulate the combined effects of catalyst and carbon support corrosion that are likely to occur during actual vehicle operation. The experimental data obtained from these tests were used to develop an empirical cathode lifetime model for each case. This model allowed them to estimate the catalyst lifetime based on a failure criterion of a 10% cell voltage drop.

Stoll et al. [23] captured X-ray images of the degraded cathode catalyst specifically during SU/SD cycles using a technique called X-ray computed tomography (XCT). By examining these images, they were able to observe the occurrence of carbon corrosion and establish a correlation between carbon corrosion and the drop in fuel cell performance. Pokhrel et al. [24] and White et al. [25] utilized XCT to investigate the structural changes of the catalyst during the degradation process. XCT allowed them to obtain detailed three-dimensional images of the catalyst, providing valuable insights into its deterioration and changes over time. Other researchers have conducted extensive studies utilizing a range of AST cycles. These include triangular wave potential cycles with different scan rates and square wave potential cycles with varying durations at the UPL and

LPL [26], [27], [28], [29], [30], [31], [32], [33]. They concluded that the cycle profile has a notable impact on the rate of degradation. Specifically, they found that potential cycles result in more pronounced degradation compared to a fixed steady state potential within a given experimental timeframe. Additionally, the use of square wave potential cycles was observed to induce significantly higher degradation compared to triangular potential cycles, when the UPL, LPL, and cycle period remained the same. Platinum particle growth was observed in all experiments, attributed to platinum dissolution/redeposition during potential cycle. Smaller platinum particles were found to be less stable and more susceptible to dissolution mechanisms compared to larger particles. Theoretically, smaller particles exhibited a lower dissolution equilibrium potential and higher dissolution rate. Consequently, dissolved platinum ions in the electrolyte tended to deposit onto larger particles, resulting in overall platinum particle growth. This phenomenon is known as Ostwald ripening. Figure 1.3 illustrates the growth of platinum particles observed after the test, comparing it to the initial state of the particles (the sample at BOL).

Research has also explored the degradation of fuel cells under vehicle drive cycles. Utilizing drive cycles based on real-world vehicle operations can provide more realistic insights compared to ASTs. Lin et al. [34] aimed to simulate an actual drive cycle by defining distinct vehicle operation periods, including starting, idle running, full power running, and overload running. They monitored voltage degradation over time at various current densities and developed an empirical model to quantify the rate of voltage degradation. Researchers have also focused on modeling the durability of fuel cells. Mayur et al. [35], [36] aimed to develop a comprehensive durability model by incorporating performance and degradation models. They utilized drive cycles specific to passenger vehicles and conducted fuel cell performance simulations, separating the performance and degradation aspects. Fuel cell durability was then estimated using an empirically derived degradation library. However, their model has certain limitations, including the omission of the direct impact of potential cycling on platinum degradation and reliance on an empirical degradation factor.

In order to comprehensively study fuel cell degradation, it is crucial to have a deep understanding of the underlying mechanisms that contribute to the degradation of fuel cell components. Darling and Meyers [37] were pioneers in this field and developed a mathematical model specifically focused on platinum degradation. Their model takes into account electrochemical and chemical reactions involved in the degradation process. It considers processes such as electrochemical platinum dissolution, platinum oxide film formation, and chemical dissolution of platinum oxide. By incorporating reaction rate equations and material

balance equations, the model can estimate parameters such as platinum loss, growth of platinum oxide thickness, and ionic platinum concentration in the solution over time. Additionally, the model enables the calculation of temporal changes in platinum particle size. Platinum degradation in fuel cells involves four key mechanisms: platinum dissolution, redeposition, detachment, and coagulation. Rinaldo et al. [13] developed mathematical models for each of these mechanisms to quantitatively analyze platinum degradation. Their models allowed them to calculate the amount of platinum lost through each degradation mechanism. Building on this work, Ao et al. [38] focused on the calculation of electrochemically active surface area (ECSA) loss in the cathode catalyst during potential cycling. They applied the fundamental methodology proposed by Rinaldo et al. [13] to estimate the ECSA loss caused by potential cycling, providing further insights into platinum degradation in fuel cells. Hiraoka et al. [39] introduced a dissolution/deposition model for platinum degradation, employing a zero-dimensional (0-D) approach. In their study, they utilized a platinum particle radius distribution obtained from experiments as the initial input for their model. They then estimated the growth of particle size by considering the Ostwald ripening phenomenon. Baroody and Kjeang [16] further developed the 0-D degradation model for the cathode electrode, building upon the Butler-Volmer kinetics introduced in [37]. In their work, they extended the model to account for both electrochemical and chemical platinum dissolution by incorporating the growth of platinum oxide on the platinum particles. By considering these dissolution and redeposition mechanisms, they were able to calculate the overall platinum degradation and quantify the temporal ECSA of the cathode electrode. A number of researchers have dedicated their efforts to developing a one-dimensional (1-D) platinum degradation model in the context of cathode degradation [10], [40], [41], [42], [43], [44], [45], [46]. To accomplish this, they integrated a straightforward 1-D platinum ion diffusion model into the existing platinum degradation model. This incorporation allowed for a more comprehensive understanding of the platinum degradation processes and provided insights into the spatial distribution of platinum degradation within the fuel cell system.

1.3.2. Carbon corrosion

During sustained operation at higher potentials above OCV, typically greater than 1.2 V, the carbon support in a fuel cell undergoes an oxidation process. This phenomenon is commonly observed during SU/SD, specifically at the cathode electrode which experiences the highest potentials. Water acts as the primary oxidant, initiating the oxidation reaction on the carbon support [47]. The carbon atoms react with the water molecules, resulting in the release of

electrons and the formation of carbon dioxide as the product of the oxidation process according to the following reaction.

$$C + 2H_2O \longrightarrow CO_2 + 4H^+ + 4e^- \qquad E^0 = 0.207 \text{ V vs. SHE} \qquad (1.2)$$

The oxidation of the carbon support material in the cathode of a fuel cell can have negative implications on performance. This oxidation process can result in a loss of the active catalyst surface area, leading to decreased electrochemical activity. Additionally, the electrical connectivity within the catalyst support structure in the electrode can be compromised. Furthermore, the oxidation of the carbon support can lead to changes in pore morphology and surface characteristics [23], [25]. This alteration of the pore structure can impact gas diffusion and mass transport within the electrode, affecting overall fuel cell performance [48], [49], [50].

1.4. Membrane degradation

The polymer electrolyte membrane used in fuel cells serves multiple important functions. Firstly, it acts as a barrier to prevent the mixing of reactant gases at the electrodes, a phenomenon referred to as gas crossover. This is crucial to maintain the proper electrochemical reactions and prevent undesirable side reactions. Additionally, the membrane should facilitate the conduction of protons across it. The membrane's ability to conduct protons is essential for the efficient operation of the fuel cell. Simultaneously, the polymer electrolyte membrane should exhibit electronic insulating properties. This is necessary to prevent the flow of electrons through the membrane, which could lead to short circuits and a drop in the fuel cell's performance [51]. Several phenomena are indicative of membrane failure in fuel cells. One of the most common signs is the occurrence of perforation, cracks, and pinholes in the membrane. These issues emerge as a result of accumulated membrane degradation over time. Membrane perforation, crack and pinholes refer to the formation of holes, breaches, fractures and gaps in the membrane material, which can compromise its integrity and allow the undesired mixing of reactant gases, particularly hydrogen crossover. Membrane degradation in fuel cells is primarily influenced by mechanical and chemical degradation mechanisms. Mechanical membrane degradation is characterized by cyclic stresses caused by the expansion and contraction of the membrane within the fuel cell. High humidity conditions lead to membrane swelling and in-plane compression, while low humidity conditions cause membrane shrinkage and in-plane tension. During dynamic vehicle operation, the membrane is exposed to fluctuating humidity and temperature conditions, resulting

in repeated water absorption and desorption cycles during fuel cell duty cycles. This leads to membrane swelling and contraction, which can contribute to its degradation over time [52], [53]. Fatigue, creep, and the formation of pinholes, cracks, and tears are commonly observed in fuel cell membranes subjected to mechanical stress and can significantly impact their lifespan and functionality [54], [55]. Extensive research has been dedicated to studying both ex-situ and in-situ mechanical degradation of fuel cell membranes. In-situ tests conducted under realistic operating conditions can be time-consuming, which has led to the development of accelerated mechanical stress tests (AMSTs). Huang et al. [56], for instance, investigated the impact of cyclic changes in RH on the mechanical properties of the membrane. They observed a notable decrease in the ductility of the membrane as a result of RH cycling. Other researchers have also focused on modeling the mechanical membrane degradation by employing various mechanical response models to assess its behavior. Tang et al. [57] introduced a linear elastic model to describe the mechanical behavior of the membrane, while Kusoglu et al. [58] utilized linear-elastic-plastic properties with isotropic hardening to study the hygrothermal stresses experienced by the membrane in situ. However, these approaches have limitations in accurately predicting the membrane's behavior, as they do not account for its inherent time-dependent response observed in experimental studies. To address this issue, Silberstein et al. [59] proposed elastic-viscoplastic models to investigate the influence of biaxial mechanical loading on the membrane. These models consider the time-dependent behavior of the membrane, allowing for a more comprehensive understanding of its mechanical response under varying conditions. Fatigue is recognized as a major consequence of mechanical membrane degradation. Khorasany et al. conducted experimental and numerical investigations to study the ex-situ and in-situ membrane lifetimes under the influence of fatigue effects [60], [61], [62]. They carried out a comprehensive study on membrane degradation by subjecting it to temperature and humidity cycles in the presence of an external tensile mechanical load. They employed a strained-based fatigue model, which was validated earlier with their experimental results, to analyze the effects of these factors on membrane degradation.

The DOE sets a recommended membrane lifetime target of 20,000 cycles specifically for pure mechanical degradation [5]. These cycles consist of a 2-minute operation at an RH of 150% followed by a 2-minute operation at an RH of 0%, both conducted at a temperature of 80℃. This target serves as a guideline for evaluating and designing membrane materials that can withstand mechanical stresses induced by humidity cycling, helping to ensure the durability and long-term performance of fuel cell membranes. In order to meet the membrane lifetime target, researchers

have introduced the concept of reinforced membranes. This involves incorporating a reinforcement layer, such as a fiber, into the membrane structure. The addition of the reinforcement layer enhances the mechanical strength and stability of the membrane, making it more resistant to degradation caused by mechanical stresses. One specific example of a reinforcement layer used in membrane technology is expanded polytetrafluoroethylene (ePTFE). ePTFE is a chemically inert material that is embedded within the membrane structure to enhance its mechanical strength; thus, the membrane can withstand an increased number of cycles [63], [64]. Ramani et al. [65] implemented an experiment to investigate the mechanical degradation of reinforced fuel cell membranes. The experiment involved intentionally introducing defects into the catalyst layers of the membrane. Subsequently, the membrane was exposed to a wet phase with high humidity (supersaturated wet at 150% RH) and a dry phase at a high temperature (80℃). These conditions were designed to simulate the operational stresses experienced by the membrane. Each fatigue test lasted for a duration of over 300 hours, which made the in-situ mechanical fatigue testing process time-consuming. The presence of the pre-existing defects allowed for accelerated testing, as the membrane's mechanical degradation could be observed within a shorter timeframe. However, it is worth noting that conducting AMSTs without these pre-existing defects would require several months to observe significant degradation, which is both costly and inefficient. Sadeghi Alavijeh et al. [66] conducted a modified version of the AMST to assess the durability of fuel cell membranes. They made adjustments to the test parameters by extending the duration of the dry cycle and increasing the temperature beyond the recommendations of DOE. Despite these modifications, the membranes demonstrated resilience and were able to withstand the test for an extended period of up to 20,000 RH cycles. This corresponds to a testing period of around eight consecutive weeks. To expedite the fatigue degradation process, researchers have proposed and developed pressure differential-accelerated mechanical stress tests (ΔP-AMSTs). These tests involve maintaining a varying range of pressure differentials between the anode and cathode of the fuel cell. By doing so, residual stress is induced in the membrane, leading to an accelerated fatigue degradation process of the membrane [63].

Chemical membrane degradation occurs as a result of the formation of radicals, such as hydroxyl (HO·) and hydroperoxyl (HOO·), which can react with the membrane materials. These radicals are generated during the electrochemical reactions that take place within the fuel cell. When these radicals come into contact with the membrane, they can initiate chemical reactions that lead to membrane thinning and the release of fluoride ions. This process is known as

chemical degradation and can have detrimental effects on the performance and durability of the fuel cell membrane [67]. The formation of radicals, such as hydroxyl (HO·) and hydroperoxyl (HOO·), in fuel cells can occur through various pathways. One common pathway is the decomposition of hydrogen peroxide, which can be generated as a by-product of the ORR during electrochemical reactions within the fuel cell. Additionally, the presence of crossover oxygen and hydrogen can also contribute to the chemical formation of hydrogen peroxide. The hydrogen peroxide generated at the electrodes can permeate the membrane and experience a Fenton reaction mechanism and decompose into radicals. The formed radicals may attack the membrane and cause main chain scission, side chain cleavage and unzipping which ultimately bring about membrane thinning and fluoride release from membrane [68], [69]. Indeed, the chemical degradation of membranes in fuel cells has been a subject of extensive research in the literature. Healy et al. [70] conducted experimental investigations to study the in-situ and ex-situ chemical degradation of a fuel cell membrane. They focused on monitoring the release of fluoride, which is a by-product of hydroxyl attack reactions that occur during membrane degradation. By analyzing the fluoride release, the researchers aimed to understand the extent and rate of chemical membrane degradation under different operating conditions. Similar to the catalyst ASTs, membrane degradation tests are conducted by subjecting the membrane to accelerated membrane durability tests (AMDTs). During AMDTs, the membrane is exposed to extreme operating conditions, such as high voltages, elevated temperatures, and low RH levels. Macauley et al. [71] implemented experimental evaluations on the lifetime of a membrane in fuel cell systems. They employed a series of AMDTs to simulate the effects of various stressors encountered during heavy-duty fuel cell transit bus operating conditions. These stressors included temperature, cell voltage, RH, and the presence of platinum in the membrane (PITM). By subjecting the membrane to these stressors and monitoring its degradation, the researchers aimed to understand the impact of each factor on membrane lifetime. Based on their findings, they developed an empirical lifetime model that could estimate the degradation rate and predict the overall durability of the membrane under real-world operating conditions experienced in transit bus applications. Several researchers have developed models to elucidate the mechanisms of membrane chemical degradation. Kundu et al. [72] focused on investigating the relationship between fluoride release and the OCV drop resulting from chemical degradation of the membrane. They developed an empirical model that aimed to establish a quantitative correlation between the amount of fluoride released and the corresponding OCV decrease. Shah et al. [73] proposed a transient model to investigate the formation of hydroxyl radicals and their concentration under different environmental conditions. Wong and Kjeang [74], [75] simulated the

process of fluoride release and membrane thinning during chemical membrane degradation by developing a 1-D numerical model. By considering the iron redox reaction, the model also explores the correlation between iron species and chemical membrane degradation. In order to prolong the membrane lifetime, several degradation mitigation strategies have been studied. One of the strategies involves the addition of cerium oxide (CeO_2) to the membrane. Cerium oxide is known for its catalytic properties and ability to scavenge radicals, making it effective in reducing the extent of chemical degradation [71]. By adding CeO_2 to the membrane material, it acts as a protective agent, inhibiting the attack of hydroxyl radicals and other reactive species on the membrane. The utilization of CeO_2-coated membranes has demonstrated notable improvements in membrane lifetime compared to conventional membranes, with enhancements of up to six times compared to conventional membranes [71]. Wong and Kjeang [76] developed a degradation model specifically for ceria-stabilized MEAs.

Fuel cell membranes undergo a combined degradation process involving both mechanical and chemical modes during real-world operating conditions. This is primarily attributed to the cyclic variations in RH and cell voltage that the membrane experiences over time. Numerous studies have focused on investigating the combined mechanical and chemical degradation of membranes [77], [78], [79], [80], showing aggravation and reduced test lifetime compared to the pure forms of degradation. Typical membrane failure modes are pinhole/fracture, crack initiation, crack development and edge cracks [78], [81]. While mechanical and chemical membrane degradations have been individually modeled in the literature, the modeling of membrane degradation due to the combined effects of these mechanisms is still an area of ongoing research and development. The challenge lies in capturing the complex interactions and synergistic effects between mechanical stresses and chemical reactions that occur simultaneously during fuel cell operation. Melchy and Eikerling [82], [83] proposed a methodology that treated the fuel cell membrane as a network of fiber bundles. They analytically calculated the times to fiber and bundle failure, taking into account only mechanical degradation mechanism. Building upon this work, Khattra et al. [84] developed a statistical model that coupled the effects of mechanical and chemical degradation using the fiber bundle methodology. This statistical model calculates the probability of fiber fracture within the membrane under specific operating conditions by considering factors such as mechanical stress, chemical degradation rates, and environmental variables (e.g., temperature, RH, and voltage).

1.5. Research objectives

Although the experiments and models discussed regarding cathode catalyst and membrane degradation offer valuable insights into the processes and mechanisms of fuel cell degradation, their applicability to real-world operating conditions is limited. These studies often focus on specific accelerated testing conditions or simplified laboratory setups, which may not fully capture the complexities of a fuel cell operating in a vehicle or other real-world applications. For instance, the theoretical cathode catalyst degradation models discussed earlier have predominantly concentrated on investigating the cathode degradation under AST cycles, rather than real-world vehicle operating conditions or drive cycles. These models have been instrumental in providing insights into the catalyst degradation mechanisms and the factors influencing its performance and lifespan under controlled laboratory conditions. However, it is important to acknowledge that the operating conditions experienced by fuel cells in actual vehicles can differ significantly from those simulated in AST cycles. Additionally, while membrane degradation experiments and models have been developed to understand trends and patterns of the membrane degradation under AMDTs and AMSTs, estimating membrane lifetime under real-world operating conditions remains a significant challenge. Real-world operating conditions involve a complex interplay of temperature, humidity, and cell voltage that can influence membrane degradation in unique ways. Therefore, predicting fuel cell lifetime under real-world conditions requires accounting for the dynamic and heterogeneous nature of the operating environment.

Furthermore, studying fuel cell degradation by considering individual components separately is a challenging yet crucial task. Each component of a fuel cell, such as the membrane and catalyst layer may exhibit different degradation mechanisms and rates under specific operating conditions. To gain a comprehensive understanding of fuel cell degradation, it is important to investigate the degradation of each component separately. This allows us to identify the primary degradation mechanisms and factors influencing degradation for each component. Comparing the degradation of different components under specific conditions helps identify which component is more susceptible to degradation and may require more attention in terms of design optimization or mitigation strategies. For example, if the membrane is found to degrade more rapidly under certain operating conditions, efforts can be focused on developing more durable and chemically resistant membranes or implementing operating strategies that minimize membrane degradation. Moreover, studying individual component degradation can lead to

insights into the interactions and synergistic effects between components. For example, degradation of the catalyst layer may affect the performance and degradation of the membrane, and vice versa. Understanding these interactions is essential for developing comprehensive degradation models and effective mitigation strategies.

The main objective of this thesis is to establish fundamental modeling frameworks and methodologies for studying the degradation of the cathode catalyst and membrane in fuel cells. The aim is to develop a comprehensive understanding of the degradation mechanisms and processes involved under the use-level conditions. To achieve this, the degradation and lifetime of both the catalyst and membrane will be evaluated under real-world operating conditions, specifically using a transit bus drive cycle that represents a heavy-duty application. Therefore, chapter 2 discusses the modeling frameworks for degradation processes of catalyst and membrane and presents a general FCEV model. The interactions between catalyst and membrane degradation mechanisms, such as voltage degradation and PITM, will be considered. By coupling the performance and degradation aspects, the framework aims to provide a holistic understanding of how the degradation processes influence the overall performance and lifetime of the fuel cell system. The framework includes separate assessments of the catalyst and membrane lifetimes, taking into account the specific operating conditions. By comparing and analyzing the degradation behavior of both components, insights will be gained regarding which component experiences dominant degradation under identical operating conditions, and the overall MEA durability will be assessed under a variety of operating conditions. In chapter 3, the images captured from pristine and degraded catalyst samples are shown and analyzed to gain insights into catalyst degradation mechanisms. Chapters 4 and 5 present the calibration results of the catalyst and membrane degradation models, respectively. Additionally, they showcase and scrutinize the results obtained under use-level conditions. In chapter 6, different mitigation approaches such as lowering the cell temperature and hybridization with a battery will be presented and tested to assess their effectiveness in slowing down the degradation rate and enhancing the durability of the fuel cell system. Finally, the genetic algorithm will be employed to optimize fuel cell overall durability, stack cost and hydrogen consumption during the transit bus drive cycle.

Chapter 2: Modeling framework and methodology

Due to the inherent differences in structure, morphology, and degradation mechanisms between the cathode catalyst and the membrane in fuel cells, separate modeling methodologies are developed to investigate their respective degradation processes. In this chapter, the developed methodologies for studying cathode catalyst degradation and membrane degradation are discussed separately.

2.1. Cathode catalyst degradation model

The following is a formatted version of M. Shojayian and E. Kjeang, **"Simulation of cathode catalyst durability under fuel cell vehicle operation--Effects of stack size and temperature,"** *Journal of Power Sources,* vol. 591, p. 233820, 2024.

The Butler-Volmer kinetic approach is utilized to model platinum dissolution and redeposition, platinum oxide formation, and platinum ion formation during fuel cell operation. While the migration and diffusion of platinum ions can occur in the fuel cell system, their contribution to the overall platinum degradation is considered negligible compared to other degradation mechanisms such as dissolution, redeposition, and oxide formation. Furthermore, although a 1-D model can provide additional insights into Pt degradation, such as the presence of Pt bands in the membrane, it is unnecessary for essential degradation analysis, such as ECSA loss, voltage drop, and lifetime prediction. The developed 0-D model is capable of accurately capturing the degradation behavior, as demonstrated in the calibration results. Moreover, numerous studies in the literature have successfully utilized the 0-D model for Pt degradation analysis and have shown that the platinum degradation and ECSA drop, which are the most crucial indicators of performance drop and catalyst degradation, are not significantly affected by neglecting platinum ion migration [39], [16], [85]. Therefore, a 0-D platinum degradation model that only takes the temporal platinum degradation into account and neglects spatial platinum ion diffusion and migration is developed in this thesis. Also, carbon corrosion is considered to be negligible under the load cycles that involve lower potentials.

The degradation reactions assumed in this model for platinum include:

1. Electrochemical platinum dissolution and redeposition: This process occurs when some platinum is released from the surface and vice versa due to an exchange of

oxygen with platinum, leading to the formation of an oxide layer. The platinum release reaction is

$$Pt \rightleftharpoons Pt^{2+} + 2e^- \qquad E^0 = 1.188 \text{ V vs. SHE} \tag{2.1}$$

2. Platinum Oxide Formation and Growth: The electrochemical reaction for platinum oxide formation and growth is

$$Pt + H_2O \rightleftharpoons Pt\text{-}O + 2H^+ + 2e^- \qquad E^0 = 0.98 \text{ V vs. SHE} \tag{2.2}$$

3. The chemical dissolution and redeposition of platinum oxide are finally as follows.

$$Pt\text{-}O + 2H^+ \rightleftharpoons Pt^{2+} + H_2O \tag{2.3}$$

The chemical dissolution process is dependent on the thickness of the platinum oxide layer and the proton concentration in the electrolyte [16]. To quantitatively describe the processes of platinum dissolution, redeposition, oxide formation, and ion generation, the reaction rate equations based on the Butler-Volmer kinetics approach are employed. These reaction rate equations are outlined by [37]. The rate expression for the electrochemical platinum dissolution and redeposition reactions (Equation 2.1) are given by

$$\begin{aligned} r_{dis} = k_{dis}(T)(1-\theta_{PtO}(r))\left[exp\left(\frac{\alpha_a nF}{RT}(\varphi(t)-\varphi_{dis}(r))\right)\right. \\ \left. - k_r \frac{c_{Pt^{2+}}}{c_{Pt^{2+},ref}} exp\left(\frac{-\alpha_c nF}{RT}(\varphi(t)-\varphi_{dis}(r))\right)\right] \end{aligned} \tag{2.4}$$

where θ_{PtO} is the fraction of oxide coverage on the platinum surface. k_{dis} and k_r are the forward dissolution and reverse rate constants, respectively. After the formation of the oxide coverage, it acts as an insulating layer, inhibiting the platinum dissolution. In this model, the reverse dissolution is considered as the redeposition mechanism. $\varphi(t)$, α_a, α_c, and n are the time-

dependent electrode potential, anodic exchange coefficient, cathodic exchange coefficient, and the number of transferred electrons in Equation 2.1, respectively. F, R, T, $c_{Pt^{2+}}$ are also Faraday's constant, gas constant, cell temperature and platinum ion concentration, respectively. The equilibrium potential φ_{dis} of Equation 2.1 is adjusted from the standard value to incorporate the influence of surface tension of platinum crystallite on the platinum potential according to the following equation [37].

$$\varphi_{dis} = \varphi_{dis}^{\theta} - \frac{\sigma_{Pt} M_{Pt}}{2 r \rho_{Pt} F} \tag{2.5}$$

where σ_{Pt}, M_{Pt}, r, and ρ_{Pt} are platinum surface tension, molar mass, particle radius, and density, respectively. φ_{dis}^{θ} is the standard equilibrium potential of Equation 2.1 which is equal to 1.188 V [86]. Equation 2.5 illustrates the phenomenon of Ostwald ripening, where smaller particles have a lower equilibrium potential compared to larger ones, resulting in a higher rate of dissolution for the smaller particles. The rate equation for the growth of platinum oxide, as expressed in Equation 2.2, can be written as follows.

$$\begin{aligned} r_{ox} = k_{ox}(T) \Bigg[& exp\left(-\frac{\omega \theta_{PtO}(r)}{RT}\right) exp\left(\frac{\alpha_a n F}{RT}(\varphi(t) - \varphi_{ox}(r))\right) \\ & - k_{ox,r} \theta_{PtO}(r) \left(\frac{c_{H^+}}{c_{H^+,ref}}\right)^2 exp\left(\frac{-\alpha_c n F}{RT}(\varphi(t) - \varphi_{ox}(r))\right) \Bigg] \end{aligned} \tag{2.6}$$

where ω is the PtO-PtO interaction energy and k_{ox} and $k_{ox,r}$ are the forward and reverse oxidation rate constants (Equation 2.2), respectively. φ_{ox}, c_{H^+}, and $c_{H^+,ref}$ are the equilibrium potential of the platinum oxide formation reaction (Equation 2.2), the proton concentration in the electrolyte, and a reference proton concentration, respectively. In a similar manner to Equation 2.1, the equilibrium potential of the platinum oxide formation reaction is adjusted from its standard value reported in the literature, as described below.

$$\varphi_{ox} = \varphi_{ox}^{\theta} + \frac{\Delta \mu_{PtO}}{2F} - \frac{\sigma_{Pt} M_{Pt}}{2 r \rho_{Pt} F} \tag{2.7}$$

where

$$\Delta\mu_{PtO} = \Delta\mu^{0}_{PtO} + \frac{\sigma_{PtO} M_{PtO}}{r \rho_{PtO}} \tag{2.8}$$

φ^{θ}_{ox} represents the standard equilibrium potential of Equation 2.2 and is known to be equal to 0.98 V [86] and the parameter $\Delta\mu^{0}_{PtO}$ is a fitted value reported as -42.3 kJ mol^{-1} [37]. The proton concentration in the electrolyte is determined based on the water content in the membrane, which is correlated with the RH. As the RH is assumed to be constant, the proton concentration in the electrolyte is also assumed to remain constant. Eventually, the rate expression for the platinum chemical dissolution reaction (Equation 2.3) is given by [37]

$$r_{cdis} = k_{cdis} \theta_{PtO} \left(\frac{c_{H^+}}{c_{H^+,ref}} \right)^2 \tag{2.9}$$

where k_{cdis} is the rate constant for Equation 2.3.

The rates of change for the platinum particle size, platinum oxide coverage, and platinum ion concentration are determined by using material balance equations. These equations ensure the conservation of platinum, platinum oxide, and platinum ions. The concentration of protons and water is assumed to remain constant. The material balance equations for platinum, platinum oxide, and platinum ions are derived based on the references [37, 16]. The rate of change for the platinum particle radius is determined by considering the material balance equation for platinum which is given by

$$\frac{dr}{dt} = -\frac{M_{Pt}}{\rho_{Pt}} (r_{dis} + r_{cdis}) \tag{2.10}$$

The rate of change for the platinum oxide film coverage is determined by considering the material balance equation for platinum oxide as follows.

$$\frac{d\theta_{PtO}}{dt} = \left(\frac{r_{ox} - r_{cdis}}{\Gamma_{max}} \right) - \left(\frac{2\theta_{PtO}}{r} \right) \frac{dr}{dt} \tag{2.11}$$

where Γ_{max} is the number of moles of active sites per unit of platinum area. Finally, the rate of change for the platinum ion concentration in the electrolyte is calculated by applying the material balance equation for platinum ions as below.

$$\frac{dc_{Pt^{2+}}}{dt} = -\frac{m_v}{M_{Pt}}\left(\frac{dM_{dis}}{dt} - \frac{dM_{cdis}}{dt}\right) \tag{2.12}$$

where m_v is the platinum mass loading per unit of volume. M_{dis} and M_{cdis} are normalized dimensionless platinum mass loss through electrochemical and chemical dissolutions, respectively and their rates of change are given by

$$\frac{dM_{dis}}{dt} = \frac{4\pi\rho_{Pt}\int_0^\infty r^2 f_N(r,t)\frac{dr}{dt}dr}{\frac{4}{3}\pi\rho_{Pt}\int_0^\infty r^3 f_N(r,0)dr} \tag{2.13}$$

$$\frac{dM_{cdis}}{dt} = \frac{4\pi\rho_{Pt}\int_0^\infty r^2 f_N(r,t)\frac{M_{Pt}}{\rho_{Pt}}r_{cdis}dr}{\frac{4}{3}\pi\rho_{Pt}\int_0^\infty r^3 f_N(r,0)dr} \tag{2.14}$$

where $f_N(r,t)$ is the platinum particle radius distribution (PRD) function at time t. In order to consider the variation in particle sizes and account for the phenomenon of Ostwald ripening, the platinum content of the electrode is treated as a collection of spherical platinum particles with different sizes. This allows for a more comprehensive understanding of the evolution of the platinum particles and their impact on the overall electrode performance. After analyzing the TEM images of the pristine catalyst layer samples, it has been determined that the log-normal distribution function provides the most realistic representation of the platinum particle sizes. This statistical distribution is able to accurately capture the variation in particle sizes observed in the images, allowing for a more reliable characterization of the catalyst layer and its performance [16], [87]. The suggested log-normal distribution function for representing the platinum particle sizes in the pristine catalyst layer samples is given by

$$f_N(r,0) = \frac{1}{\sigma\sqrt{2\pi}}exp\left[-\frac{(\ln(r)-\mu)^2}{2\sigma^2}\right] \tag{2.15}$$

Reference [22] reported that the platinum loading and ECSA for the pristine cathode catalyst layer at the BOL were 0.5 mg cm^{-2} and 32 m^2 g^{-1}, respectively. Based on this information, the parameters σ and μ can be determined as 0.549 and 0.538, respectively [16]. These specific values of σ and μ are applicable for the catalyst layer with a platinum loading of 0.5 mg cm^{-2}. However, for different platinum loadings, these parameters can be calculated accordingly to reflect the specific particle size distribution of the catalyst layer.

The change in the PRD with time can be determined by calculating the rate of change of the particle sizes ($\frac{dr}{dt}$) (Equation 2.10) as follows.

$$\frac{\partial f_N(r,t)}{\partial t} = -\frac{\partial}{\partial r}\left[f_N(r,t)\frac{dr}{dt}\right] \tag{2.16}$$

The ratio of the remaining ECSA at a given time t to the initial ECSA can be calculated using the following equation [13], [16], [87].

$$\frac{ECSA(t)}{ECSA(0)} = \frac{\int_0^\infty r^2 f_N(r,t)dr}{\int_0^\infty r^2 f_N(r,0)dr} \tag{2.17}$$

2.1.1. Temperature dependency

Temperature indeed plays a crucial role in the electrochemical reactions of platinum dissolution. There are several ways in which temperature affects these reactions:

1. Tafel Slope: Temperature affects the Tafel slope (RT/F) in the exponent terms of Eqs. 2.4 and 2.6.

2. Equilibrium Potentials: Temperature can influence the equilibrium potentials of the reactions in Eqs. 2.1 to 2.3. However, theoretical studies, such as the one by Kregar et al. [85], [88] have shown that the actual shift from the standard equilibrium potential due to temperature change is insignificant and negligible. Therefore, for the purposes of this study, the equilibrium potential change is neglected.

3. Reaction Rate Constants: The most significant impact of temperature is on the reaction rate constants (k_{dis} and k_{ox}) in Eqs. 2.4 and 2.6.

It is worth noting that the temperature does not directly affect the rate of chemical dissolution of the platinum catalyst. In this thesis, the effect of temperature on the reaction rate constants is

considered using the Arrhenius approach. The Arrhenius equation relates the rate constants to temperature through an exponential term, and it is expressed as follows.

$$k_{dis}(T) = k_{0,dis} T exp(-\frac{\Delta G_{dis}}{k_B T}) \tag{2.18}$$

$$k_{ox}(T) = k_{0,ox} T exp(-\frac{\Delta G_{ox}}{k_B T}) \tag{2.19}$$

where k_B is the Boltzmann constant which has a value of 8.6×10^{-5} eV K^{-1}. The parameters k_0 and ΔG are determined by comparing the model predictions with experimental data through a calibration process. The activation energy barrier (ΔG) represents the energy threshold that must be surpassed for these reactions to occur [85], and it influences the rate at which the reactions proceed. By adjusting the values of k_0 and ΔG, the model can be fine-tuned to match the experimental observations and provide a more accurate representation of the degradation processes taking place at the cathode catalyst.

2.1.2. Methodology of cathode catalyst degradation analysis

The algorithm for the platinum degradation methodology can be summarized as follows:

1. Initialize the variables: $f_N(r, 0) = \text{initial PRD}$, $\theta_{PtO} = 0$, $c_{Pt^{2+}} = 0$
2. Solve Equations 2.10 to 2.12 to calculate the changes in the $f_N(r, t)$, θ_{PtO}, and $c_{Pt^{2+}}$.
3. Calculate the updated ECSA using Equation 2.17, taking into account the changes in the particle size distribution.
4. Repeat steps 2 and 3 until the desired simulation time is reached.

The flowchart for this algorithm, illustrating the sequence of steps, is presented in Figure 2.1.

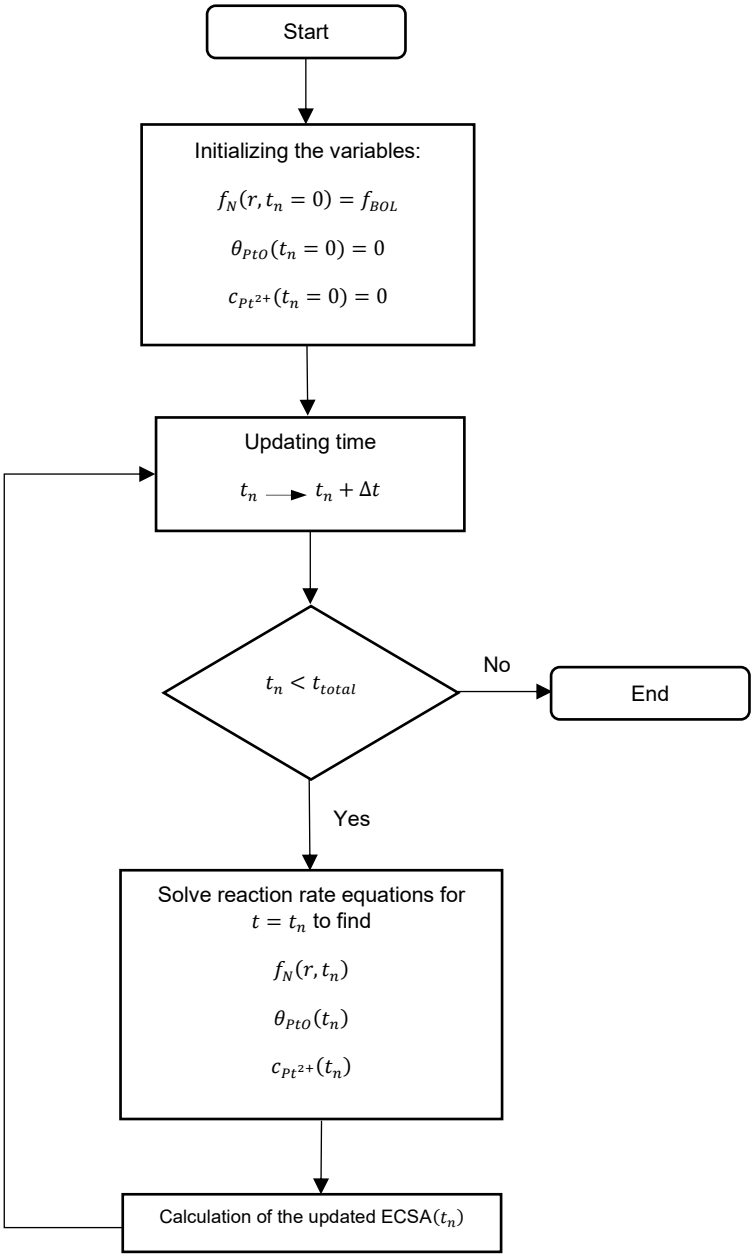

Figure 2.1: Flowchart for the Pt degradation algorithm.

2.2. Membrane degradation model

As mentioned earlier, membrane degradation in fuel cells can be attributed to two main degradation mechanisms: mechanical degradation and chemical degradation. Cyclic stresses arising from the expansion and contraction of the membrane within the fuel cell during dynamic

operating conditions result in mechanical membrane degradation whereas chemical membrane degradation occurs due to the presence of reactive radicals, such as hydroxyl and hydroperoxyl, which can react with the membrane material, leading to chemical reactions and degradation processes. The theory and the reactions leading to the chemical membrane degradation are as follows. The primary factor responsible for attacking the membrane is hydrogen peroxide (H_2O_2). Hydrogen peroxide is generated as a byproduct of the ORR in the catalyst layer. The formation of hydrogen peroxide occurs through the following electrochemical reaction [89].

$$O_2 + 2H^+ + 2e^- \longrightarrow H_2O_2 \qquad E_{2e} = 0.695 \text{ V vs. SHE} \tag{2.20}$$

After its formation in the catalyst layers, hydrogen peroxide can diffuse into the membrane where it can react with a Fenton reagent such as ferrous iron, Fe^{2+}. This reaction is known as the Fenton reaction and can be represented as follows [14].

$$Fe^{2+} + H_2O_2 + H^+ \longrightarrow Fe^{3+} + .OH + H_2O \tag{2.21}$$

The presence of ferrous iron remnants in fuel cell membrane generally arises from contamination during manufacturing process or operation [74]. The produced radicals can cause membrane chemical degradation by reacting with the membrane material which results in main chain scission, side chain unzipping and cleavage. The ultimate consequence is the fluoride release from the membrane and membrane thinning. The degradation of the membrane is aggravated by increasing cell voltage and temperature. Additionally, a decrease in RH has been found to increase the formation of hydrogen peroxide, resulting in greater membrane degradation [71].

Practically, there is an interaction between mechanical and chemical degradation mechanisms in the membrane. To develop a comprehensive model of membrane degradation, it is crucial to consider the chemo-mechanical effects and their combined influence on the degradation process. In this thesis, a Nafion membrane with hydrophobic polytetrafluoroethylene (PTFE) backbone and hydrophilic side chains each terminated with a sulfonic acid group (- SO_3H) is considered. A statistical model of membrane degradation is developed and coupled with the kinetic approach. By coupling the statistical membrane degradation model, the structural effects of the membrane can be captured. This means that not only the chemical and mechanical degradation mechanisms are considered, but also the overall structural integrity of the membrane is taken into account. First, the membrane degradation rate should be fundamentally calculated using the kinetic approach. To this end, the membrane is considered to be composed of a network

of ionomer bundles with a priori random structure, as suggested by [83]. This structural arrangement has been supported by experimental studies [90]. Each bundle consists of an aggregate of cylindrical strands of ionomer, with a uniform surface charge density. To predict the number of ionomer strands within a single bundle (referred to as the aggregate number), the hydrophobic nature of the ionomer and the electrostatic interactions are taken into account. A theoretical modeling, integrating these interactions, is employed to derive the free-energy functional [82]. Next, the aggregate number of ionomer strands within each bundle was determined by minimizing the free energy functional, taking into account the bundle geometry and physical properties such as surface tension. The calculated aggregate number was found to be 6-10 for a typical bundle with a diameter of 2-3 nm in the Nafion membrane [83]. Experimental observations of membrane morphology using techniques such as small-angle X-ray scattering (SAXS) and atomic force microscopy (AFM) have confirmed that the lengths of the bundles fall within the range of 50-100 nm [91]. This range is significant as it is in the order of the persistence length of the ionomer. The persistence length refers to the characteristic length scale over which a polymer chain maintains its overall shape despite thermal fluctuations. The observed bundle lengths provide evidence of the structural properties of the membrane and highlight the organization of the ionomer at the nanoscale level. A schematic of the bundle network and the aggregated ionomer chains in a bundle is shown in Figure 2.2.

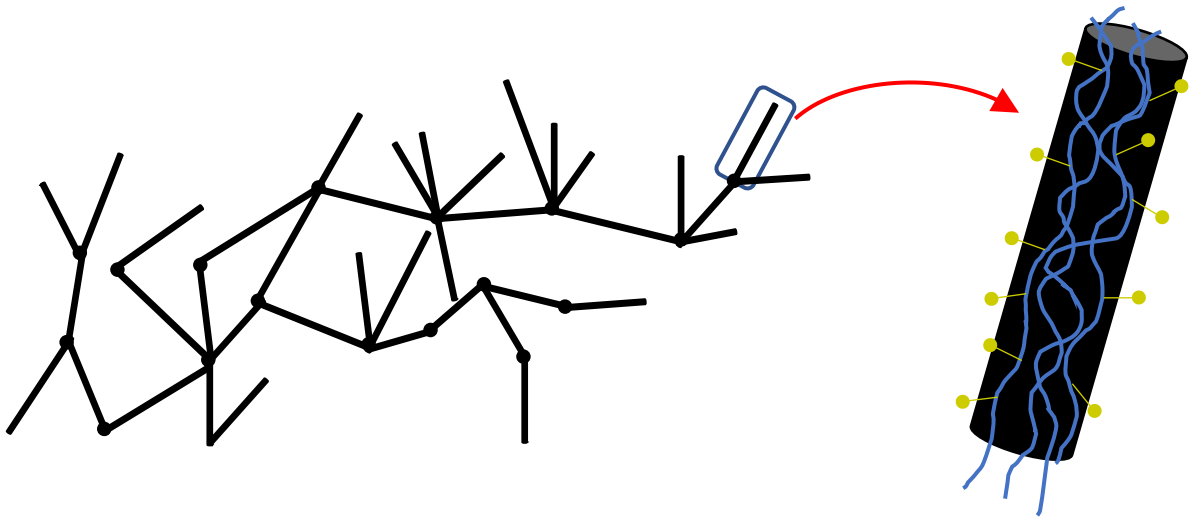

(a) (b)

Figure 2.2: (a) A schematic of the network of the connected bundles; (b) a bundle comprising ionomer chains with sulfonated groups (in yellow) protruding from the chain surface.

In the current modeling framework, the mechanical and chemical degradation mechanisms of the membrane are treated separately. Different degradation rates are applied to each mechanism at every time step during the simulation. The degradation effects are initially applied to individual ionomer chains, which are considered as the smallest computational units in the model. As a result, the affected chains influence the strength and integrity of their respective bundles. Subsequently, broken adjacent bundles form clusters and microcracks. The assumptions of the model can be summarized as follows.

1. The membrane is made up of a random structure composed of interconnected bundles, where each bundle contains a specific number of ionomer chains.

2. All the ionomer chains in the domain have similar mechanical and material properties, including mechanical strength and activation energy.

3. The mechanical failure of the ionomer chains only occurs under tensile load and is not influenced by compressive load.

4. The chemical degradation process is treated independently of the mechanical degradation process. However, the mechanical degradation is affected by chemical degradation through stress enhancement after bundle failure and stress redistribution.

The subsequent section provides a detailed explanation of how the model incorporates the effects of these degradation modes.

2.2.1. Mechanical and chemical degradation rates

The model begins by determining the breaking time of a single ionomer chain, which is assumed to be equivalent to the thermally activated breaking time of a carbon-carbon (C-C) bond in the ionomer backbone under mechanical stress, which is given by [83]

$$\tau = \tau_0 . \exp\left(\frac{E_a - \nu N_a \sigma}{RT}\right) \tag{2.22}$$

where τ_0 represents a constant in the order of the period of atomic bond vibration, E_a denotes the activation energy, ν represents the activation volume of the polymer, σ signifies the applied stress, R represents the gas constant (8.314 J mol^{-1} K^{-1}), N_a stands for Avogadro's number (6.022×10^{23} mol^{-1}), and *T* denotes the temperature. Equation 2.22 was introduced and discussed in the literature [92], [93], [94] and is utilized to determine the breaking time for a polymer fiber, τ. Hence, the breaking rate of each ionomer chain is obtained by taking the inverse of Equation 2.22, which is considered equivalent to the mechanical degradation rate of each ionomer chain in the model.

$$r_m = \tau^{-1} = {\tau_0}^{-1} . \exp\left(-\frac{E_a - \nu N_a \sigma}{RT}\right) \tag{2.23}$$

where r_m is the mechanical degradation rate.

In this model, chemical membrane degradation is addressed separately by considering a degradation rate denoted as r_c [95], [96]. This chemical degradation rate is physically correlated with the fluoride release from the membrane [84], making it dependent on factors such as the membrane material, cell potential, temperature, and humidity.

2.2.2. Computational methodology

The current model employs a statistical approach to simulate the random nature of ionomer/bundle breakage in the membrane. For this purpose, an overall degradation rate is assigned to each ionomer chain, which is defined as the sum of the mechanical and chemical degradation rates ($r_o = r_m + r_c$). This implies that ionomer chains with higher overall degradation rates have a greater probability of breaking. Therefore, the breaking probability of each ionomer chain in the computational domain at a specific time can be determined as follows.

$$p_i(t) = \frac{r_{o,i}}{\sum_{j=1}^{N_i} r_{o,j}} \tag{2.24}$$

where $p_i(t)$ is the breaking probability of the i^{th} ionomer chain, $r_{o,i}$ is the overall degradation rate of the i^{th} ionomer chain and N_i is the number of intact ionomer chains at time t. The breaking probabilities of the ionomers govern their failure at any given time. The breaking time of the i^{th} ionomer chain in the b^{th} bundle, which consists of an aggregate of ionomer chains, is calculated as [83]

$$\Delta t_b = \left(\sum_{j=1}^{k_b} r_{o,j,b} \right)^{-1} \tag{2.25}$$

where Δt_b is the breaking time of the i^{th} ionomer chain in the b^{th} bundle, $r_{o,j,b}$ represents the overall degradation rate of the j^{th} ionomer chain in the b^{th} bundle, and k_b shows the number of intact ionomer chains in the b^{th} bundle. The bundle failure time refers to the time when the last remaining ionomer chain within the bundle fails. The failure time of an ionomer chain within the entire computational domain can then be determined by

$$\Delta t_e = \left(\sum_{b=1}^{N_b} {\Delta t_b}^{-1} \right)^{-1} \tag{2.26}$$

where Δt_e is the failure time of any ionomer chain in the entire domain and N_b is the number of surviving bundles in the computational domain.

The stress distribution among the ionomer chains varies over time with ionomer failure. In this model, upon the failure of an ionomer chain, its mechanical stress is redistributed equally among the remaining intact chains, leading to increased stress levels and subsequently larger degradation rates and breaking probabilities for the surviving chains. However, in the event of bundle failure, the stress redistribution is not equal among adjacent bundles. The bundles in close proximity to the failed bundle experience higher stress levels compared to those located farther away. Therefore, once the j^{th} bundle fails, the new stress carried by the i^{th} surviving bundle is calculated as [84]

$$\sigma_i^{new} = \sigma_i^{old} + \frac{\sigma_j}{d_{ij}^{\gamma}} \left(\sum_{\substack{k=1 \\ k \neq j}}^{N_b} d_{kj}^{-\gamma} \right)^{-1} \tag{2.27}$$

where d_{ij} represents the distance between the i^{th} and j^{th} bundles and γ is the power law exponent, which is assumed to be 5 according to [97].

The broken bundles that are adjacent to each other form clusters, representing microcracks across the membrane. To determine the extent of membrane failure, the length of the longest path along these clusters is calculated. If this length exceeds a critical value, the membrane is considered to have failed. The algorithm described above is applied to randomly generated networks of bundles in order to estimate the membrane lifetime. The mean lifetime value obtained from these networks is considered as the predicted lifetime under specific operating conditions. The discussed algorithm is displayed in Figure 2.3 (t_n denotes the current time of the simulation).

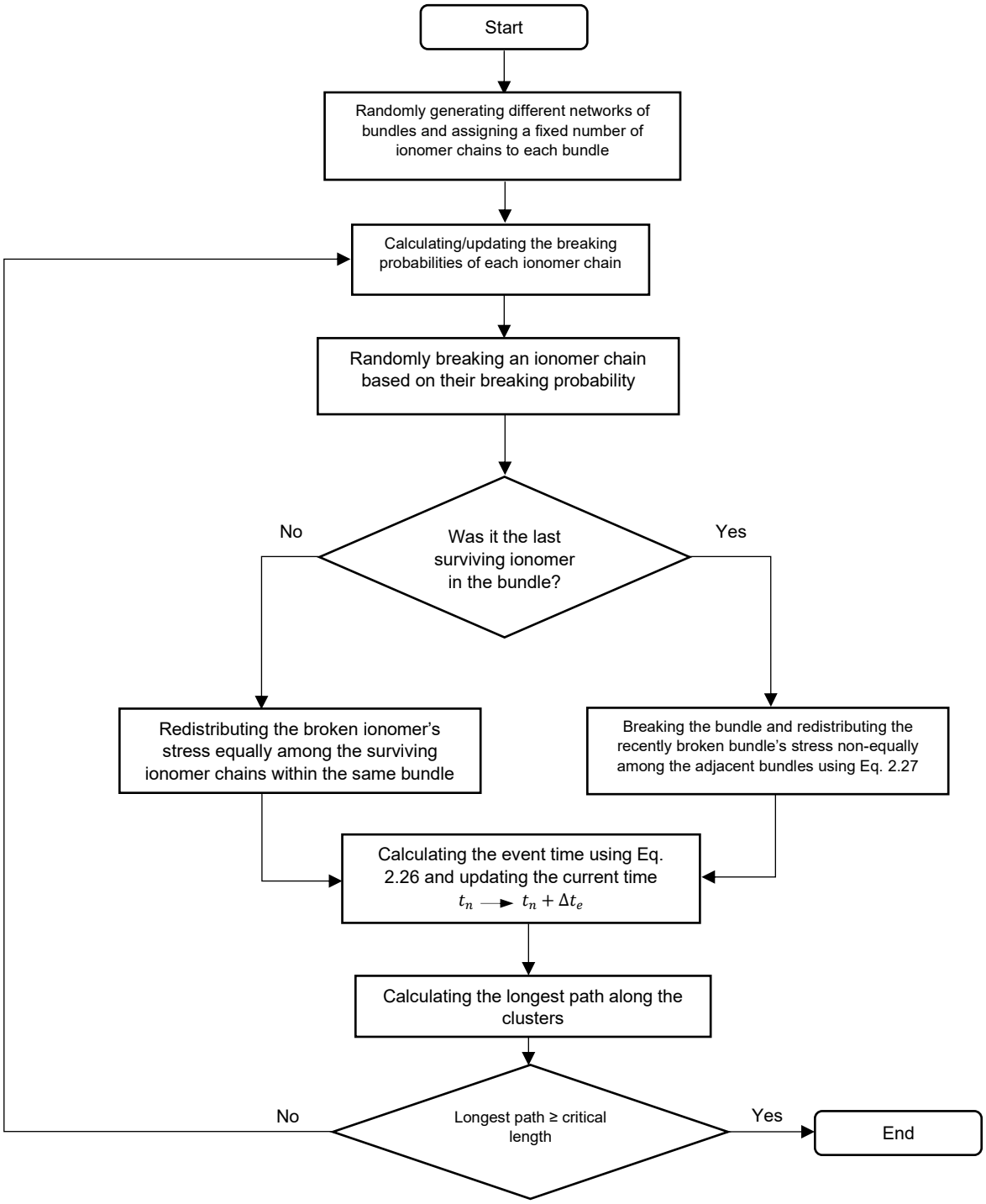

Figure 2.3: Flowchart for the membrane degradation algorithm.

2.3. Drive cycle analysis

The following is a formatted version of M. Shojayian and E. Kjeang, **"Simulation of cathode catalyst durability under fuel cell vehicle operation--Effects of stack size and temperature,"** *Journal of Power Sources,* vol. 591, p. 233820, 2024.

Conducting a vehicle drive cycle analysis is crucial for gaining a comprehensive understanding and addressing fuel cell degradation in real-world operating conditions for FCEVs. To achieve this, it is essential to implement an FCEV performance model, which allows for a targeted analysis under specific vehicle drive cycle conditions. This approach enables the evaluation of fuel cell performance and degradation patterns throughout the entire drive cycle, providing valuable insights into the impact of dynamic operating conditions on the fuel cell system. By considering the unique characteristics of the drive cycle, such as varying loads, speeds, and durations, it becomes possible to assess the fuel cell durability, identify degradation mechanisms, and develop strategies to mitigate degradation and optimize system performance. In order to obtain a cell voltage profile that corresponds to a specific drive cycle, Ahmadi and Kjeang [98] presented a methodology that incorporates various factors such as vehicle aerodynamics, rolling resistance, technical specifications, regenerative braking, and road angle. In this thesis, a similar procedure is adopted which is outlined as follows.

1. First, the vehicle acceleration is calculated using the available drive cycle data.

$$\vec{a} = \frac{d\vec{V}}{dt} \tag{2.28}$$

where a, V, and t are the vehicle acceleration, velocity, and operation time, respectively.

2. The power needed for vehicle acceleration is given by

$$P_{weight} = m_{FCEV}\vec{a}\vec{V} \tag{2.29}$$

where P_{weight} and m_{FCEV} are the required power for vehicle acceleration and the vehicle mass, respectively.

3. The rolling resistance force, which depends on vehicle weight, speed, tire size, and pavement type, is expressed by

$$F_R = C_R m_{FCEV} g cos\beta \tag{2.30}$$

where g is the gravitational acceleration (9.81 m s^{-2}), β is the road angle, and C_R is the rolling resistance coefficient, which is affected by tire material, vehicle speed, and road surface, and is determined by

$$C_R = (0.0041 + 0.000018\,V)C_H \tag{2.31}$$

where C_H is the road surface coefficient, typically assumed to be 1.5 for worn asphalt surfaces [99]. The power required to counteract the rolling resistance force is calculated using the equation

$$P_R = F_R \vec{V} \tag{2.32}$$

Also, the gravity force due to road angle is $F_{mg} = m_{FCEV} g sin\beta$ and the required power to offset that is $P_{mg} = F_{mg}\vec{V}$.

4. The required power to overcome the drag force applied by the air flow is

$$P_{drag} = \frac{1}{2}\rho_{air} A_{front} C_D \vec{V}^3 \tag{2.33}$$

where P_{drag}, ρ_{air}, A_{front}, and C_D are the vehicle drag power, air density, vehicle frontal area, and drag coefficient, respectively.

5. The total power required is obtained by summing the power contributions from vehicle weight, rolling resistance force, drag force, and gravity force. However, it is important to consider the efficiency of the drivetrain, as a portion of the provided power is lost. The adjusted power is calculated by dividing the required power by the drivetrain efficiency as below.

$$P_{total} = \frac{P_{weight} + P_R + P_{drag} + P_{mg}}{\eta_{drivetrain}} \tag{2.34}$$

where $\eta_{drivetrain}$ is the fuel cell drivetrain efficiency.

6. To account for power requirements of vehicle accessories such as air conditioning, lights, and electronics, an auxiliary power component is included. Additionally, the stack efficiency is taken into consideration to reflect power losses within the fuel cell stack.

$$P_{stack,\ demand} = \frac{1}{\eta_{stack}}\left(\frac{P_{weight} + P_R + P_{drag} + P_{mg}}{\eta_{drivetrain}} + P_{aux}\right) \tag{2.35}$$

where $P_{stack,\ demand}$, P_{aux}, and η_{stack} are the total required stack power, auxiliary power, and stack efficiency, respectively.

7. The cell power density is then determined by dividing the required stack power by the cell area and the number of cells.

$$p_{cell,\ demand} = \frac{P_{stack,\ demand}}{N_{cell}A_{cell}} \tag{2.36}$$

where $p_{cell,\ demand}$, N_{cell}, and A_{cell} are the required cell power density, number of cells, and cell area, respectively.

8. To convert cell power density to current density and subsequently to cell voltage, a measured fuel cell polarization curve obtained at the BOL is used.

$$p_{cell,\ demand} = V_{cell} \times i_{cell} \tag{2.37}$$

where V_{cell} and i_{cell} are the cell voltage and current density, respectively. Figure 2.4 depicts a flowchart for the drive cycle analysis.

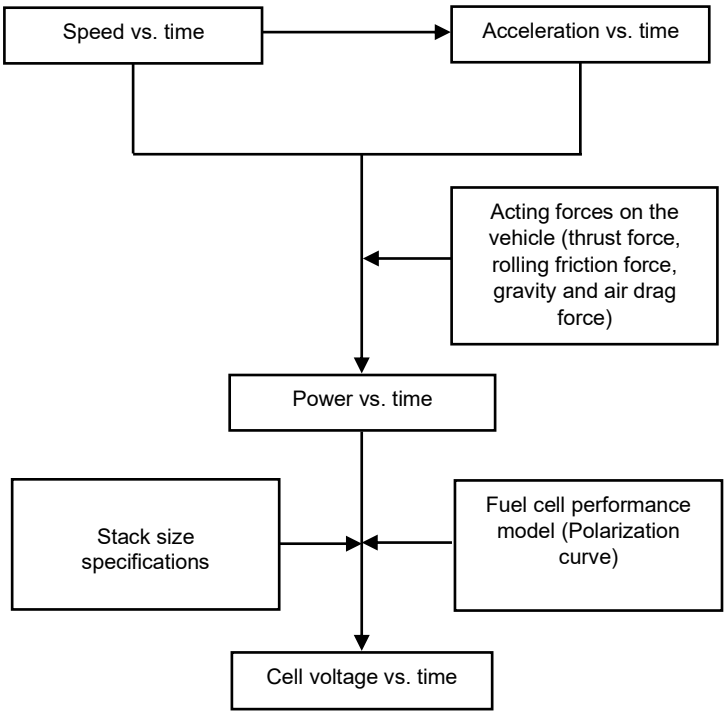

Figure 2.4: The flowchart for the vehicle drive cycle conversion into the fuel cell voltage profile.

During real-world operating conditions, the fuel cell voltage experiences degradation due to the degradation mechanisms occurring in the components such as gradual decrease in ECSA from cathode catalyst degradation over time and the membrane degradation. Therefore, a coupling between fuel cell performance and degradation is inevitable in the model to continuously update the voltage. Zihrul et al. [100] developed a theoretical model to describe the voltage drop caused by ECSA loss in fuel cells. In their model, they assumed that ECSA loss only affects activation losses. The voltage loss was calculated using simple Tafel kinetics considering negligible variation of the exchange current with the ECSA as follows.

$$\Delta\eta_{ORR} = \frac{RT}{\alpha F} ln \frac{ECSA_{BOL}}{ECSA_{EOT}} \tag{2.38}$$

where $\Delta\eta_{ORR}$ represents the cathodic overpotential resulting from ECSA degradation. The parameter α denotes the cathodic transfer coefficient, which is assumed to be equal to 1 in this context. The subscripts "BOL" and "EOT" refer to the beginning-of-life and end-of-test conditions, respectively. While the membrane degradation simultaneously affects the fuel cell performance, its effect is insignificant compared to the ECSA degradation. The impact of membrane degradation on the performance drop is typically intensified abruptly during the last stages of

lifetime and primarily affects the high voltages near OCV [101]. However, the performance drop due to ECSA degradation takes place gradually over time and impacts a broad range of voltages [33]. An analysis has been carried out to compare the performance loss due to ECSA degradation and membrane degradation which is presented in Appendix A. The continuous calculation of voltage drop allows for the updating of the polarization curve over time. Therefore, the developed model for catalyst degradation should include updating the polarization curve at any given time using the ECSA. Figure 2.5 depicts the full methodology used for the analysis of catalyst degradation in a fuel cell vehicle.

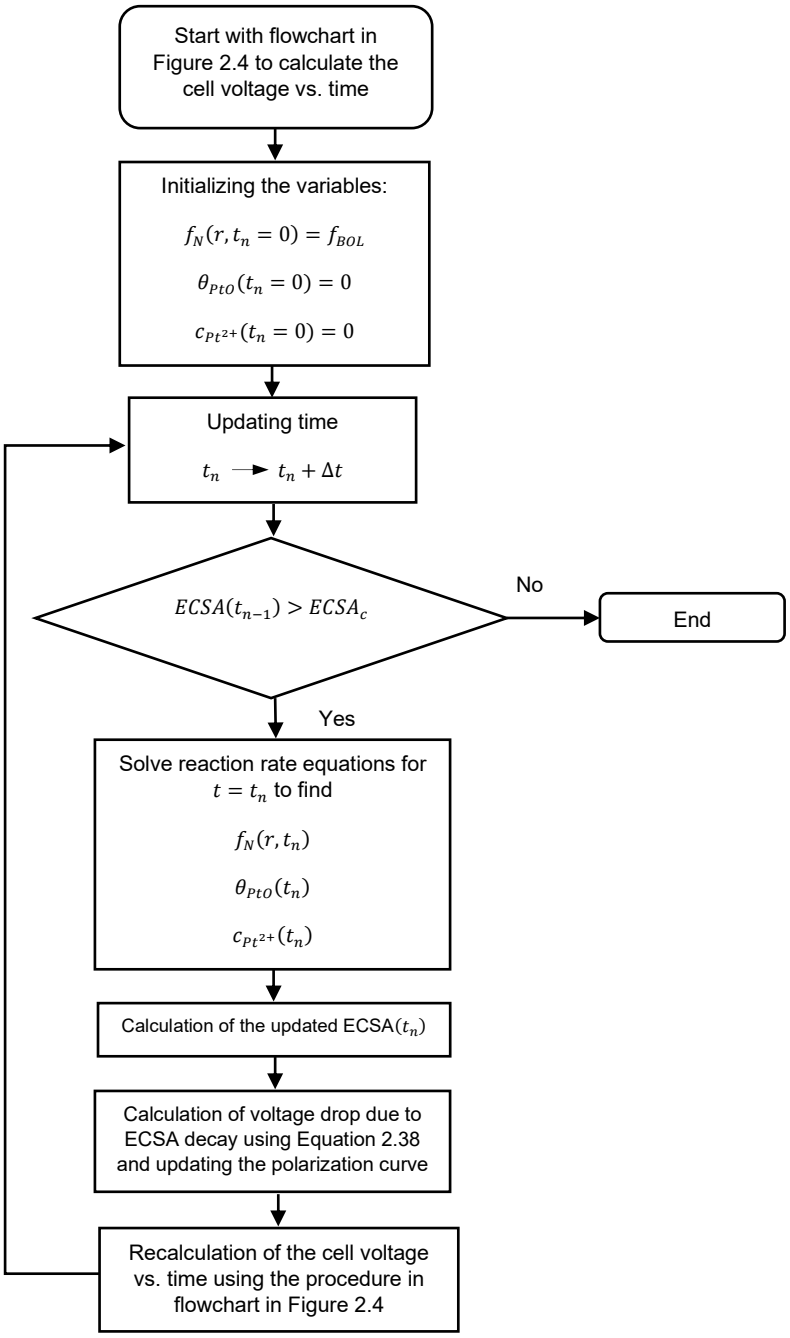

Figure 2.5: Complete flowchart for the catalyst degradation analysis under real-world FCEV operating conditions.

While Figure 2.1 shows the catalyst degradation model alone under AST cycles, Figure 2.5 demonstrates the coupling between FCEV model and the catalyst degradation model, facilitating investigation into real-world operation. Figure 2.5 illustrates that the simulation continues until the ECSA at a specific time reaches the critical ECSA (ECSAc), which serves as the criterion for fuel

cell stack failure due to catalyst degradation. The determination of the critical ECSA will be discussed in the section on lifetime estimation.

This chapter focused on delineating the separate methodologies formulated for investigating cathode catalyst degradation and membrane degradation, given the inherent distinctions in structure, morphology, and degradation mechanisms between the cathode catalyst and the membrane within fuel cells. Furthermore, the FCEV model was integrated and coupled with the durability models to facilitate the prediction of durability at use-level conditions.

Chapter 3: Pristine and degraded catalyst characterization

A comprehensive understanding of catalyst morphology and characterization, including the arrangement and size distribution of platinum particles and their attachment to the carbon support, is essential for building an accurate degradation model for the catalyst layer in a fuel cell. The platinum particle size distribution affects their catalytic activity and performance. The platinum degradation mechanisms impact the platinum size distribution, resulting in a reduction in available catalytic surface area and a decline in catalytic activity and overall performance. To develop a realistic catalyst degradation model that accurately represents platinum degradation, obtaining valuable insights into the platinum particle size distribution at BOL and at the end of the test (EOT) is crucial. To this end, imaging techniques should be performed on the relevant samples to analyze the platinum particles. Scanning electron microscopy (SEM) and TEM are the two widely used techniques in this regard which offer valuable information about the catalyst layer morphology.

SEM is a powerful imaging technique used to study the surface morphology and microstructure of materials at high resolution. SEM involves generating a focused electron beam that scans the sample's surface, and the interaction between the electrons and the sample leads to the emission of various signals. These signals are detected and processed to form images that reveal the sample's surface features and composition. SEM typically provides lower resolution than TEM, usually in the range of a few nanometers to tens of nanometers [102]. In this thesis, the Nova NanoSEM located at 4D labs in SFU was employed to capture the SEM images.

TEM is an advanced microscopy technique utilized to examine the internal structure and composition of materials at the nanoscale. As opposed to SEM, which images the surface of samples, TEM is operated by passing an electron beam through an ultra-thin specimen. The focused electron beam interacts with the sample, leading to the formation of various signals that are recorded to create detailed internal images. TEM offers much higher resolution, capable of resolving features at the atomic scale, typically down to 0.1 nm; therefore, TEM is employed to generate valuable data about the microstructure, including crystal lattice arrangement, defects, and nanoparticles [103]. In this study, a Tecnai Osiris S/TEM was utilized for obtaining the TEM images. Thin samples suitable for TEM were prepared using an EM FC7 ultramicrotome manufactured by Leica, located at 4D labs. Subsequently, energy-dispersive X-ray spectroscopy

(EDX) was conducted using the EDX detector in the TEM system after capturing TEM images to gain insights into the composition and elemental structure of the samples. A detailed discussion of these procedures will follow in the next section.

In this thesis, two samples are considered for this purpose: one sample at BOL and one at EOT where the sample had been subjected to fuel cell cathode catalyst AST based on cell potential cycling between 0.7 and 0.98 V on a square wave with a 3 second-hold time at each LPL and UPL. The cell temperature was 80 ℃ with an RH of 90%. Hydrogen/air were utilized for anode and cathode, respectively [15]. In the following sections the details of the sample preparation and characterization are discussed.

3.1. Pristine sample preparation for imaging

During the catalyst layer fabrication process, a catalyst ink, which is a liquid solution containing the catalyst material, is sprayed onto the membrane to create the catalyst layer. The catalyst ink can be independently applied for obtaining TEM images using TEM grids. A TEM grid is a thin, flat, and perforated copper sheet that serves as a support for the sample during the TEM analysis. Therefore, the catalyst ink is utilized as the sample at BOL for TEM images. The catalyst ink is composed of suspended Pt/C nanoparticles, a solution of ionomer that facilitates proton conductivity, and a solvent such as methanol. A platinum/high-surface-area carbon powder with a 50% platinum weight fraction is added to the ionomer solution and methanol. The ionomer solution comprises a 20% weight fraction of Nafion PFSA dispersion. Then, the resulting solution will be subjected to the sonication process to obtain a homogeneous mixture. After the catalyst ink is prepared, a small drop of the ink is carefully placed onto a copper TEM grid. The solvent evaporates after depositing on the grid. Therefore, the TEM grid, containing only porous catalyst layer material, is inserted under the transmission electron microscope. Figure 3.1 shows two TEM images of the pristine sample. These two images, that were taken from two different locations of the sample, clearly show the platinum particle distribution within the carbon support. These specific spots were meticulously selected within the sample due to their clear display of platinum particles, making it easier to visualize and analyze the particles effectively. The darker dots indicate the platinum particles whereas the lighter clusters signify the carbon support. The darkest areas in the images are the results of the accumulation of platinum particles in the image depth. The catalyst layer prepared from the same ink is expected to exhibit an identical catalyst structure.

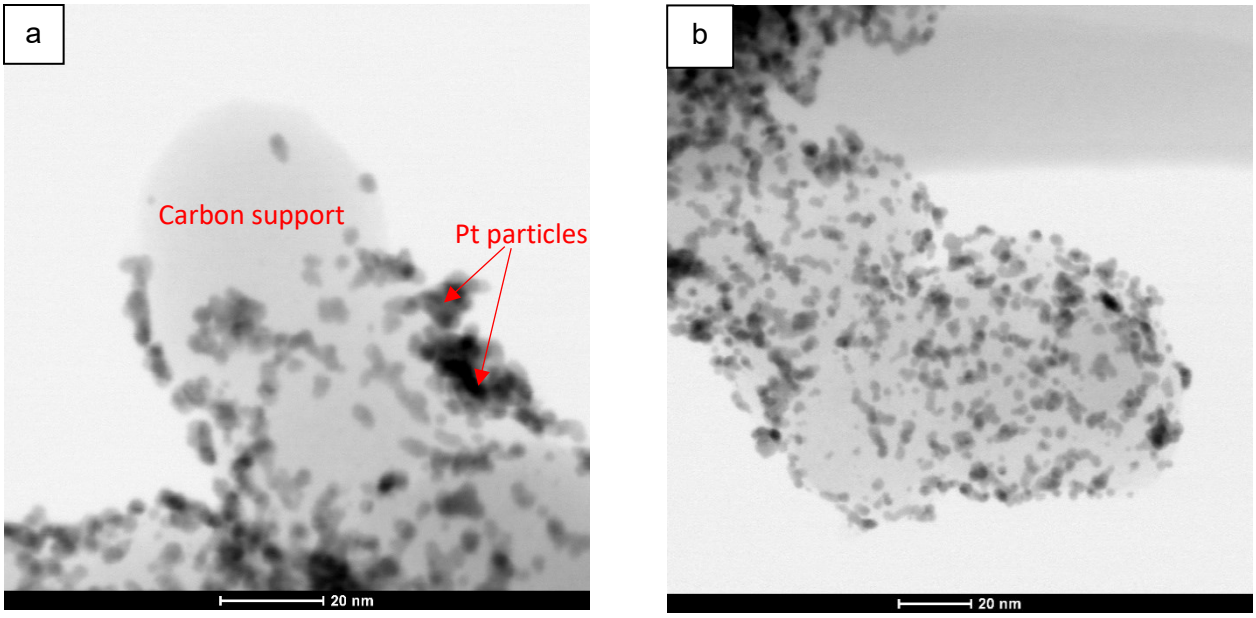

Figure 3.1: TEM images of the catalyst ink at (a) 900kx and (b) 630kx magnification.

To ensure accurate composition analysis of the catalyst, an elemental analysis should be performed. EDX is commonly utilized for this purpose. EDX is an analytical technique used in conjunction with electron microscopes, such as SEM and TEM, to determine the elemental composition of a sample. During EDX analysis, the sample is bombarded with an electron beam, causing the atoms to emit characteristic X-rays. Each element emits X-rays at specific energy levels, which are unique to that element. The X-rays emitted by the sample are collected by a detector, and the energies of the X-rays are measured. From these energy measurements, the elemental composition of the sample can be determined. EDX can detect a wide range of elements, from light elements like carbon and oxygen to heavy elements like gold and uranium. Figure 3.2 displays the result of an EDX analysis conducted on the TEM image of Figure 3.1a.

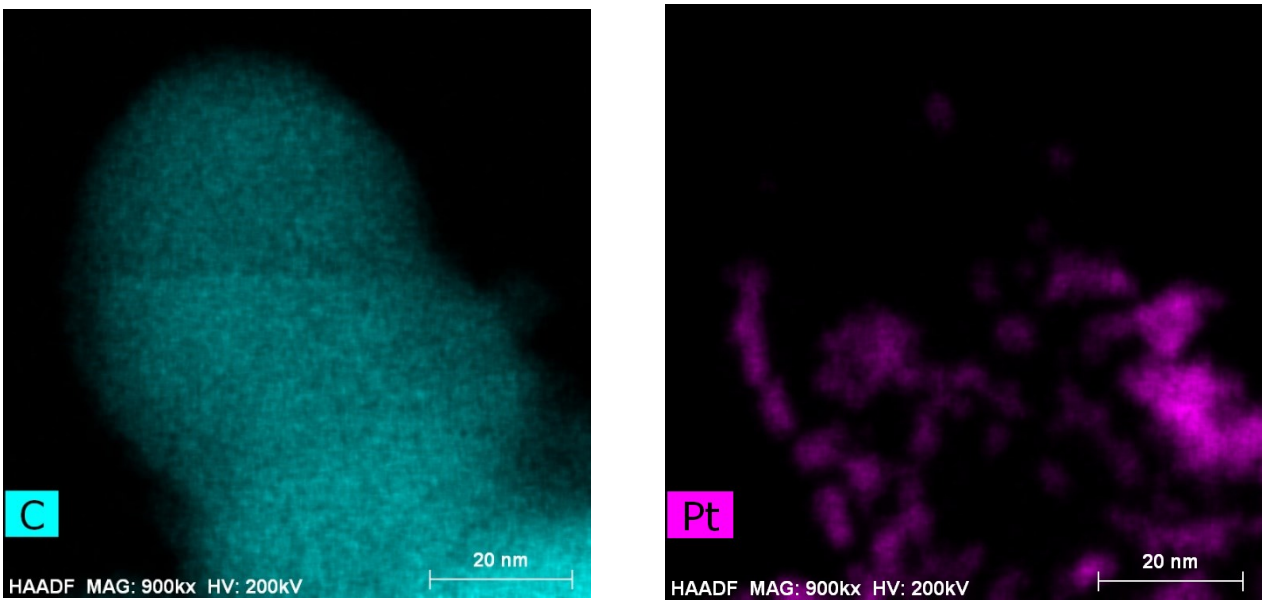

Figure 3.2: The EDX analysis on the TEM image of Figure 3.1a.

In Figure 3.2, the results of the EDX analysis clearly show separate indications of carbon and platinum. It is concluded that the dark areas in Figure 3.1 correspond to regions where platinum is present, while the bright areas represent the carbon support. This distinction allows for identifying and visualizing the distribution of platinum particles within the catalyst layer and their attachment to the carbon support. Therefore, a particle size distribution (PSD) is obtained using the TEM images in Figure 3.1 by employing the ImageJ software which is an open-source image analysis software. Figure 3.3 depicts the measured PSD.

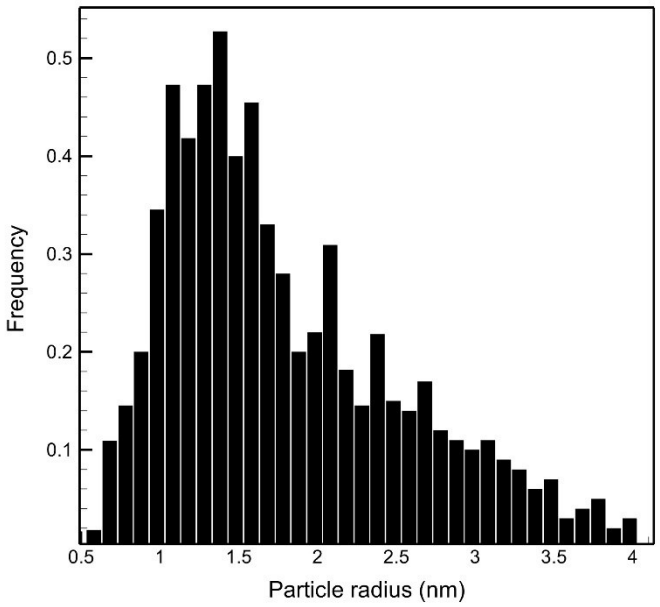

Figure 3.3: PSD obtained from the TEM images at BOL.

Figure 3.3 indicates that the sizes of platinum particles within the catalyst layer are not evenly distributed but rather exhibit a characteristic pattern commonly observed in various particle systems. This Figure illustrates that the platinum PSD follows a log-normal trend. The calculated average particle radius is 1.79 nm which falls within the reported range in the literature (1.25-2.6 nm) [30], [104].

3.2. Degraded sample preparation for imaging

For the degraded sample, an MEA that was subjected to an AST cycle is chosen. The AST was performed by Messing [15], a former M.A.Sc. student at the SFU Fuel cell research laboratory (FCReL). Figure 3.4 shows the AST cycle and the resulting ECSA loss over time reported by [15].

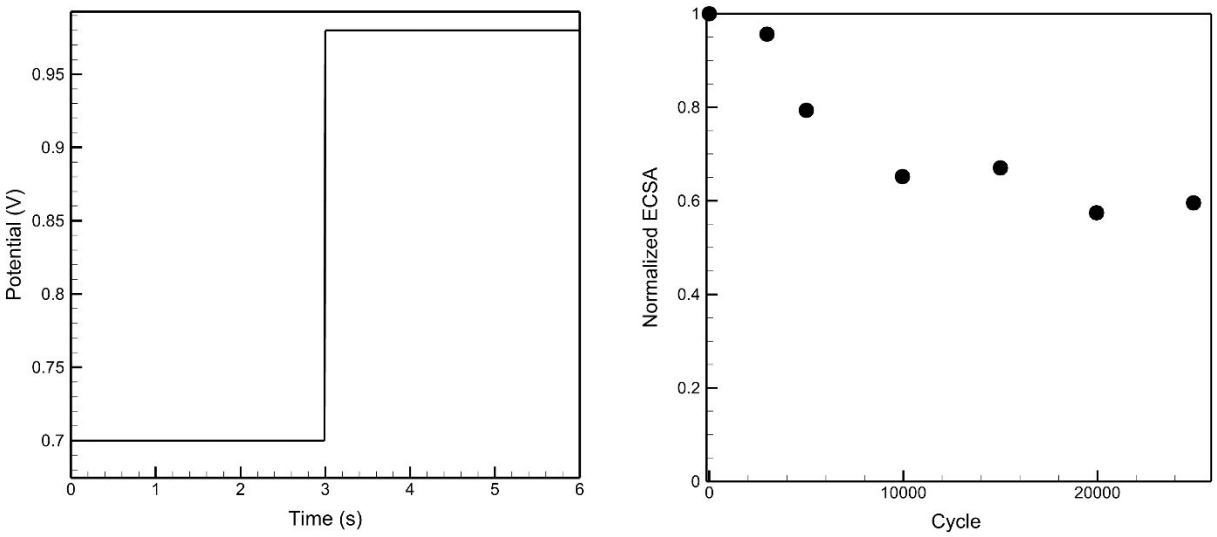

(a) (b)

Figure 3.4: (a) The AST cycle and (b) the ECSA loss with the number of the AST cycles reported by [15].

Preparing the degraded sample for imaging is more complex compared to the pristine sample. The degraded cathode catalyst layer is situated within the MEA, positioned between the membrane and cathode GDL. To prepare a degraded sample for imaging, the GDLs should be carefully detached and discarded from the MEA. Once the GDLs are removed, a small part of the catalyst coated membrane (CCM) is cut in the middle. The section is chosen in the middle of CCM to avoid any edge effects. The resulting part of the CCM should be taken for cross-sectioning. For obtaining high-quality TEM images, the sample thickness is a critical factor. It is recommended that the sample be thin enough, typically less than 100 nm thick, to ensure optimal imaging resolution and clarity. The electron beam interacts with the sample as it passes through, and if the sample is too thick, the electrons will scatter and attenuate, leading to a loss of image detail and contrast. Therefore, it is essential to perform sample cross-section cutting before TEM imaging. This process involves carefully preparing a thin slice of the sample, typically using specialized techniques such as ultramicrotomy. The process involves cutting samples into ultra-thin sections, typically on the order of 50-100 nm in thickness, allowing for high-resolution imaging and detailed analysis of the sample structures.

Prior to ultramicrotomy, it is essential to embed the sample in an appropriate resin to provide the necessary support and stability during the sectioning process. Various epoxy resins are utilized for microtomy, and in this thesis, one of the commonly used epoxy resins is employed, following the published recipe. The details of the resin preparation recipe are provided in the appendix B. Once the epoxy resin is prepared, the sample of the CCM is embedded in the resin, ensuring that it is securely held in place for sectioning. Subsequently, the embedded sample and the epoxy resin are placed in an oven set at 60℃ and kept there to dry out for 12 hours. This drying process allows the resin to solidify, providing the necessary support and stability for the subsequent ultramicrotomy process.

After the resin-embedded sample is prepared, it is positioned on the ultramicrotome for sectioning. Before starting the sectioning process, the mounted sample is carefully trimmed using a razor blade. Trimming serves to expose the specific region of interest and eliminate any excess resin, creating a smooth surface for sectioning. Next, ultra-thin sections are cut from the trimmed sample using a previously prepared ultra-sharp diamond or glass knife. The ultramicrotome enables precise control over the thickness of the sections, ensuring uniformity in the section thickness throughout the sample. This precision is essential for obtaining high-quality and consistent sections suitable for subsequent analysis. As the sections are cut, they are carefully collected on a water surface and then transferred onto a TEM grid. The sections are now ready for the TEM imaging. Figure 3.5 illustrates the dried resin-embedded sample and the TEM image of the AST degraded cathode catalyst layer, subjected to the AST shown in Figure 3.4a for 25,000 cycles. The section shown in Figure 3.5 is 70 nm thick which is suitable for transmission microscopy and depicts the cathode catalyst layer next to a thin cross-sectional slice of the membrane.

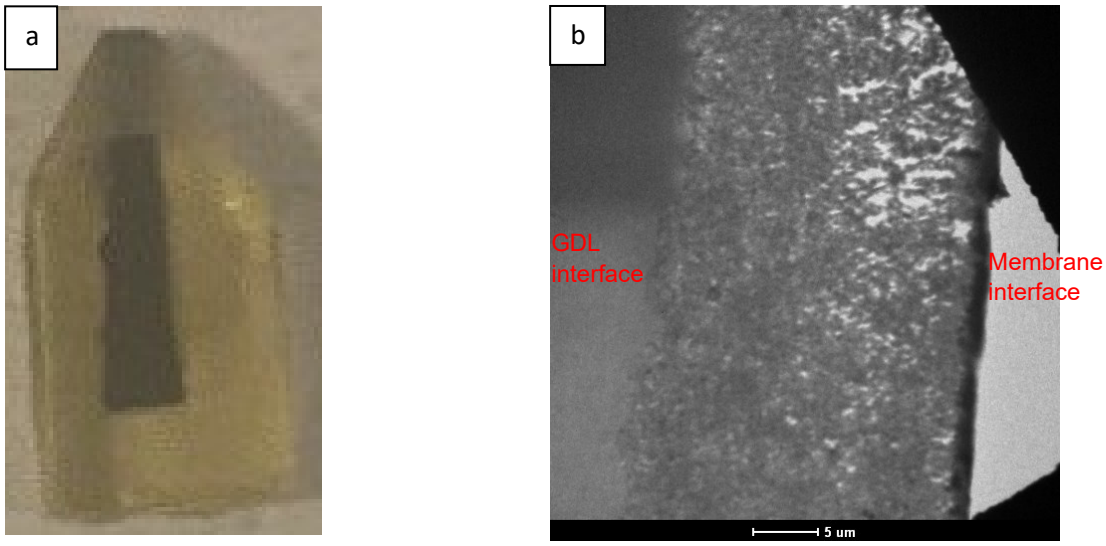

Figure 3.5: (a) the dried resin-embedded sample; (b) The TEM image of the degraded cathode catalyst layer at 2.5kx magnification.

The degraded samples might have non-uniform platinum PSD within the catalyst layer. This non-uniformity can be attributed to the diffusion and migration of the generated platinum ions across the catalyst layer during the degradation process. Migration of ions refers to the movement of ions under an electric field through an electrolyte toward the electrode of the opposite charge while diffusion means the movement of matter driven by concentration gradient across a medium. To observe the non-uniform platinum PSD, three locations are chosen across the cathode catalyst layer. The first location is selected close to the membrane, representing the region near the interface between the membrane and the catalyst layer. The second location is chosen in the middle of the catalyst layer, capturing the central region of the layer. Lastly, the third location is selected close to the GDL, representing the region near the interface between the catalyst layer and the GDL. At each location, three TEM images showing the platinum distribution are taken parallel to the catalyst-membrane interface to capture the spatial effect in this direction on the platinum PSD. Then, the average of the platinum PSD is calculated. The obtained images and the discussion will be presented as follows.

Region close to the catalyst-membrane interface

The images taken from the catalyst in the region close to the membrane are shown in Figure 3.6.

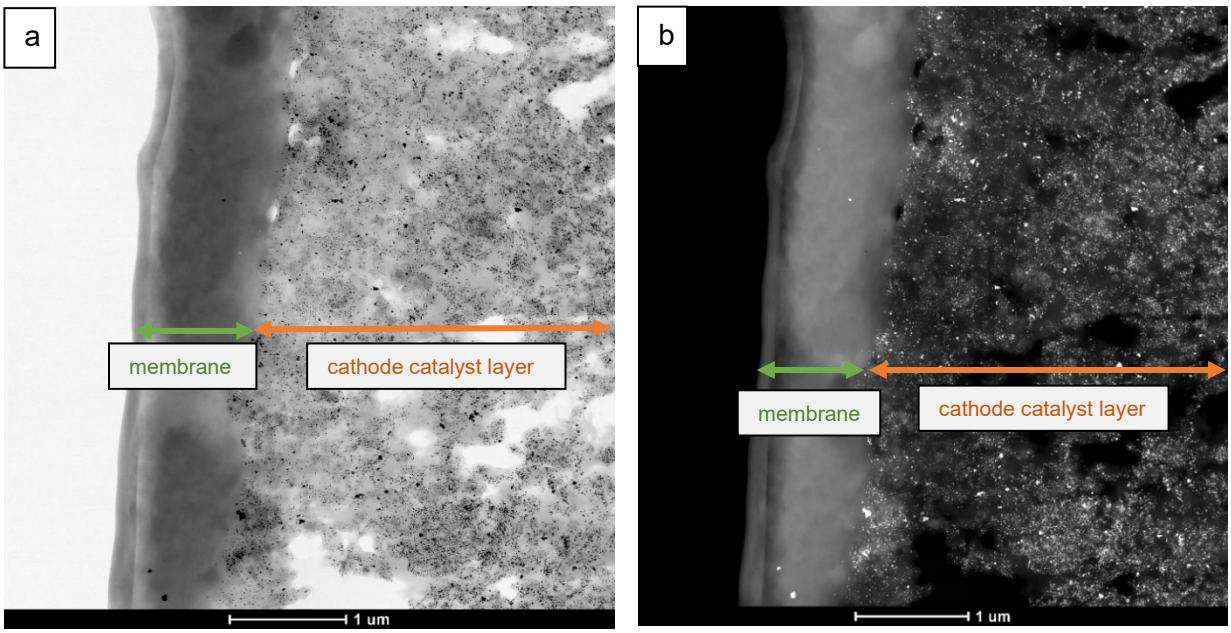

Figure 3.6: TEM images of the degraded cathode catalyst layer in the region close to the catalyst-membrane interface at 20kx magnification; (a) Bright-field (BF) image, (b) High-angle-annular dark-field (HAADF) image.

An EDX analysis is conducted to ensure that the captured region is in fact close to the membrane. Figure 3.7 illustrates the EDX analysis result.

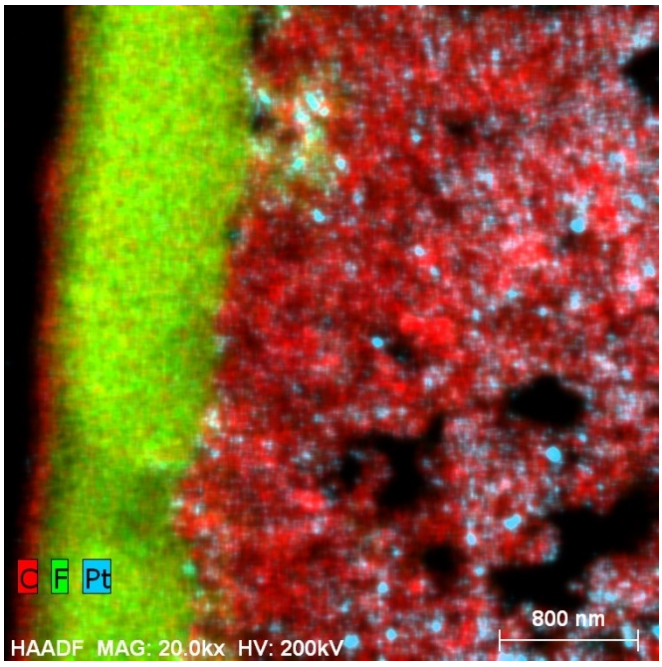

Figure 3.7: EDX analysis performed on the TEM image from the region close to the catalyst-membrane interface.

Figure 3.7 reveals elemental distribution within the TEM images in Figure 3.6. The left side of the image predominantly shows the presence of fluorine, indicating that this region corresponds to the membrane. As fluorine is unique to the membrane and the ionomer dispersed within the catalyst layers, its dominance on the left side confirms the identification of the membrane in the TEM images. On the other hand, the right side of the image displays the distribution of platinum supported on carbon. This confirms the presence and arrangement of platinum particles attached to the carbon support material within the catalyst layer. Figure 3.8 shows the TEM images of the platinum particle distribution within the region close to the membrane.

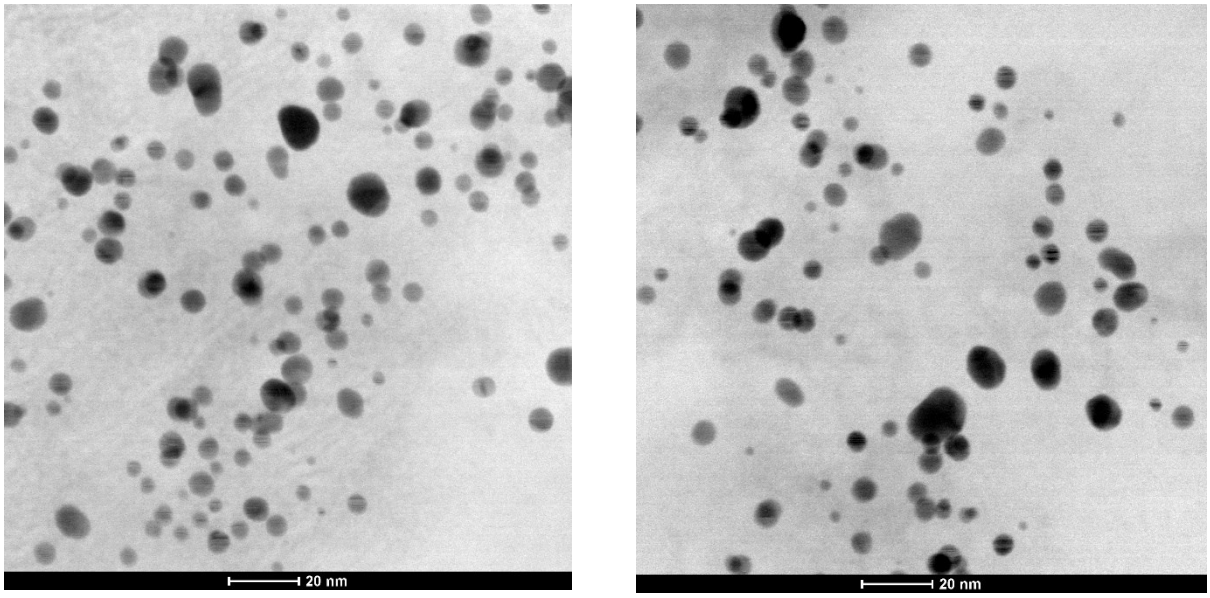

Figure 3.8: Representative sample images showing the platinum particle distribution in the region close to the catalyst-membrane interface at 630kx magnification.

Region in the middle of catalyst layer

The TEM images and the platinum particle distribution in the middle of the degraded catalyst layer are shown in Figure 3.9 and Figure 3.10, respectively.

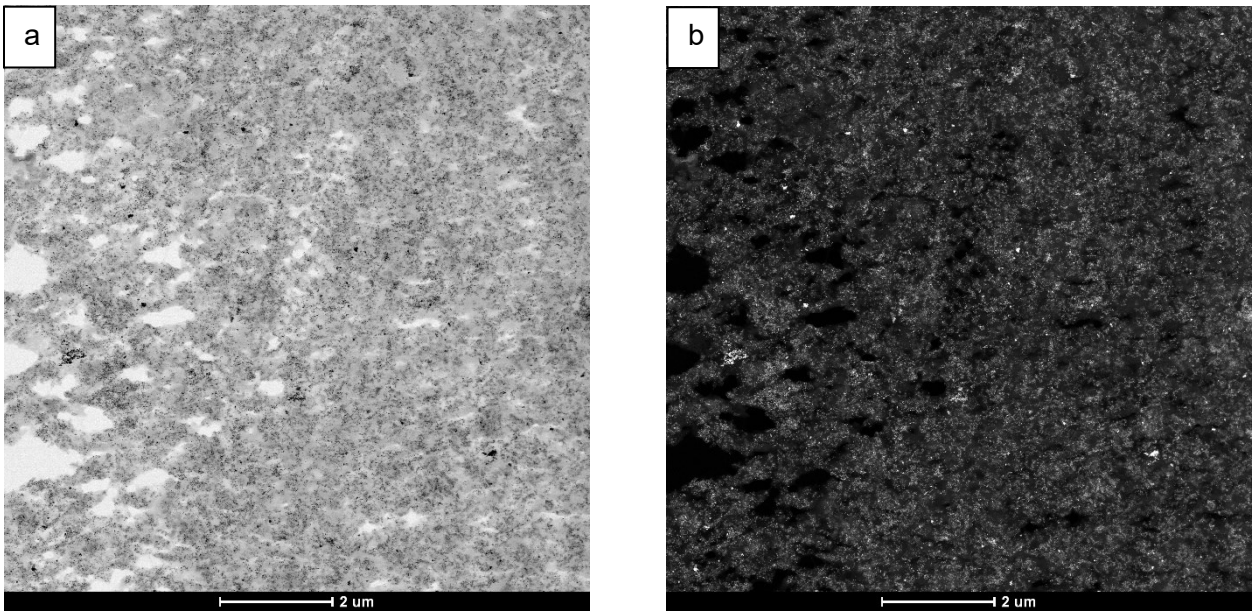

Figure 3.9: The TEM images of the middle of the catalyst layer at 9kx magnification; (a) BF image, (b) HAADF image.

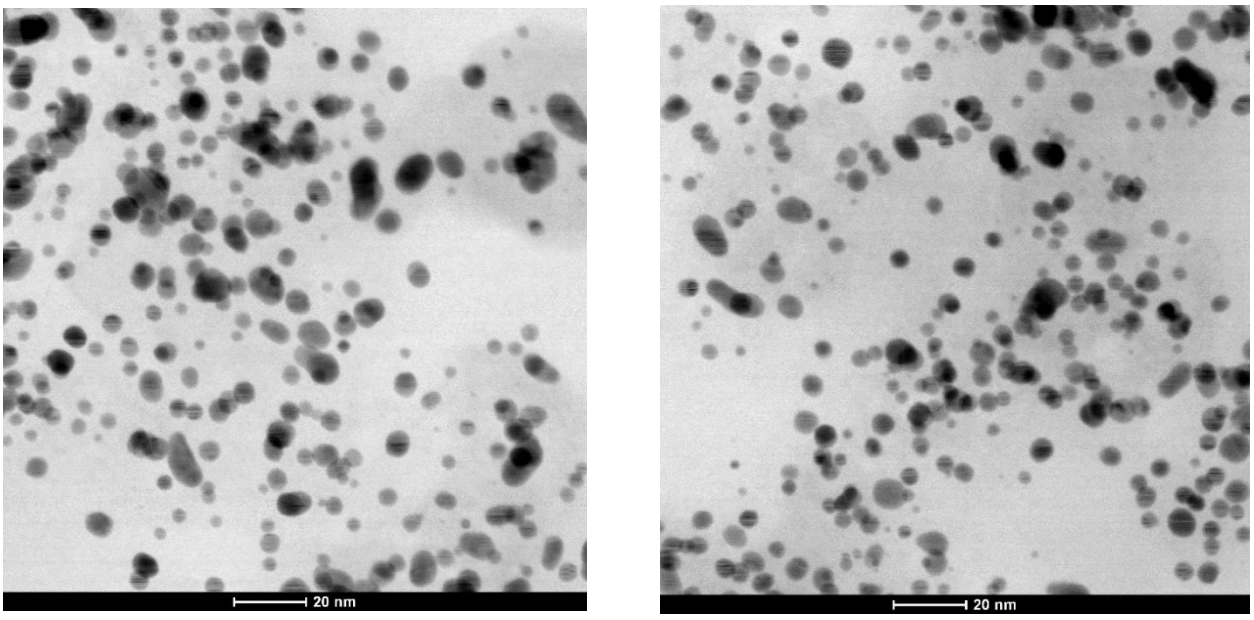

Figure 3.10: Representative sample images showing the platinum particle distribution in the middle of the catalyst layer at 630kx magnification.

Region close to the catalyst-GDL interface

The TEM images and the platinum particle distribution in the region close to GDL are shown in Figure 3.11 and Figure 3.12, respectively.

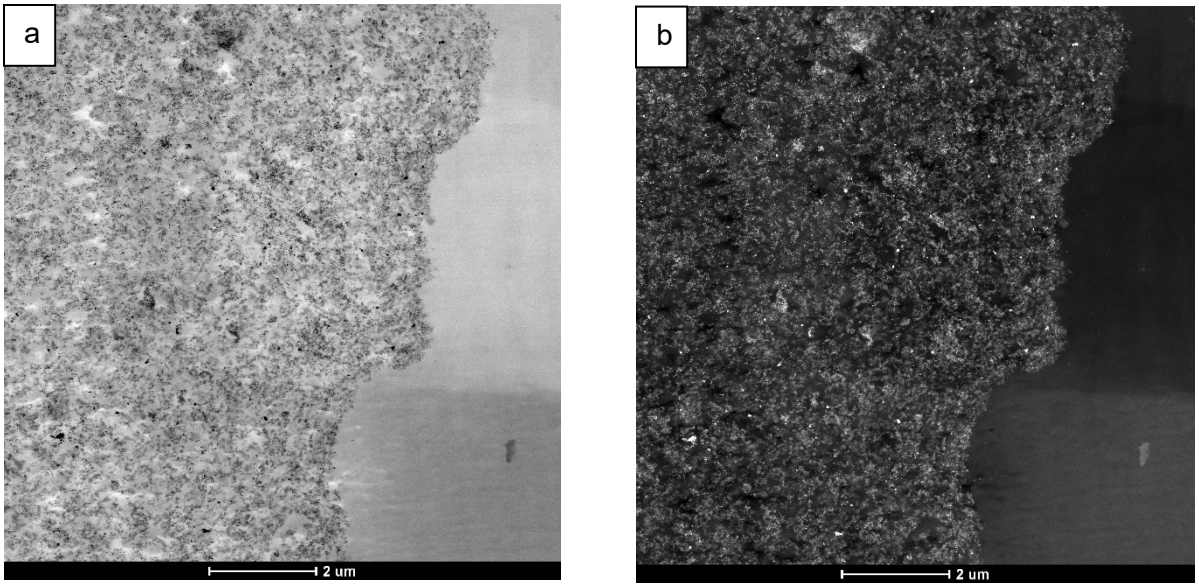

Figure 3.11: The TEM images of the catalyst in the region close to the catalyst-GDL interface at 9kx magnification; (a) BF image, (b) HAADF image.

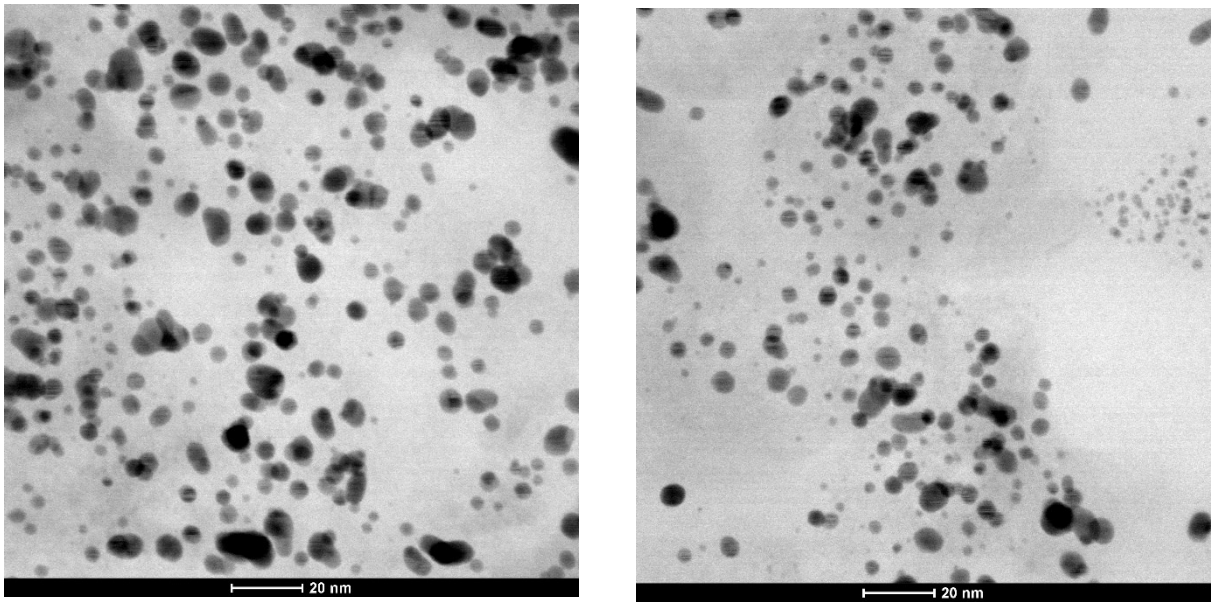

Figure 3.12: Representative sample images showing the platinum particle distribution in the region close to the catalyst-GDL interface at 630kx magnification.

After taking the TEM images of the catalyst at different regions, the platinum PSDs are calculated and depicted in Figure 3.13, and the average particle radii are displayed in Figure 3.14.

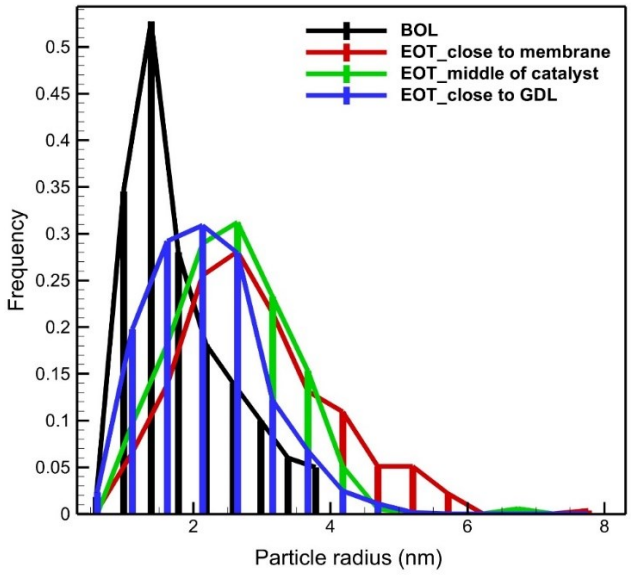

Figure 3.13: The platinum PSD at BOL and EOT at different regions across the catalyst.

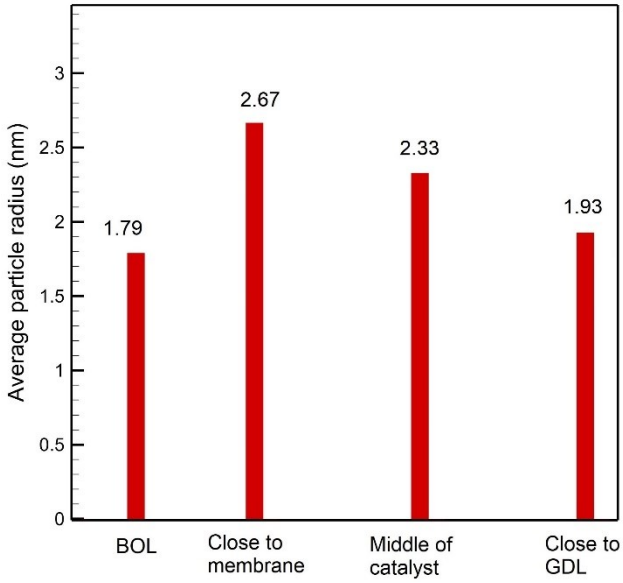

Figure 3.14: The average platinum particle size at BOL and EOT at different locations.

The fresh samples at BOL are expected to have uniform platinum concentration and identical platinum PSD across the catalyst layers when using ultrasonic spray coating for sample

preparation [15]. Figures 3.13 and 3.14 demonstrate the platinum particle growth over time due to degradation which is the direct result of the Ostwald ripening. However, the average particle growth during the degradation is not even across the entire catalyst layer. The platinum particles in the region close to the membrane experience a more significant growth compared to the other regions within the catalyst. Furthermore, the platinum concentration can be calculated at each location given that the sample thickness was equal in each case (70 nm). The TEM images presented in Figures 3.8, 3.10 and 3.12 are used for calculation of the platinum concentration. These images share an identical catalyst region area, allowing for a direct comparison of the concentrations in all three cases. The platinum concentration is normalized with the platinum concentration in the region close to the membrane. Figure 3.15 depicts the measured platinum concentration at EOT and at each catalyst location.

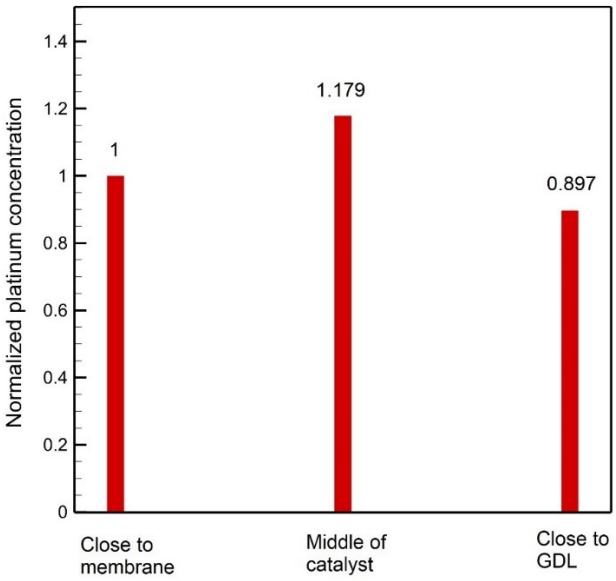

Figure 3.15: The platinum concentration at EOT and at each catalyst region (normalized with the platinum concentration in the region close to the membrane).

According to Figure 3.15, the platinum concentration in the region close to the membrane is lower than that in the middle of the catalyst. This finding is consistent with the published results [26]. This observation is attributed to the movement of the generated platinum ions toward the membrane. A number of platinum ions may move toward the membrane under diffusion and migration, leading to a reduction in the platinum concentration within the region close to the membrane. By taking a cross-sectional SEM image of the degraded sample, the movement of platinum ions toward the membrane and their subsequent deposition in that region can be

confirmed. As depicted in Figure 3.16, the SEM image of the degraded sample clearly illustrates the formation of a platinum band inside the membrane, specifically near the cathode interface. This observation validates the anticipated higher degradation levels at the cathode compared with the anode. The penetrated platinum ions in the membrane can be reduced to the metallic platinum upon contact with the hydrogen crossover from the anode. The resulting platinum particles deposited in the membrane are considered inactive as they do not contribute to the ORR in the catalyst. The partial pressures of hydrogen and oxygen control the location of the platinum band. The movement of platinum ions toward the membrane occurs under identical driving forces such as diffusion, migration, and gas pressure; therefore, they eventually deposit within the membrane in a linear arrangement parallel to the catalyst-membrane interface.

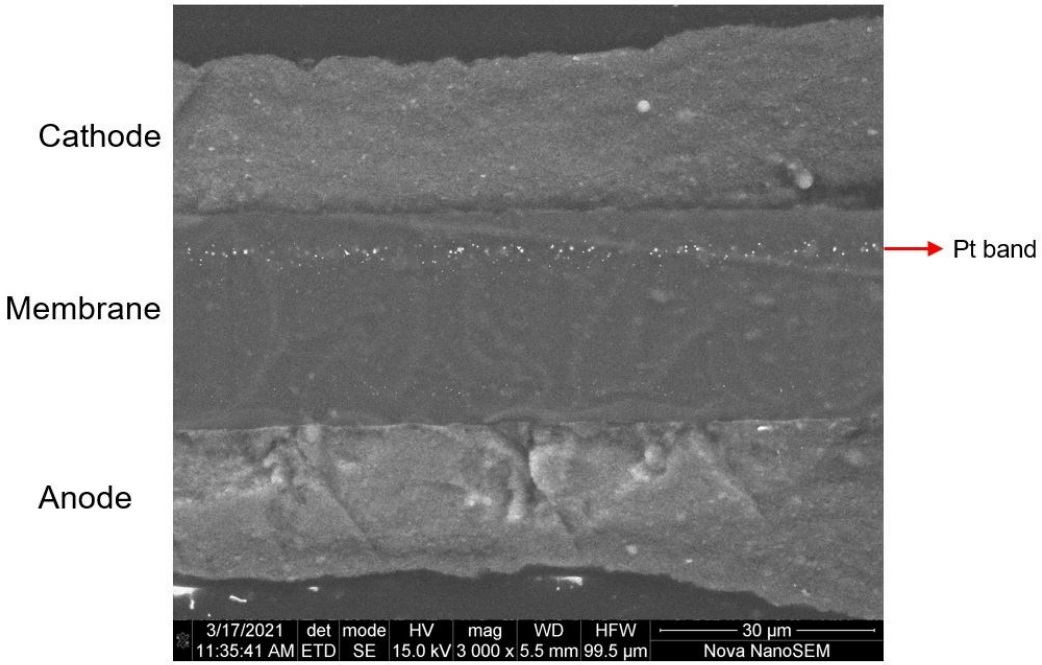

Figure 3.16: Cross-sectional SEM image of the degraded CCM sample showing the platinum band inside the membrane.

In this chapter, the captured images from pristine and degraded catalyst samples were presented and analyzed, and insights into platinum degradation mechanisms were obtained. Platinum PSDs were measured at BOL and EOT in different regions. Platinum particle growth was observed in the degraded sample, confirming the Ostwald ripening.

Chapter 4: Cathode catalyst degradation and lifetime

This chapter is a formatted version of M. Shojayian and E. Kjeang, **"Simulation of cathode catalyst durability under fuel cell vehicle operation--Effects of stack size and temperature,"** *Journal of Power Sources,* vol. 591, p. 233820, 2024.

The catalyst and membrane degradation models are implemented separately to evaluate their respective degradation. However, it is crucial to maintain the coupling between these models as the cell voltage degradation is impacted by the catalyst degradation. In particular, the catalyst degradation model estimates the voltage degradation over time, taking into account the ECSA loss. This voltage degradation is then integrated into the membrane degradation model, ensuring a comprehensive understanding of the overall degradation process. In this chapter, the catalyst degradation model is calibrated using a variety of empirical results from the literature, considering different potential cycles, UPLs, LPLs, and temperatures. Subsequently, the calibrated model is employed to estimate the catalyst degradation during real-world FCEV operation.

In order to utilize the developed platinum degradation model for practical durability predictions, empirical parameters need to be calibrated. This calibration process involves comparing the model results to relevant measured and empirical data from the literature. To ensure the reliability of the model, a selection of cathode catalyst AST voltage cycle waveforms, UPLs, LPLs, and cell temperatures have been chosen for calibration. It is crucial to note that carbon corrosion has been shown to have a negligible contribution to catalyst degradation at lower potentials, specifically below the OCV [12]. Considering this, all the AST cycles selected for the calibration process expose the cathode to voltages below this threshold. As a result, the inclusion of carbon corrosion in the model is not necessary for the calibration procedure. In fact, the literature datasets used for calibration were specifically chosen to exclude carbon corrosion, simplifying the modeling process. Other platinum degradation mechanisms such as detachment and coagulation, which are directly associated with carbon corrosion, have also been disregarded in the model.

For the calibration process, experimental degradation analyses conducted by Ferreira et al. [105], Uchimura et al. [106], and Kocha [107] have been considered. Ferreira et al. [105] performed an AST at 80℃ using a triangular voltage profile with a scan rate of 20 mV s^{-1}. The UPL and LPL were set at 1 V and 0.6 V, respectively. On the other hand, Uchimura et al. [106] and Kocha [107] carried out square wave potential cycles with a 2.5 s hold at the LPL (0.6 V) and

a 10 s hold at the UPL (0.95 V). Figure 4.1 illustrates the potential cycles employed by Ferreira et al. [105] (Figure 4.1a) and Uchimura et al. [106] and Kocha [107] (Figure 4.1b), which serve as the basis for the calibration process.

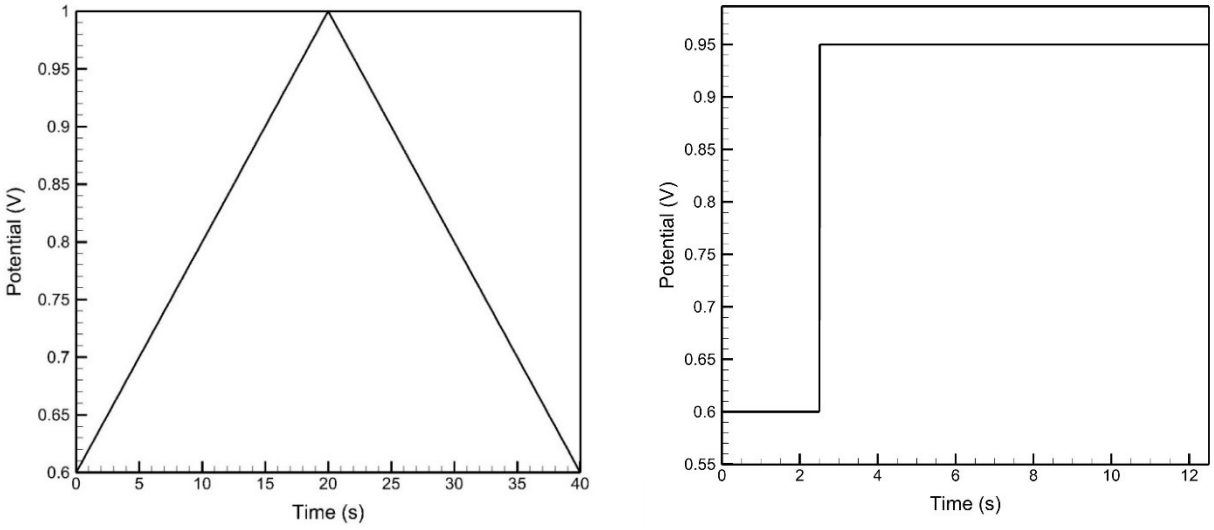

(a) (b)

Figure 4.1: The potential cycles employed experimentally by (a) Ferreira et al. [105] and (b) Uchimura et al. [106] and Kocha [107].

As previously mentioned, the platinum degradation model puts the PRD function into effect to capture the Ostwald ripening phenomenon by considering a collection of particles with different sizes. In this model, the radius of platinum particles within the BOL cathode catalyst layer is assumed to range between 0 and 10 nm, based on the PRD obtained from TEM images. To discretize the particle size range, a number of equidistant radii are distributed between the lower and upper bounds. Choosing an appropriate number of radii ensures that the model solution is independent of the number of radii used. To this end, the effect of the number of radii on the platinum ion concentration is investigated by separately running the model for the triangular potential cycle (Figure 4.1a) at 80℃, considering 15, 25, 50, and 100 radii. The resulting Pt^{2+} concentration for different radii is depicted in Figure 4.2 [108]. The analysis indicates that a reliable solution is obtained when the number of radii is equal to or greater than 50. Therefore, to optimize computational efficiency, the model considers 50 radii within the platinum particle size range. This

choice strikes a balance between accuracy and computational cost, ensuring reliable results for the platinum degradation model.

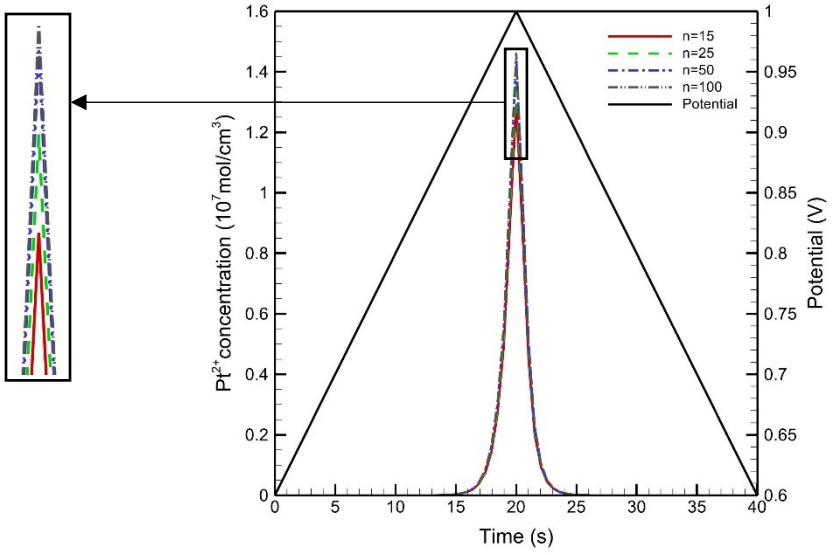

Figure 4.2: Pt ion concentration for different numbers of Pt particle radii for the triangular potential cycle in Figure 4.1a.

Figure 4.2 provides valuable insights into the platinum ion generation and Ostwald ripening phenomenon during a potential cycle. It shows that there is a threshold potential required for the generation of platinum ions. Additionally, the figure illustrates the occurrence of Ostwald ripening, which involves the dissolution of small platinum particles as the dominant degradation mechanism during the ramp-up portion of the potential cycle. Conversely, during the ramp-down part of the potential cycle, the platinum ions are observed to vanish, indicating the redeposition of these ions onto the larger particles. For the calibration process, the ECSA losses over time reported in [105], [106], [107] are compared to the ECSA losses obtained from the present model. The calibration is performed progressively due to the interdependence between platinum degradation and oxide formation. This coupling necessitates simultaneous calibration of parameters related to both platinum degradation and oxide formation. This process involves utilizing literature datasets from various potential cycles, such as triangular and square waves with different LPLs and UPLs, as well as different temperatures. This approach ensures the reliability of the calibration process for both platinum degradation and oxide formation. By varying the UPL while keeping the LPL constant during the calibration process, the model can specifically capture and characterize the platinum degradation aspect. This allows for a detailed understanding of how the platinum

degradation changes with different upper potential limits. Similarly, by varying the LPL while keeping the UPL constant, the model can accurately calibrate and capture the oxide formation process. Additionally, by applying different temperatures during the calibration, the model can demonstrate its reliability and functionality across a wide range of operating temperatures. This ensures that the model can accurately predict the degradation behavior under various temperature conditions commonly encountered in fuel cell applications. Figure 4.3 depicts the calibration results with the selected literature works, and Table 4.1 provides the values of the tuned empirical parameters and physical properties used in the model [108].

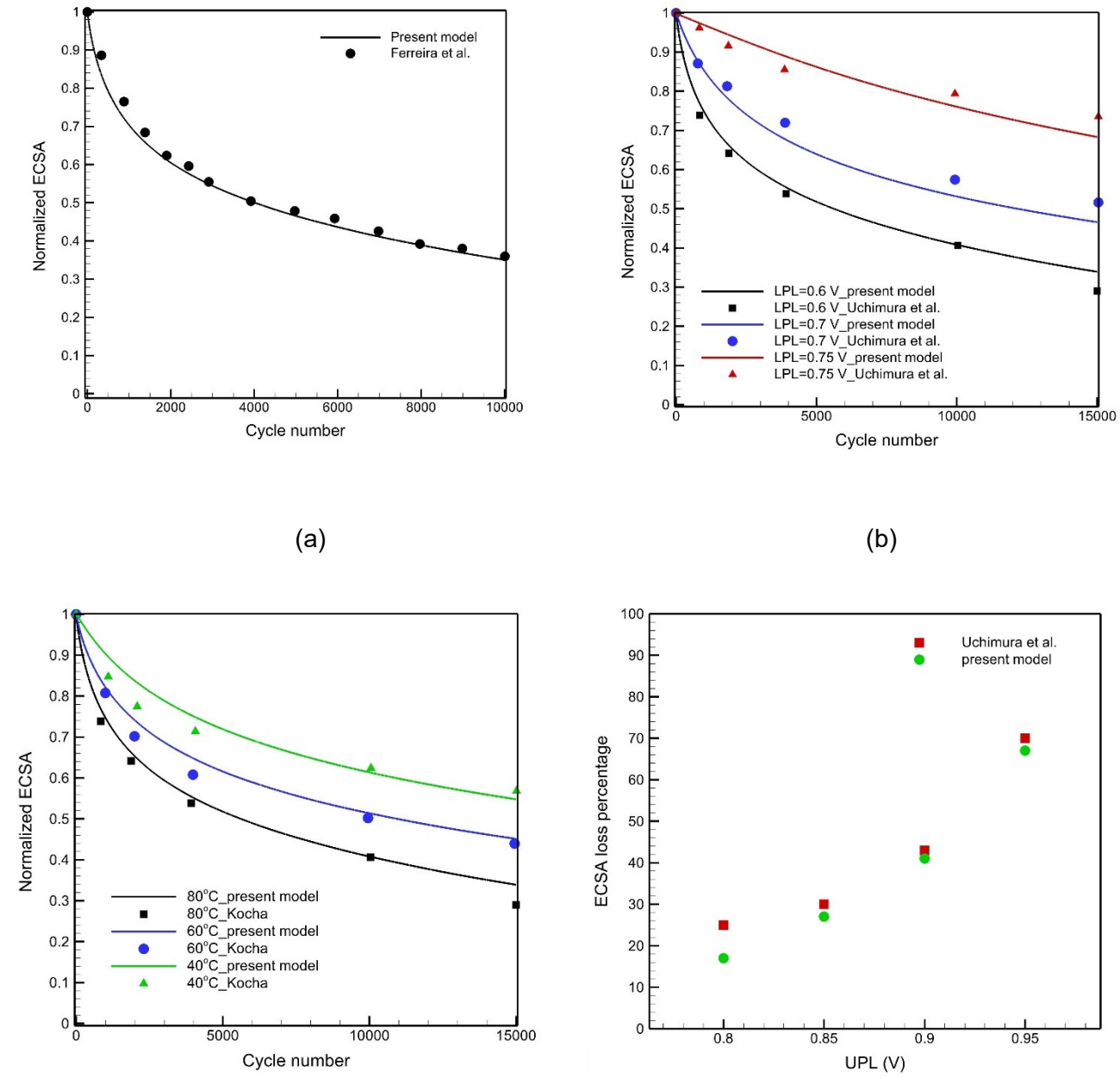

Figure 4.3: Results of model calibration with selected works: (a) under the triangular wave potential cycle shown in Figure 4.1a at 80℃ with Pt loading of 0.4 mg cm^{-2} [105]; (b) under the square wave potential cycle shown in Figure 4.1b for different LPLs at UPL = 0.95 V and 80℃ with Pt loading of 0.35 mg cm^{-2} [106]: (c) under the square wave potential cycle shown in Figure 4.1b with Pt loading of 0.35 mg cm^{-2} at different temperatures for UPL = 0.95 V and LPL = 0.6 V [107]; and (d) under the square wave potential cycle shown in Figure 4.1b for different UPLs at LPL = 0.6 V and 80℃ with Pt loading of 0.35 mg cm^{-2} after 15,000 potential cycles [107] [108].

Table 4.1: Physical properties and tuned empirical parameters used in the calibrated Pt degradation model.

Parameter	Value	Unit	Reference	Description
$k_{0,dis}$	1.5×10^{-10}	mol/(cm^2.s.K)	Fitted	Forward dissolution rate constant
ΔG_{dis}	0.12	eV	Fitted	Activation energy of dissolution
k_r	1	-	Fitted	Reverse dissolution rate constant
$k_{0,ox}$	6×10^{-12}	mol/(cm^2.s.K)	Fitted	Forward oxide formation rate constant
ΔG_{ox}	0.12	eV	Fitted	Activation energy of oxide formation
$k_{ox,r}$	0.39	-	Fitted	Reverse oxide formation rate constant
k_B	8.6×10^{-5}	eV/K	Ref. [85]	Boltzmann constant
k_{cdis}	1×10^{-14}	mol/(cm^2.s)	Fitted	Chemical dissolution rate constant
α_a	0.5	-	Ref. [17]	Anodic charge transfer coefficient
α_c	0.5	-	Ref. [17]	Cathodic charge transfer coefficient
n	2	-	Ref. [17]	Number of transferred electrons
F	96485	c/mol	Ref. [17]	Faraday's constant
R	8.314	J/(mol.K)	Ref. [37]	Gas constant
φ_{dis}^{θ}	1.188	V	Ref. [86]	Standard equilibrium potential of dissolution reaction
φ_{ox}^{θ}	0.98	V	Ref. [86]	Standard equilibrium potential of oxide reaction
$\Delta\mu_{PtO}^{0}$	-42.3	kJ/mol	Ref. [37]	A constant in Equation 2.8
σ_{Pt}	2.4×10^{-4}	J/cm^2	Ref. [42]	Platinum surface tension
M_{Pt}	195.084	g/mol	Ref. [42]	Platinum molar mass
ρ_{Pt}	21.45	g/cm^3	Ref. [42]	Platinum density
ω	3×10^{4}	J/mol	Ref. [37]	PtO-PtO interaction energy
Γ_{max}	2.18×10^{-9}	mol/cm^2	Ref. [37]	Platinum surface site density
$c_{Pt^{2+},ref}$	1	mol/cm^3	Ref. [42]	Reference platinum ion concentration

The results obtained from the present predictive model demonstrate its reliability and accuracy across various potential cycle types (e.g., triangular and square wave cycles), LPLs, UPLs, and temperatures. As shown in Figure 4.3, the platinum degradation rate increases with higher UPLs (at a constant LPL), higher temperatures, and lower LPLs (at a constant UPL). This indicates that these factors have a significant influence on the degradation process. Furthermore, the effects of

LPL and temperature on PRD, platinum oxide formation, and platinum ion concentration are illustrated in Figure 4.4 [108]. In particular, Figure 4.4c highlights the strong influence of voltage on the formation of the oxide layer over the platinum surface, suggesting that a higher voltage leads to a larger fraction of the platinum surface being covered with oxide species. When the LPL is set to 0.6 V, a significant decrease in oxide coverage is observed during the lower potential hold time. However, when the LPL is adjusted to 0.75 or 0.7 V, the drop in oxide coverage during the same hold time is much less pronounced. This phenomenon has a noticeable impact on the degradation rate, suggesting that the specific value of the LPL can significantly influence the degradation behavior of the platinum catalyst. When the voltage is cycled between 0.6 and 0.95 V, a higher degradation rate is observed compared to the other cases. This is because the oxide coverage on the platinum surface is effectively removed from the platinum surface when the potential reaches the lower limit of 0.6 V. However, when the LPL is set to 0.75 V or 0.7 V, the platinum surface remains consistently covered with oxide species. This continuous oxide coverage provides a protective layer and reduces the exposure of the platinum to degradation processes. Consequently, the degradation rate is lower in these cases compared to when the voltage range includes a lower limit of 0.6 V. The behavior described is supported by the findings presented in Figures 4.3b, 4.4a, and 4.4d. These figures demonstrate that when the LPL is lowered, a greater extent of ECSA loss, platinum particle growth, and platinum ion generation is observed in each potential cycle while the UPL is maintained constant. In contrast, it is known that a high coverage of oxide species can hinder degradation, and this is reflected in the model through the term $(1 - \theta_{PtO}(r))$ in Equation 2.4. This is evident in Figures 4.4c and d, which demonstrate that the formation of platinum ions during each potential cycle is slowed down by an increase in oxide coverage over time (specifically at LPL = 0.75 V). The oxide coverage acts as a protective layer, reducing the rate of platinum ion formation and thereby slowing down the degradation process. As mentioned earlier, the cell temperature has a notable impact on platinum degradation. The model takes into account temperature-dependent reaction rate constants and the influence of temperature on the Tafel slope. Figures 4.4b and 4.4d clearly demonstrate that increasing the temperature from 60 to 80℃ results in more significant platinum particle growth and higher platinum ion generation during each voltage cycle, indicating a greater level of platinum degradation at 80℃. However, the temperature has a negligible effect on the fractional coverage of oxide species over the platinum surface shown in Figure 4.4c.

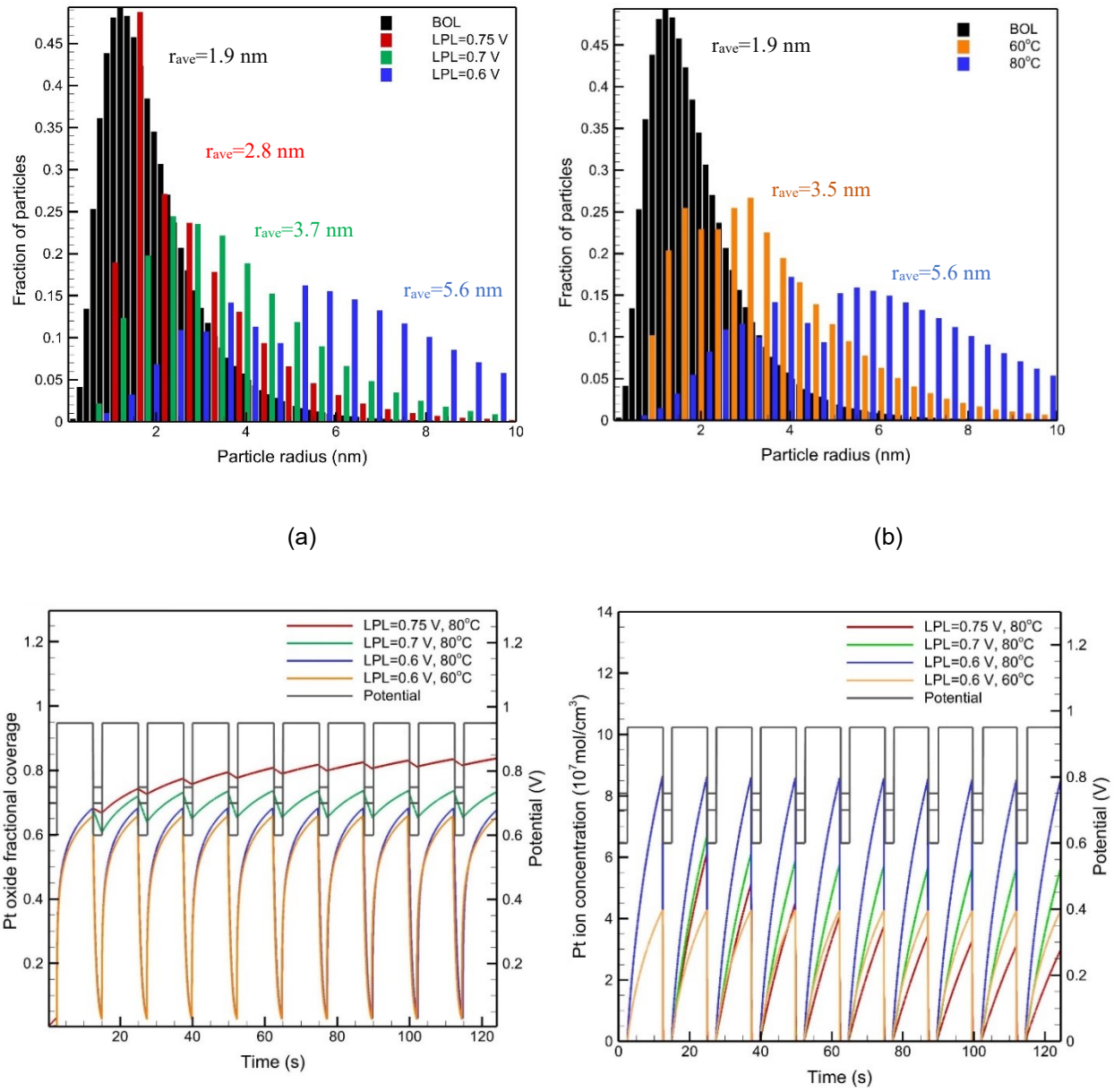

Figure 4.4: Simulated effects of LPL and cell temperature on the Pt degradation under the square wave potential cycle shown in Figure 4.1b with UPL = 0.95 V: (a) PRD for BOL and EOT with three different LPLs at 80℃; (b) PRD for BOL and EOT at two different temperatures for LPL = 0.6 V; (c) Pt oxide fractional coverage averaged over all particle sizes; and (d) Pt ion concentration [108].

4.1. Catalyst degradation under FCEV drive cycle

The obtained results from AST provide valuable understanding into the physical and electrochemical processes involved in catalyst degradation. However, it is crucial to consider that these results may differ significantly from the actual potential cycles experienced during the operation of FCEVs. In order to analyze catalyst degradation under real-world operating conditions, a drive cycle corresponding to the vehicle's velocity profile over time is considered. A drive cycle refers to the recorded vehicle velocity profile during a specific operational condition over a period of time. The calculation of the required fuel cell potential for a given drive cycle involves using the specifications of the fuel cell stack and the vehicle. In order to analyze catalyst degradation under real-world operating conditions, a transit bus drive cycle is investigated. Specifically, a transit bus line that operates in the city of Victoria, B.C., Canada, and travels between the city centre and the University of Victoria is chosen for the degradation analysis. This particular bus route provides a representative scenario for studying the catalyst degradation in a transit bus application. Figure 4.5 illustrates the recorded drive cycle of the bus, including data from both the northbound and southbound directions of the same route along with the road elevation [109]. The road elevation data is employed to calculate the road angle at any point. The characteristics of the transit bus and fuel cell stack assumed for the analysis are summarized in Table 4.2.

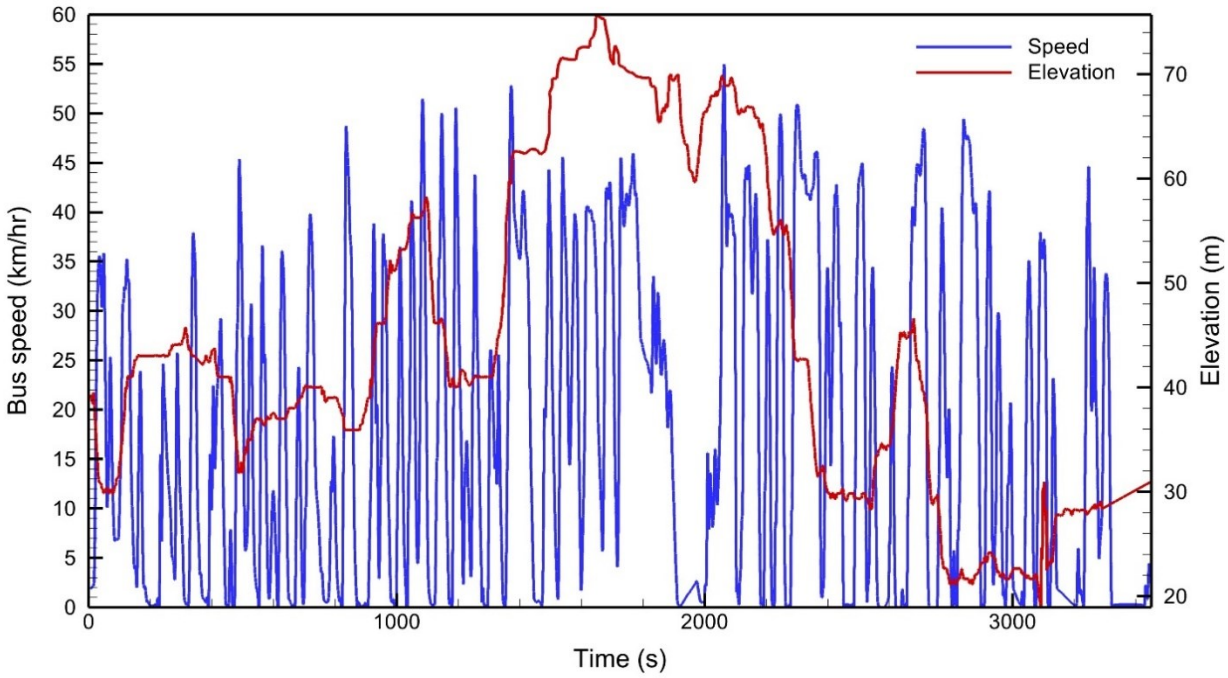

Figure 4.5: The drive cycle of the transit bus operating in Victoria, B.C [109].

Table 4.2: The transit bus and fuel cell characteristics.

Bus mass (kg)	15,500 [110]
Frontal area (m^2)	8.8 [109]
Powertrain and stack efficiencies	80%
Auxiliary power (kW)	20 [111]
Drag coefficient	0.6 [109]
Platinum loading (mg cm^{-2})	0.4

As mentioned earlier, the impact of carbon corrosion on catalyst degradation is found to be minimal under lower potentials or low temperatures. The voltage profile obtained from the drive cycle analysis confirms that the voltage levels during the load cycle do not exceed the threshold for carbon corrosion. This indicates that the operating conditions during the load cycle do not induce significant carbon corrosion. The only potential cycle where carbon corrosion may occur is during SU/SD, when higher voltages above the open circuit voltage (OCV) are experienced. However, in transit bus applications, SU/SD cycles are relatively shorter and less frequent compared to the load cycles. Additionally, these cycles typically occur at lower temperatures, which further reduces the carbon corrosion rate. Furthermore, recent advancements in materials

have made significant progress in addressing the issue of carbon corrosion by developing carbon materials that are more resistant to corrosion [112].

To accurately calculate the cell voltage needed to meet the drive cycle requirements, considering fuel cell polarization curves at various operating temperatures is essential. It is anticipated that higher cell temperatures, reaching around 90℃, would enhance the fuel cell performance due to the decrease in activation energy with increasing temperature. Several research studies have examined the impact of temperature on fuel cell performance. In this study, the fuel cell performance and polarization curves obtained from the experimental work conducted by Sun et al. [113] are utilized. Figure 4.6 illustrates the effect of temperature on polarization curve.

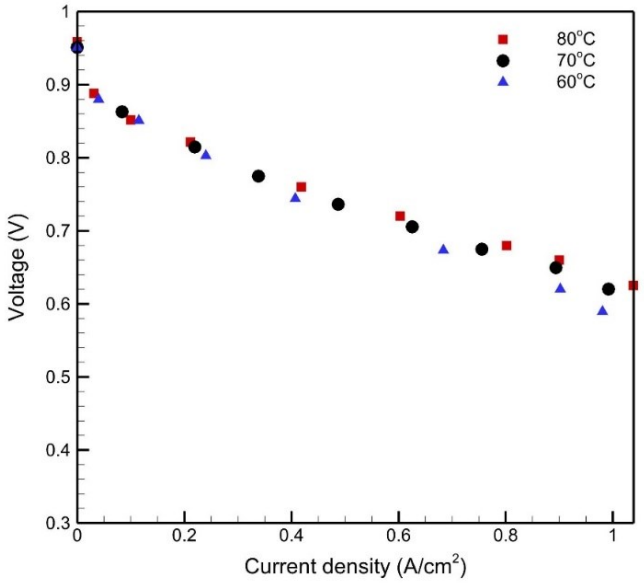

Figure 4.6: The fuel cell polarization curves for different temperatures reported by [113].

The power density and cell voltage for different stack sizes can be calculated using the drive cycle depicted in Figure 4.5, following the methodology outlined in Section 2.3. It is assumed that the fuel cell performance is consistent across all cells within the stack. The stack size is represented by the stack nominal power, which is defined as the electrical power output of the stack under normal operating conditions.

$$P_N = N_{cell} A_{cell} p_{max} \tag{4.1}$$

where P_N and p_{max} denote the stack nominal power and maximum power density generated by each cell, respectively.

The transit bus drive cycle depicted in Figure 4.5 is characterized by frequent stops, resulting in short periods of speed reduction. During these deceleration and stop phases, the fuel cell stack is primarily responsible for supplying the minimum required power, which is the auxiliary power needed for various functions. As a result, the fuel cell stack operates at the highest cell potential (i.e., UPL), during these periods. Likewise, the highest power demand, which typically occurs during periods of rapid acceleration, results in the fuel cell stack operating at the lowest cell potential (i.e., LPL). The calculated power density and cell voltage (at BOL) for a fuel cell stack with a nominal power of 264 kW at 80°C are presented in Figure 4.7.

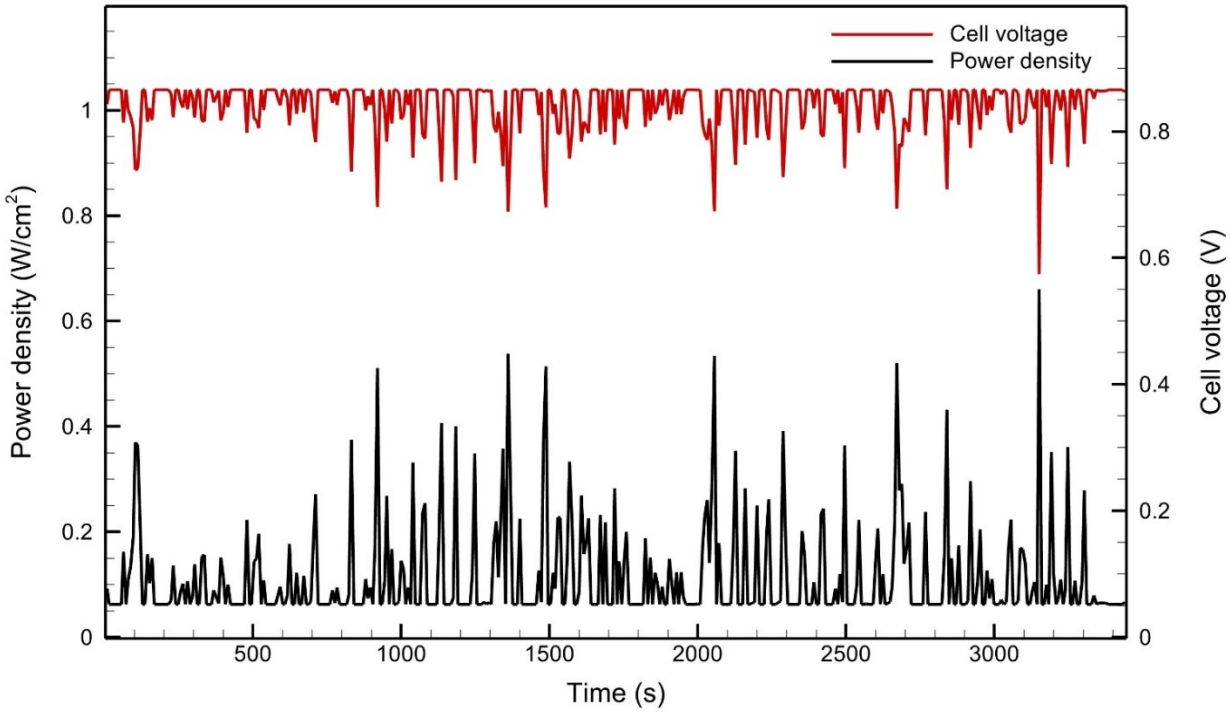

Figure 4.7: The calculated power density and cell voltage for a fuel cell stack with a nominal power of 264 kW at 80°C, subjected to the transit bus drive cycle shown in Figure 4.5 [108].

In order to ensure the reliability of the numerical simulation, a time step dependency analysis is conducted prior to running the drive cycle simulation. Three different time steps are considered: 8, 4, and 2 seconds. The numerical degradation analysis is then performed separately for a stack with a nominal power of 198 kW using these different time steps. The analysis reveals that for

time steps equal to or below 4 seconds, the change in ECSA over time becomes independent of the time step value. Based on this observation, a time step of 4 seconds is selected for the drive cycle analysis to ensure both simulation accuracy and computational efficiency in capturing the degradation dynamics of the fuel cell stack during the drive cycle simulation. Figure 4.8 illustrates the results of the ECSA decay over time for different time steps.

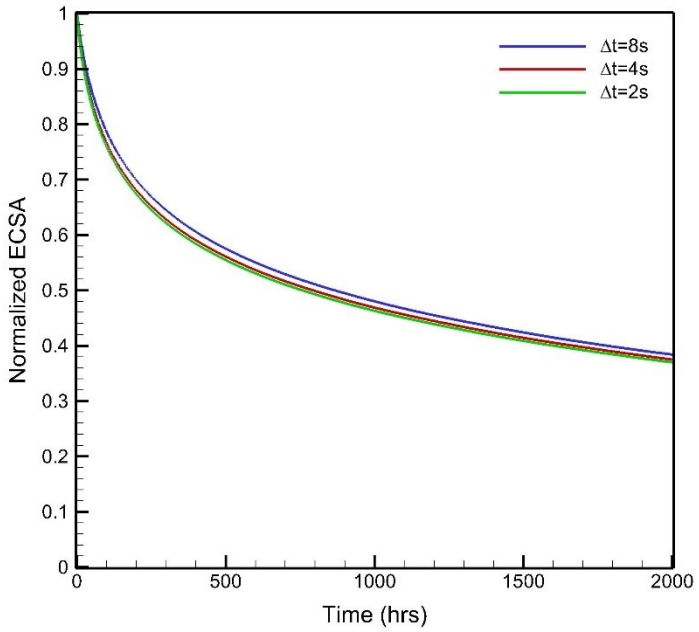

Figure 4.8: Simulated ECSA degradation with time for different time steps for a stack with a nominal power of 198 kW at 80℃.

4.1.1. Effect of stack size on ECSA degradation

To examine the impact of stack size on catalyst degradation, five different nominal powers (132, 198, 264, 330, and 396 kW) are selected. These power levels are chosen to ensure that they all meet the performance demands of the drive cycle. As the fuel cell stack size is increased, the required power density decreases, resulting in an increase in the cell voltage, as per the conventional fuel cell performance. Figure 4.9 displays the cell voltage profiles for three different stack sizes.

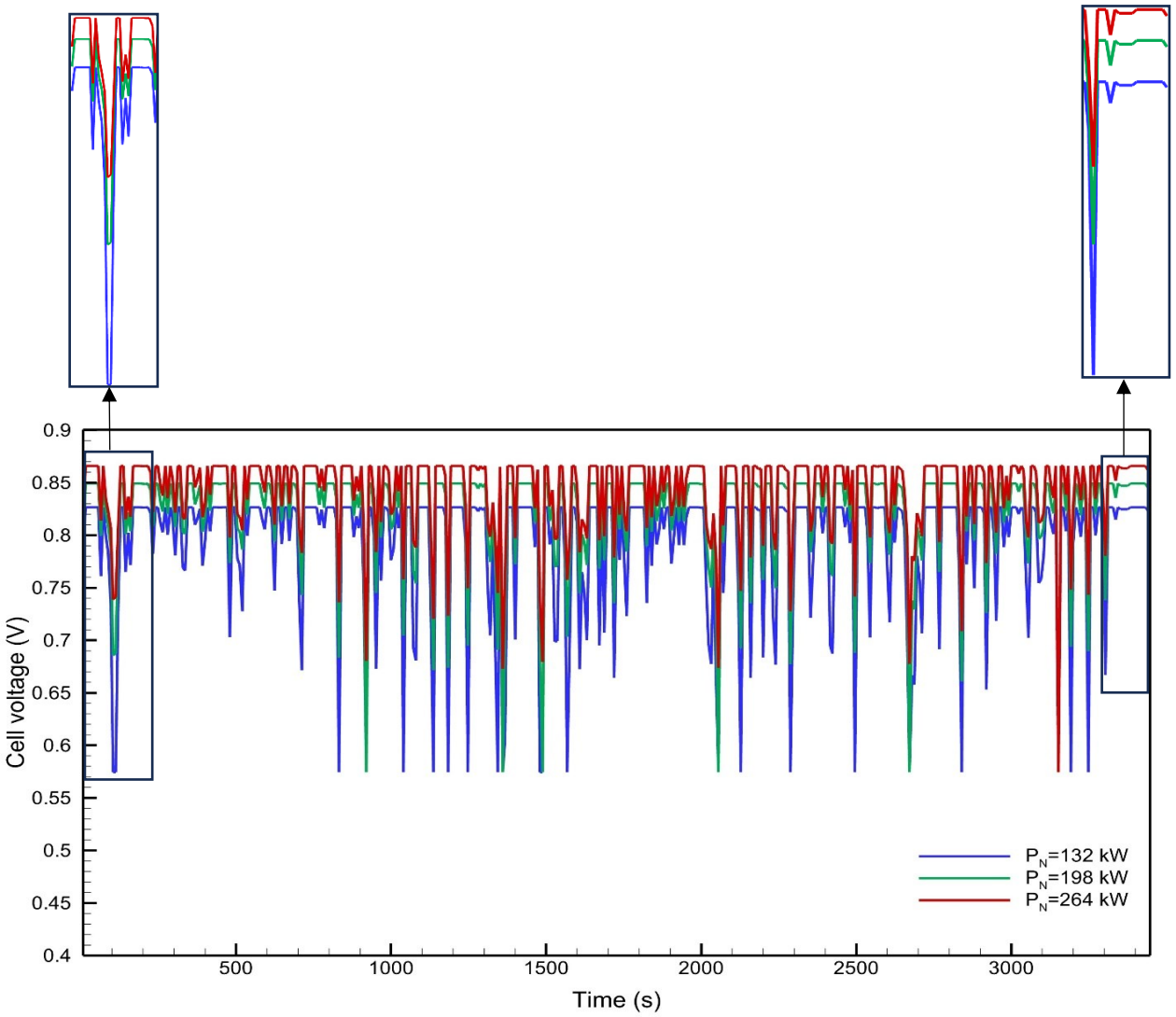

Figure 4.9: The cell voltage profiles for different stack sizes at 80℃ [108].

The cell voltage profiles obtained from the drive cycle are utilized as input for the degradation model. The degradation model is separately run for each of the specified stack sizes at 80℃. At each time step, the model calculates the remaining ECSA, platinum oxide fractional coverage, and platinum ion concentration. The results of these calculations are presented in the Figure 4.10 [108]. Figures 4.10a and 4.10c illustrate that the rate of ECSA decay over time increases as the stack size increases from 132 kW to 396 kW. This observation results from the potential cycle changes for different stack sizes shown in Figure 4.9. As the stack size increases, the corresponding higher UPLs result in a more significant ECSA loss over time. This is primarily attributed to the accelerated dissolution and redeposition of platinum, which occurs more rapidly at higher UPLs. Therefore, larger stacks experience a more pronounced ECSA degradation over

time. On the other hand, Figure 4.10b reveals that the oxide coverage over the platinum surface increases with the stack size at a given time due to the higher potentials experienced. This suggests that larger stacks exhibit a greater extent of oxide formation on the platinum surface. The increase in oxide coverage reduces the exposed surface area of platinum, resulting in a decrease in ECSA degradation. Therefore, the rate of ECSA degradation slows down as the stack size increases. Figure 4.10d illustrates the cell voltage degradation over time due to ECSA loss at a current density of 0.5 A cm^{-2}, as calculated using Equation 2.38. The degradation in performance closely follows the trends in ECSA decay, as anticipated, and is in good agreement with the measured voltage losses reported in the literature for degraded ECSA levels at lower current densities, such as 0.5 A cm^{-2} [114].

Based on the calibrated parameters in Table 4.1, it is observed that the electrochemical dissolution mechanism is the dominant degradation mechanism in all simulated stacks shown in Figure 4.10, and is responsible for approximately 99% of the overall degradation rate on average. This finding indicates that the contribution of chemical degradation is negligible, which is in agreement with the previous findings in the literature [37].

Furthermore, it is observed that the degradation rates are higher at the beginning of the simulation and gradually decrease over time. This can be attributed to the gradual performance degradation of the fuel cell, which leads to higher current densities required to deliver the desired power. As the fuel cell operates at lower degraded voltages, the degradation rate is reduced over time.

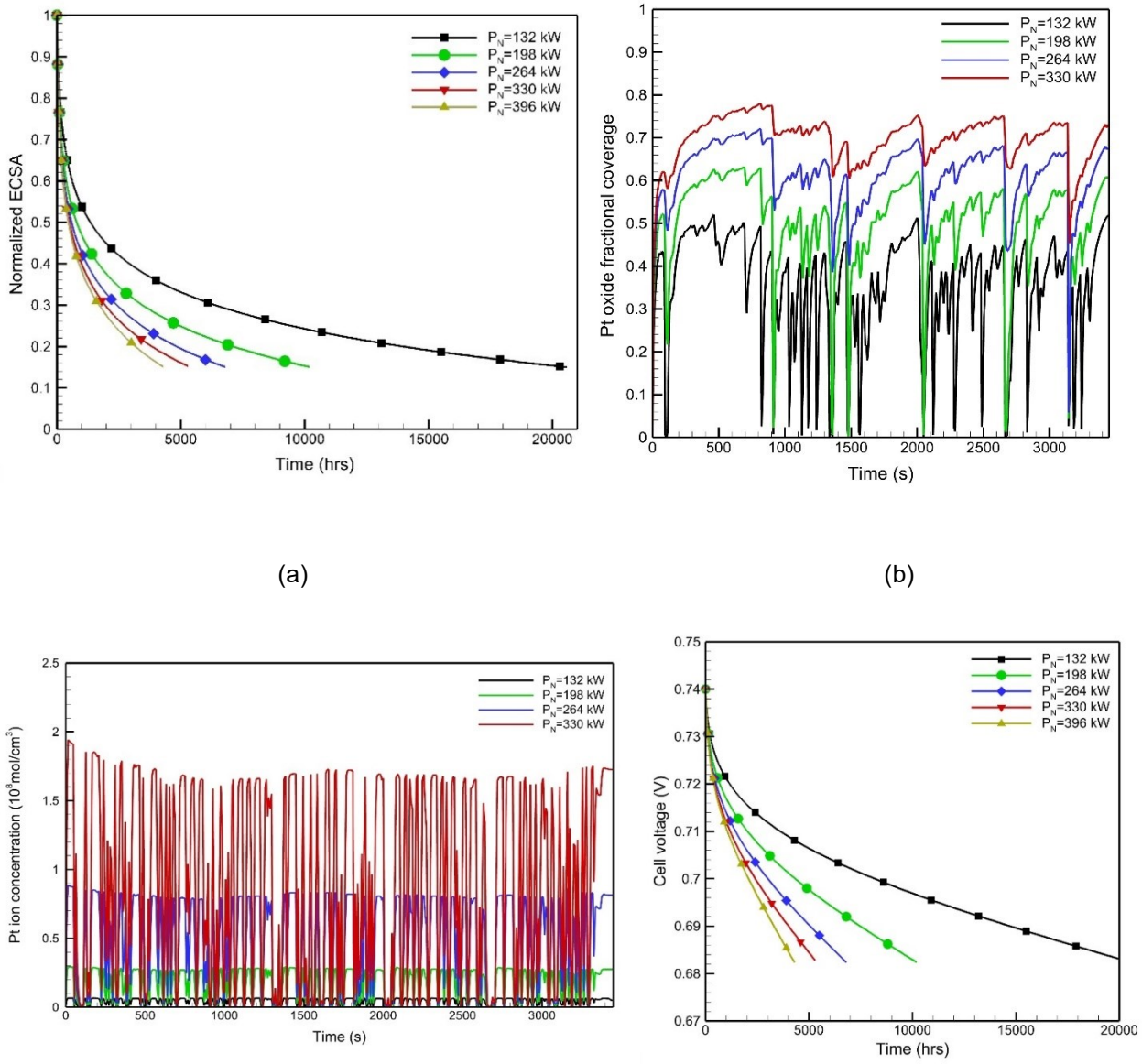

Figure 4.10: Simulated effect of stack size on cathode catalyst degradation under fuel cell transit bus operation at 80℃ under the drive cycle shown in Figure 4.5: (a) normalized ECSA decay with time for the complete simulation time; (b) Pt oxide fractional coverage averaged over all particle sizes with time for one drive cycle; (c) Pt ion concentration with time for one drive cycle; and (d) cell voltage degradation over time at 0.5 A cm^{-2} [108].

4.1.2. Effect of temperature on ECSA degradation

To investigate the impact of stack temperature on ECSA loss, the degradation model is applied separately with three different temperatures (60, 70, and 80℃). These simulations are conducted for a stack with a nominal power of 264 kW under the same transit bus drive cycle. The corresponding polarization curve for each temperature is used in the analysis (Figure 4.8). The simulation results shown in Figure 4.11 illustrate a significant increase in ECSA loss as the temperature is raised (Figures 4.11a, c, and d) [108]. This observation is in agreement with the reaction rate equations used in the Butler-Volmer approach. At higher temperatures, the platinum dissolution and redeposition mechanisms are expected to occur at a faster rate, leading to accelerated platinum degradation. The oxide coverage, on the other hand, is not substantially impacted by the temperature as shown in Figure 4.11b. Similar to the previous cases, the dominant mechanism of platinum degradation is found to be the electrochemical platinum dissolution and redeposition, accounting for an average contribution of 99.1% to the overall degradation rate.

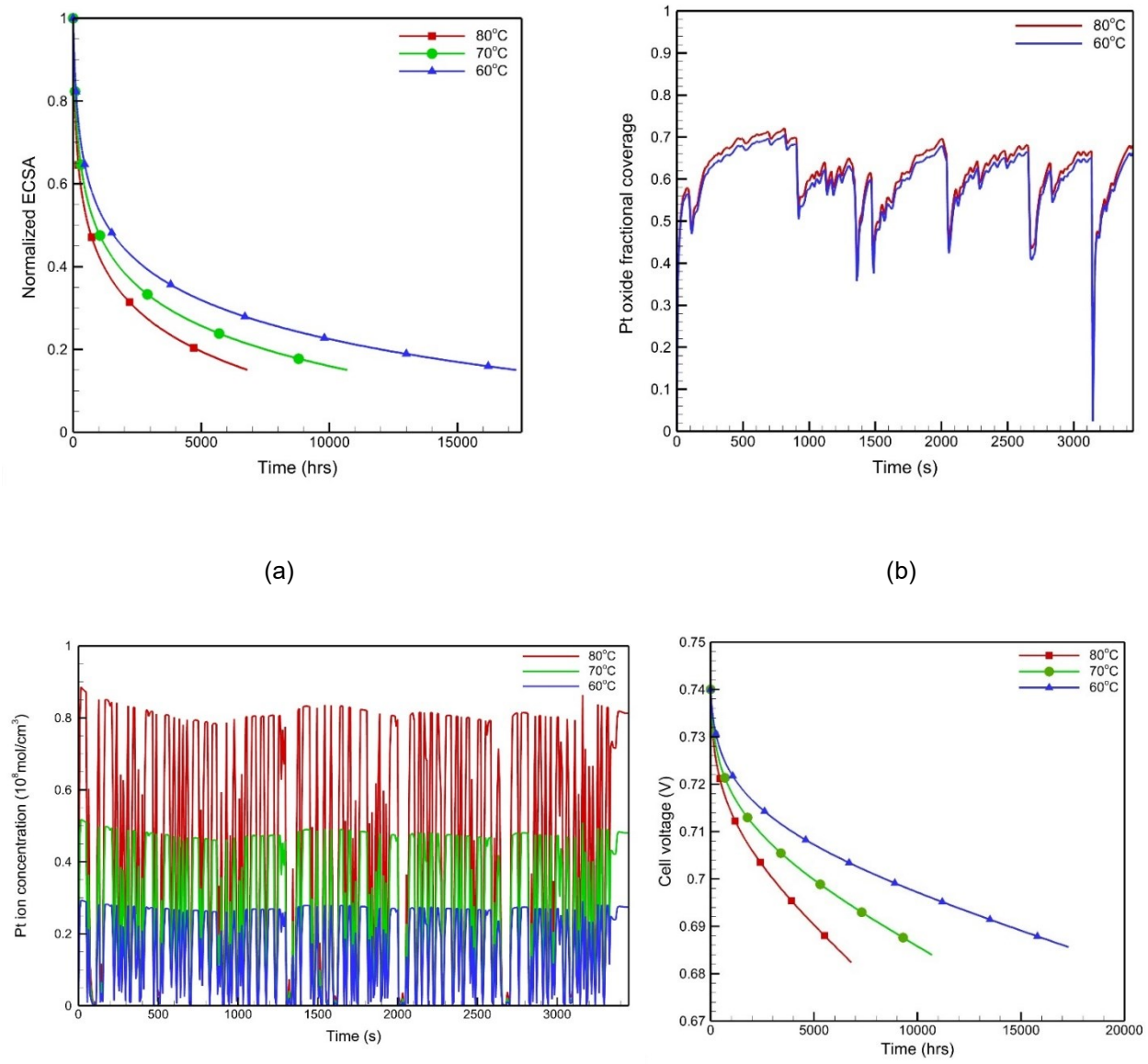

Figure 4.11: Simulated effect of stack temperature on cathode catalyst degradation under fuel cell transit bus operation for a stack with a nominal power of 264 kW under the drive cycle shown in Figure 4.5: (a) normalized ECSA decay with time for the complete simulation time; (b) Pt oxide fractional coverage averaged over all particle sizes with time for one drive cycle; (c) Pt ion concentration with time for one drive cycle; (d) cell voltage degradation over time at 0.5 A cm^{-2} [108].

4.1.3. Estimation of stack lifetime affected by cathode degradation

The stack lifetime for the fuel cell transit bus drive cycle is estimated based on the simulated cathode catalyst degradation using a failure criterion of a 10% cell voltage drop at a constant current density of 0.5 A cm^{-2}. This criterion is used to determine the point at which the degradation reaches a level that is considered unacceptable by US DOE for the desired performance of the fuel cell stack. Wang et al. [114] developed a model that correlates the voltage drop with the ECSA loss and validated it. Their study found that a 10% voltage drop at 0.5 A cm^{-2} corresponds to an 85% ECSA loss, using a similar polarization curve as in the present study. This finding aligns with the results obtained in this work (Figures 4.10 and 4.11). Therefore, the cathode lifetime is estimated based on the criterion of an 85% ECSA loss. Figure 4.12 presents the estimated stack lifetimes for each scenario [108]. As shown in Figure 4.12a, the lifetime decreases non-linearly from 20,600 to 4,300 hours at 80℃ as the stack nominal power increases from 132 to 396 kW. Additionally, Figure 4.12b demonstrates that increasing the cell temperature from 60 to 80℃ results in a 61% reduction in lifetime for a stack with a nominal power of 264 kW.

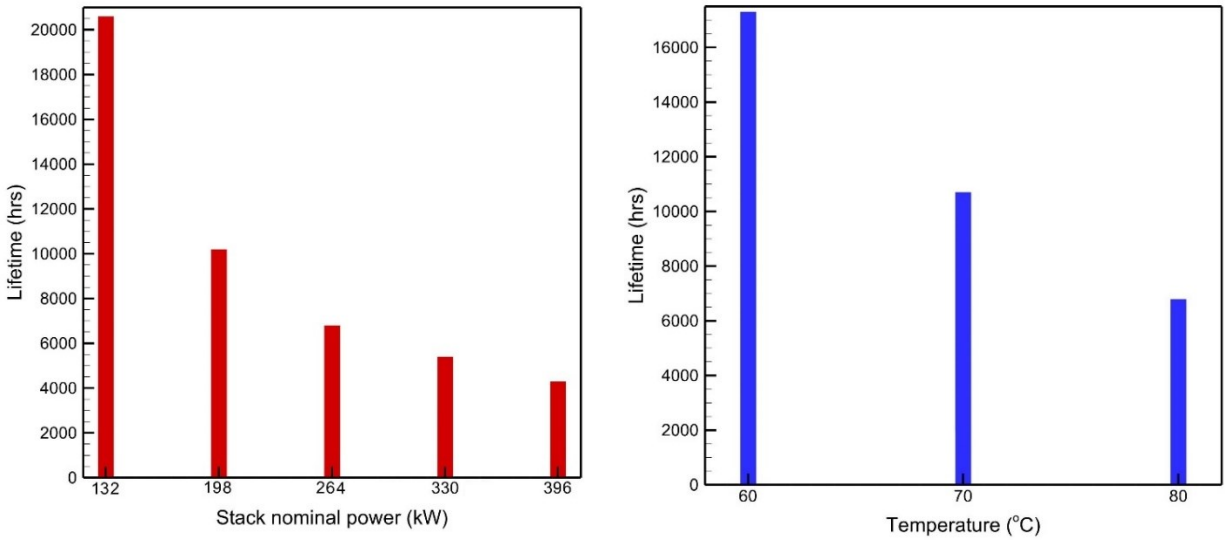

(a) (b)

Figure 4.12: Effects of (a) stack size at 80℃ and (b) stack temperature for the 264-kW stack on the estimated stack lifetime [108].

The US DOE has set lifetime targets for fuel cell applications, including a target of 25,000 hours for fuel cell buses by 2020 [5]. However, based on the tested conditions shown in Figure 4.12, it is evident that the catalyst degradation at the cathode does not meet this target, even in the absence of other modes of fuel cell degradation. To achieve the DOE target, a strategy of operating the smallest stack at lower temperatures is considered since it allows to run the stack at the minimum achievable UPL with lower platinum dissolution and redeposition rates due to lower temperatures. It is determined that the 132-kW stack, operating at 70 and 60℃, can achieve lifetimes of 35,000 and 63,000 hours, respectively, before reaching the catalyst failure criterion. This indicates that these conditions meet and exceed the DOE requirement. Additionally, recent advancements in degradation mitigation strategies have introduced approaches such as encapsulating platinum particles within the micropores of high surface area carbon support [115]. These strategies have the potential to further enhance catalyst durability and contribute to extended lifetime of fuel cell systems.

In this chapter, the developed catalyst degradation model was calibrated with a variety of AST conditions including different potential cycles, LPLs, UPLs, and temperatures. Then, the validated model was utilized to simulate catalyst degradation under a real-world transit bus drive cycle. The stack size and temperature were found to have strong effects on catalyst degradation. Specifically, smaller stacks operating at lower temperatures were observed to experience reduced levels of degradation.

Chapter 5: Membrane degradation and lifetime

In this chapter, the membrane degradation model is first calibrated for mechanical and chemical degradation mechanisms using in-house measured accelerated stress test data. Then, the model is applied to estimate the membrane degradation and determine its lifetime under real-world FCEV operation conditions.

Cylindrical bundles with lengths of 50-100 nm are created in the network as shown by Ref. [91]. It is assumed that each bundle consists of 9 ionomer chains, which is the reported stable aggregate number according to references [83, 84]. To ensure the formation of clusters within the network, a sufficient number of bundles is required. In this work, the number of bundles is set to 20,000, following the recommendation in references [95, 96]. The critical crack length of 2,500 nm, as suggested by references [95, 96], is considered for this study. The validity of this value will be assessed in the calibration procedure section. Given the stochastic nature of the model, the simulation is repeated multiple times for each case until the standard deviation of the predictions converges to a single value. For each trial, a new network of interconnected bundles is generated. The simulations are performed on these networks, and the lifetime of each network is calculated. The average lifetime and the standard deviation of the lifetimes obtained from the simulations are then considered as the predicted lifetime and the uncertainty of the predictions, respectively.

The model parameters are determined by calibrating the model using experimental results from membrane degradation tests. The calibration process involves separately calibrating the mechanical and chemical degradation phases of the model using test results specific to each degradation mechanism. This approach simplifies and expedites the calibration process. The subsequent sections will provide a detailed explanation of the calibration procedure.

5.1. The calibration of the mechanical degradation phase

The data required for the mechanical degradation mode of the model was obtained from ΔP-AMSTs which were run by another Ph.D. student at FCReL. After finishing the experiments, the calibration of the mechanical degradation mode of the model using the measured experimental membrane lifetimes was carried out in this thesis. The ΔP-AMST method subjects fuel cell membranes to higher stress amplitudes by applying humidity cycles and a pressure differential between the cathode and anode sides. The test assembly used for ΔP-AMSTs

includes a polycarbonate spacer, a pressurized bladder, a polyimide film, a reinforced membrane with a thickness of 15 µm, and GDL. To apply the stress tests to the membrane, a fuel cell test station equipped with water-injected evaporator-type humidifiers, an end-plate heater, mass flow controllers, and a backpressure control system is used. This setup allows for precise control of the operating conditions and provides the necessary infrastructure to conduct the ΔP-AMSTs. The water-injected evaporator-type humidifiers ensure proper humidification of the reactant gases, while the end-plate heater maintains the desired temperature. The mass flow controllers regulate the flow rates of the gases, and the backpressure control system controls the pressure differential applied to the cathode and anode sides of the membrane. The membrane is subjected to consecutive humidity cycles consisting of a 60-second dry phase (RH=30%) followed by a 30-second wet phase (RH=100%). This cyclic exposure to dry and wet conditions is designed to accelerate membrane fatigue degradation based on dynamic membrane hydration changes during real-world operating conditions, whereas the applied pressure differential further reduces the test duration and facilitates stress adjustment in order to obtain fatigue lifetime curves. To eliminate any interference from chemical degradation, nitrogen is used as the carrier gas in the test. The pressure differential loss, indicating a significant decrease in pressure across the membrane, is used as the failure criterion in this test. Monitoring the pressure differential allows for the assessment of membrane degradation and the determination of its lifetime under the applied stress conditions. The details of the test setup and the experimental procedure are found in Ref. [63]. Figure 5.1 shows a schematic of the ΔP-AMST.

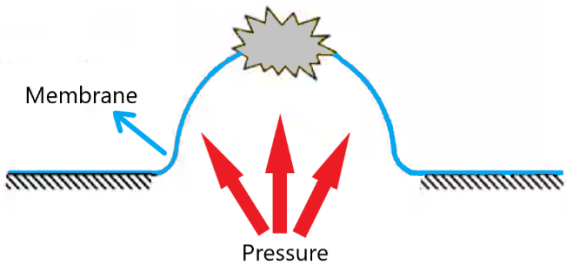

Figure 5.1: A schematic of the ΔP-AMST.

Finite element simulations are carried out to determine the initial stress distribution in the membrane under the ΔP-AMST conditions by Mazrouei et al. [116]. These simulations are based on the stress-strain curves of the membrane obtained from experimental data under different

ambient conditions. For each test, two separate simulations are performed, one for dry conditions and another for wet conditions. Hence, the maximum stress obtained from the finite element simulations for each case is used as the input stress value in Equation 2.22. The G'Sell-Jonas phenomenological model [117], [118], [119] is employed to characterize the constitutive response of the membrane. This model takes into account the effects of temperature, RH, and strain rate, all included into a single equation. The G'Sell-Jonas' model is added to the initial yield as an isotropic hardening function. Therefore, the yield stress equation used as the constitutive equation after modifying using the G'Sell-Jonas is as follows.

$$\sigma_y = \sigma_{y0} + K(T, RH)\left(1 - e^{-w(RH)\varepsilon}\right)e^{h(RH)\varepsilon^2}\dot{\varepsilon}^m \tag{5.1}$$

where σ_{y0} represents the initial yield strength, ε denotes the strain, and K, m, w, and h are all functions of temperature and RH. The material parameters in Equation 5.1 are determined through tensile tests conducted using dynamic mechanical analysis (DMA) under various conditions of temperature, humidity, and strain rates [46]. Figure 5.2 illustrates the resultant initial stress distribution across the membrane under one ΔP-AMST condition at 60℃ and a pressure differential (ΔP) of 8 kPa, considering both the dry and wet phases, and Table 5.1 shows the results of the experiments and finite elements simulations implemented by [116]. As expected, the stress is intensified with a higher ΔP. It is also understood that the stress magnitude is higher in dry cases compared to wet cases under identical conditions due to membrane contraction during dry cycles.

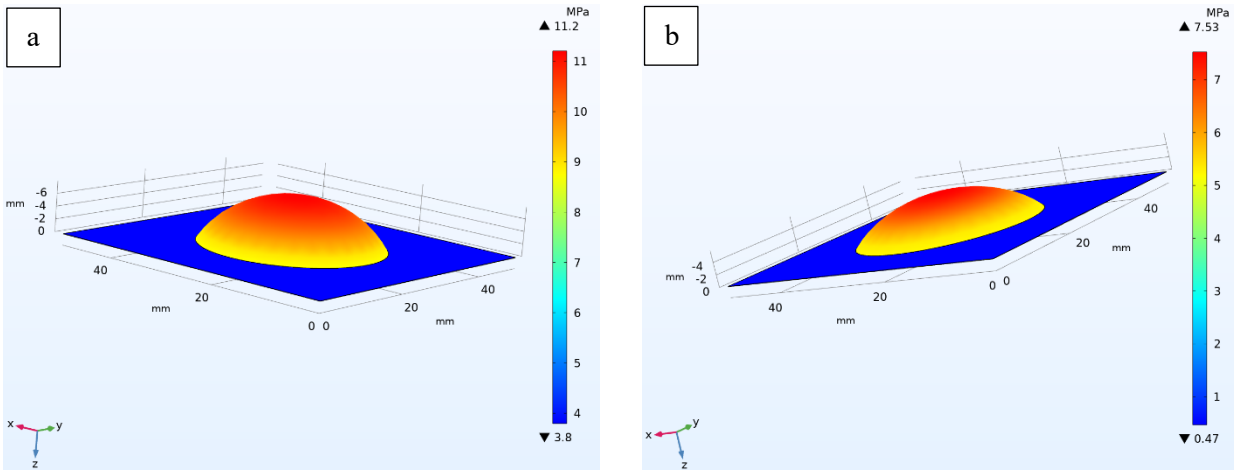

Figure 5.2: The tensile stress distribution across the membrane obtained from the finite element simulations at (a) dry and (b) wet phases of ΔP-AMST at 60℃ and ΔP=8 kPa [116].

Table 5.1: The results of the ΔP-AMSTs and finite element simulations [116].

Temperature (℃)	ΔP (kPa)	Maximum stress at wet condition (MPa)	Maximum stress at dry condition (MPa)	Lifetime (RH cycles)
90	3	2.8	5.65	3453
90	4	3.5	6.72	1605
90	5	4	7.8	1127
90	8	6	11.54	161
60	8	7.53	11.2	4122
60	11	8.5	14.7	1012
60	13	10.29	17.81	571

The tuning parameters (τ_0, E_a and ν) in the pure mechanical degradation rate equation (Equation 2.23) are adjusted based on the results obtained from the ΔP-AMSTs and finite element simulations conducted at various temperatures and pressure differentials. The wide ranges of temperatures and pressure differentials ensure the accuracy and reliability of the calibration process.

5.1.1. The utilization of optimization in calibration

The tuning parameters are adjusted using the genetic optimization algorithm using the least squares method. The objective function is defined as the sum of the squared errors between the modeling results and experimental data at each data point as below.

$$Objective\ function = \sum_{i=1}^{N}\left[\frac{L_{e,i} - L_{m,i}}{L_{e,i}}\right]^2 \tag{5.2}$$

where L_e and L_m are the lifetimes obtained from experiment and model, respectively and N is the number of data points. The design variables are the tuning parameters (τ_0, E_a and ν) in Equation 2.23. After the optimization process, the values of the tuning parameters are determined as $\tau_0 = 4.58 \times 10^{-11}$ s, $E_a = 129.06$ kJ mol^{-1}, and $\nu = 1.58 \times 10^{-27}$ m^3. Figure 5.3 shows a comparison between the results obtained from the calibrated model and the experimental data, and signifies a favorable agreement between them.

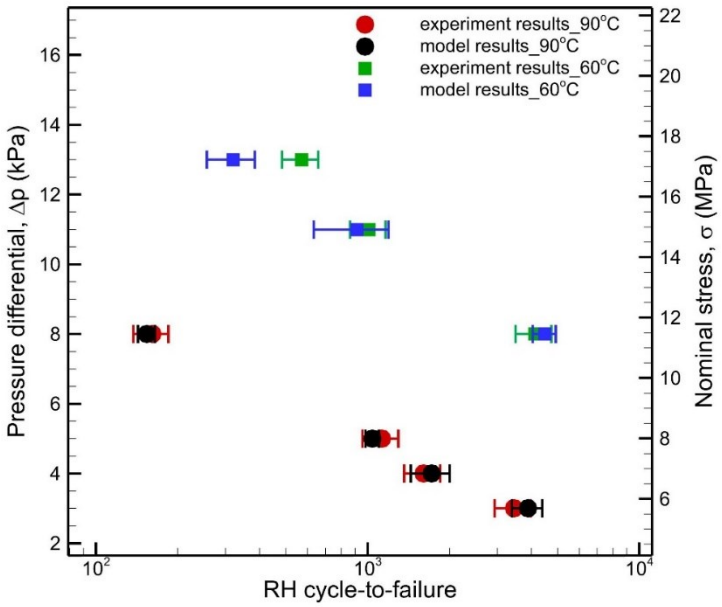

Figure 5.3: The results of the calibration of the model with the experiments under the pure mechanical degradation.

Figure 5.4 illustrates the formation and growth of clusters over time for two specific cases (ΔP=3 kPa at 90℃ and ΔP=8 kPa at 60℃). The figure shows that there is a rapid growth of a main cluster

within a specific single RH cycle, which ultimately leads to membrane failure in the form of fatigue-fracture. This phenomenon is known as the percolation of the network. Based on the observations in Figure 5.4 and analysis of other simulated cases, it is determined that a critical cluster length of 2,500 nm corresponds to membrane failure.

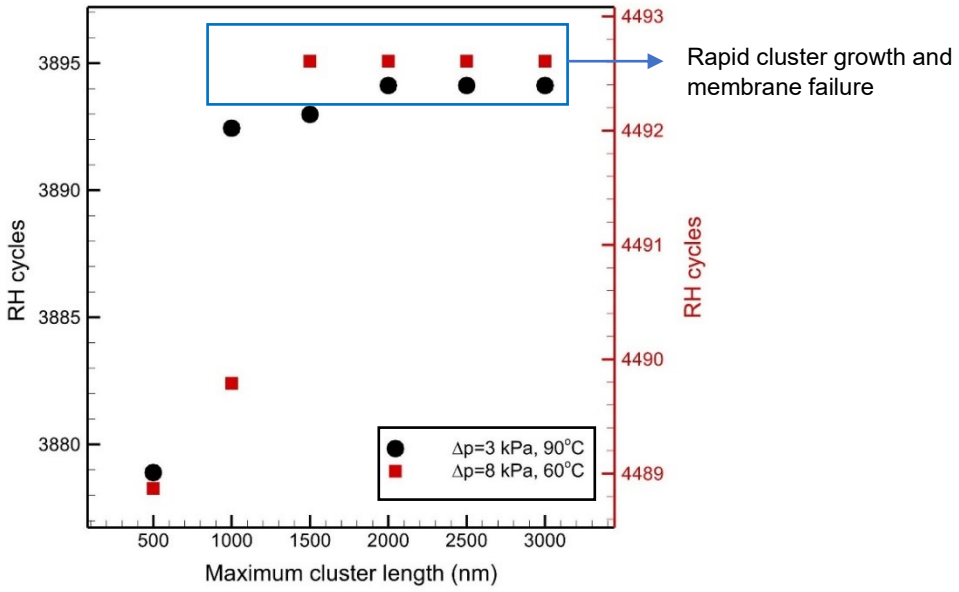

Figure 5.4: The growth of the longest cluster within the network over time for ΔP=3 kPa at 90℃ and for ΔP=8 kPa at 60℃

Figure 5.5a presents the number of failed ionomer chains and bundles over time for the ΔP-AMST case at 60℃ and ΔP=8 kPa and illustrates the significant increase in bundle failure rates during a short period of time leading up to the ultimate membrane failure. From a mechanical perspective, the presence of a defect in a material subjected to mechanical loading results in a notable concentration of stress around the defect. As a result, the likelihood of fracture occurring around the defect is significantly increased. The model takes into account this phenomenon through a non-uniform stress redistribution scheme. When a bundle fails, the adjacent bundles experience higher stress levels compared to those farther away. This leads to an increased breaking probability for the adjacent bundles due to the higher stress concentrations in their vicinity. As a result, while the initial failure of bundles may occur randomly across the membrane, subsequent bundle failures and cluster growth predominantly occur in the vicinity of the existing failed bundles. This is because the ionomer chains in the vicinity of the failed bundles have higher breaking probabilities, leading to the propagation of failures in that region. As the cluster grows,

the stress concentration around it becomes increasingly intense. This leads to a rapid increase in the stress levels within the membrane, ultimately resulting in its failure within a very short period of time after the formation of the cluster. Figures 5.5b-d depict the rapid formation and growth of clusters in the membrane, eventually leading to membrane failure.

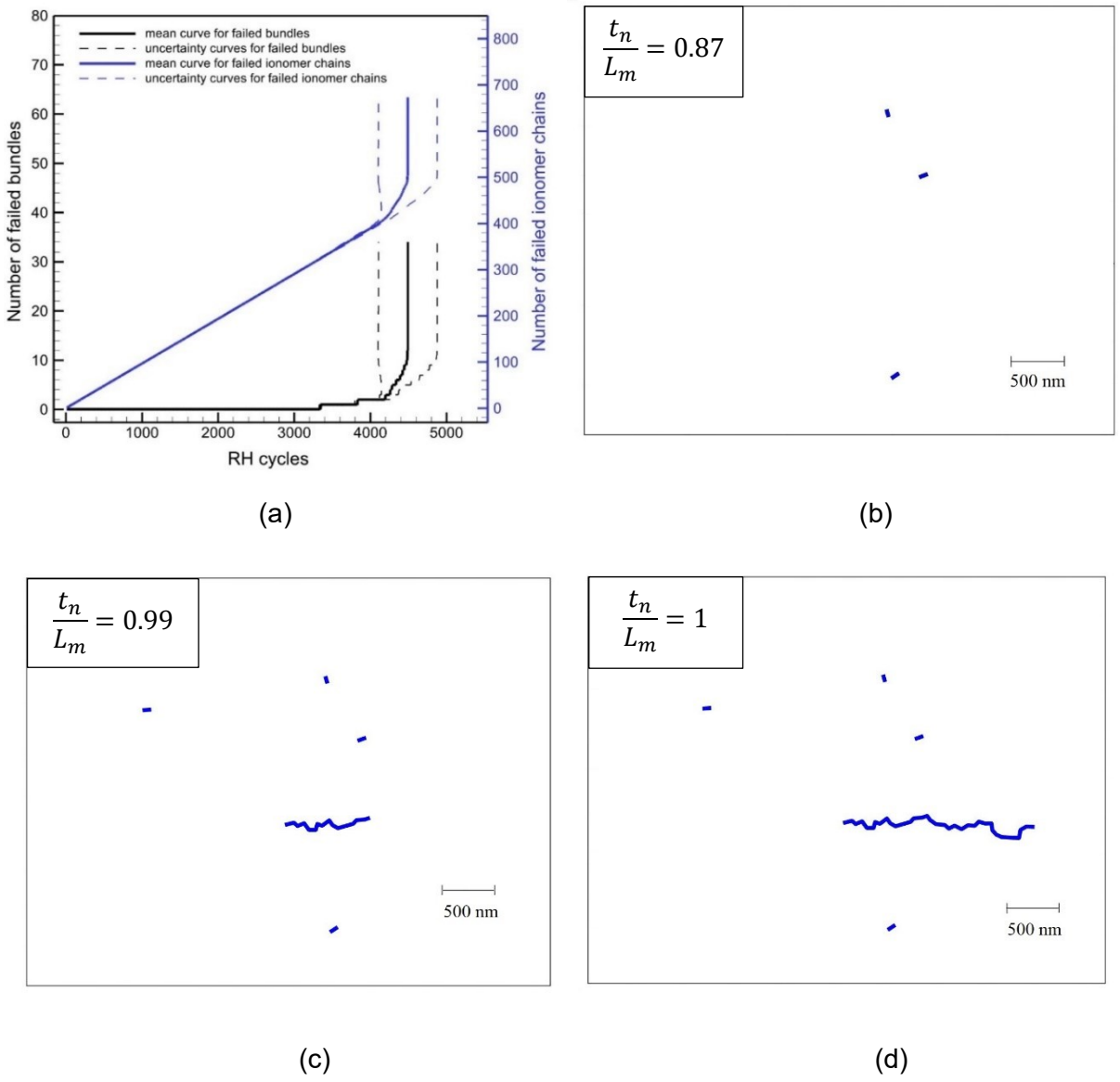

Figure 5.5: The results of the simulation of ΔP-AMST at 60℃ and ΔP=8 kPa: (a) the number of failed bundles and ionomer chains at any time and the cluster formation and development at (b) 87% of the membrane failure time, (c) 99% of the membrane failure time, and (d) the membrane failure time.

5.2. The calibration of the chemical degradation phase

The model predictions for pure chemical membrane degradation are calibrated using the empirical model developed by [71], which is based on experimental results obtained during AMDTs. These tests primarily focused on chemical membrane degradation but, instead of isolating it from mechanical stress, strategically applied periodic light RH cycles. This approach facilitated a membrane failure mode (pinhole/fracture) that mirrors failures observed during field operations. Simultaneously, it reduced test duration compared to pure chemical AST. The chosen failure mode aligns with the current approach of fracture percolation simulation and its application for combined chemo-mechanical membrane degradation. A 10-cell stack was employed to gather statistically relevant data that can be utilized for lifetime prediction and uncertainty analysis.

The empirical model considers a baseline membrane lifetime obtained from a baseline AMDT. The membrane lifetime under specific operating conditions is then estimated by extrapolating from the measured lifetime in the baseline AMDT to the selected operating conditions. This approach involves applying an acceleration factor (AF) for each stressor, which is determined by comparing the AMDT lifetime at a specific operating condition to the baseline lifetime. The AF represents the ratio of the lifetime at the specific operating condition to the baseline lifetime. After determining the acceleration factors for each stressor, the baseline lifetime is adjusted for the desired operating conditions. This is done by multiplying the baseline lifetime by the corresponding acceleration factors that represent the effects of stressors such as cell voltage, temperature, RH, and PITM. This adjustment accounts for the accelerated degradation caused by these stressors in the specific operating conditions. Therefore, the estimated membrane lifetime at the given operating conditions is calculated as [71]

$$\text{Membrane lifetime} = L_{baseline} AF_v AF_{RH} AF_T AF_{PITM} \tag{5.3}$$

where $L_{baseline}$ is the baseline lifetime. The value of the chemical degradation rate for each ionomer chain is calibrated by comparing it with the results obtained from the empirical model under different cell voltages and temperatures. This calibration is conducted while keeping the RH constant at 100%, which represents the typical operating condition of a fuel cell undergoing pure chemical membrane degradation during a load cycle. The average discrepancy between the calibrated results of the present model and the empirical model was found to be 0.25%. Figure

5.6 displays the results of the present model, including the calculated uncertainty, further demonstrating the accuracy and reliability of the model in estimating the membrane degradation.

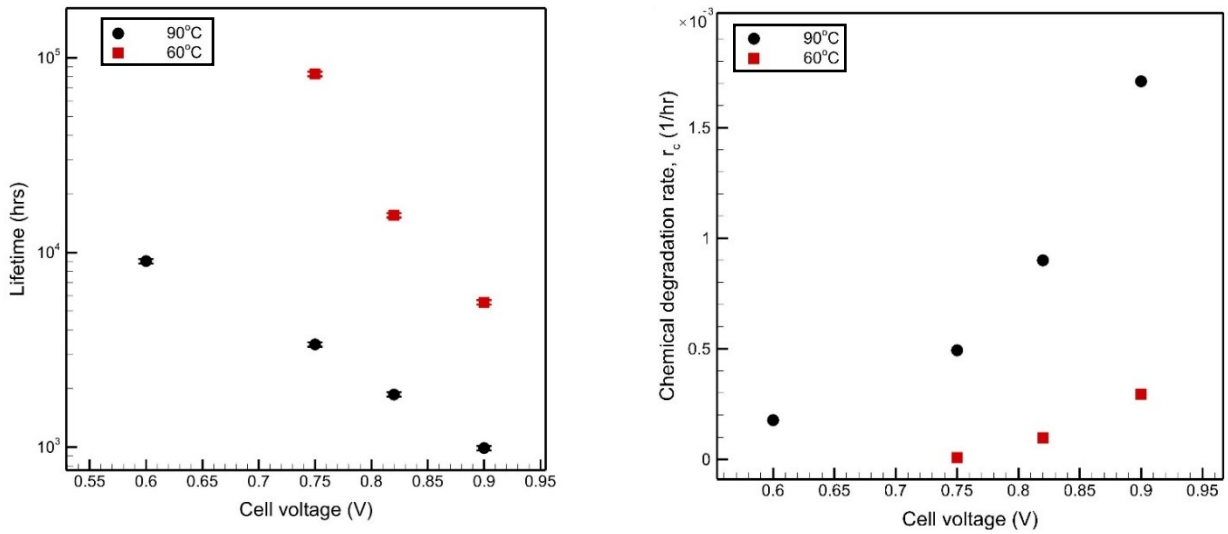

(a) (b)

Figure 5.6: (a) The calibrated results of the present model for pure chemical degradation at RH=100%. (b) The chemical degradation rate for each simulation at RH=100%.

Figure 5.7a illustrates the number of failed ionomer chains and bundles over time for the pure chemical membrane degradation at a cell voltage of 0.9 V and a temperature of 90℃. In contrast to the abrupt bundle failure observed in the pure mechanical degradation, the pure chemical degradation exhibits a more gradual impact on the failure of the bundles. Figure 5.7b-d show the progression of cluster formation at different stages of the simulation for the pure chemical membrane degradation. In this case, without the presence of mechanical stress, the ionomer chains exhibit the same degradation rate and breaking probability at any given time. As a result, clusters are observed throughout the entire domain rather than being concentrated in any specific region, as the degradation affects the domain uniformly.

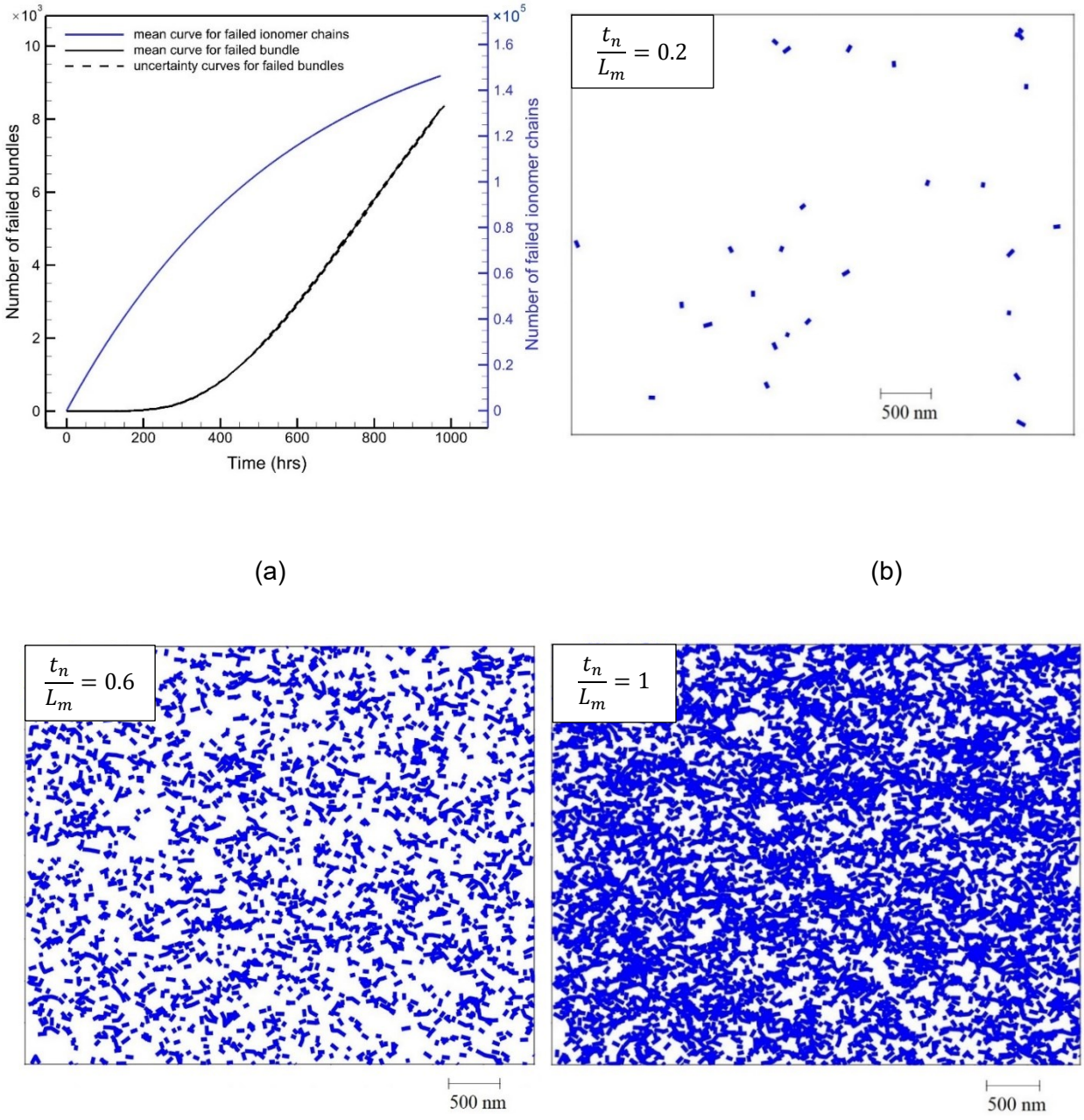

Figure 5.7: The results of the pure chemical degradation at 0.9 V and 90 ℃: (a) the number of failed bundles and ionomer chains at any time and the cluster formation and development at (b) 20% of the membrane failure time, (c) 60% of the membrane failure time, and (d) the membrane failure time.

5.3. Membrane degradation under a combined chemo-mechanical degradation phase

After independent calibrations of membrane degradation model under pure mechanical and chemical degradation modes, the combined chemo-mechanical degradation can be investigated. To this end, an RH cycle is implemented at a constant cell voltage and a constant temperature. The RH cycle and the applied cell voltage bring about a combined chemo-mechanical membrane degradation. Hence, the ΔP-AMST with ΔP=8 kPa at 60℃ is chosen and coupled with a cell voltage of 0.9 V. The results are shown in Figure 5.8. The resulting membrane lifetime is lower than the case under pure mechanical degradation as expected due to the additional chemical degradation. The onset of bundle failure occurs earlier than in the pure mechanical case due to the degradation contribution from the chemical degradation. The chemo-mechanical degradation features a more gradual bundle failure during the simulation time than pure mechanical degradation since the even distribution of chemical degradation rate across all the bundles prevents sudden cluster growth and membrane failure at a specific region after the first bundle breaks, as observed in pure mechanical degradation. This phenomenon also results in a more scattered distribution of broken bundles at the time of membrane failure.

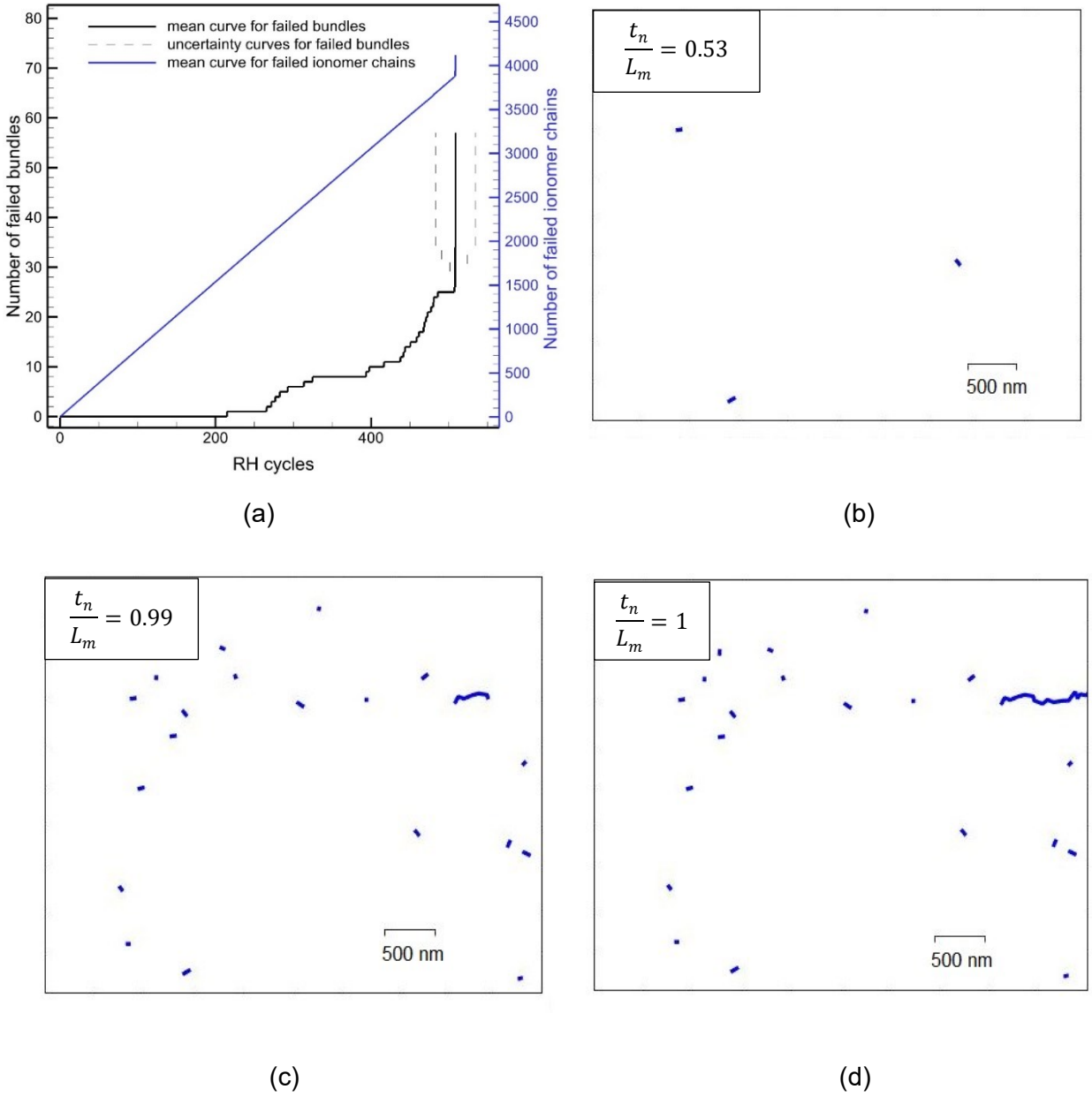

Figure 5.8: The results of the combined chemo-mechanical degradation conducted using ΔP-AMST with ΔP=8 kPa at 60℃ and at 0.9 V: (a) the number of failed bundles and ionomer chains at any time and the cluster formation and development at (b) 53% of the membrane failure time, (c) 99% of the membrane failure time, and (d) the membrane failure time.

5.4. Simulating membrane degradation under a FCEV drive cycle

The calibrated model is utilized to predict the lifetime of a membrane under real-world operating conditions. The vehicle operation is divided into two sections: SU/SD and the load cycles. The SU/SD phase is characterized by rapid changes in temperature and humidity as the fuel cell transitions from ambient conditions to the operating conditions and vice versa. The load cycle refers to the main operational phase during which the fuel cell reaches a stable temperature and humidity, and the vehicle is in active use. To analyze the membrane degradation under a realistic drive cycle, the transit bus drive cycle in the city of Victoria, B.C. presented in section 4.1 with the same polarization curves is again considered. The initial potential cycles are obtained using the initial polarization curves as discussed in section 2.3. Furthermore, the voltage degradation, which was calculated in section 4.1 based on the ECSA drop, is again utilized for membrane degradation to update the potential cycles at any given time. Therefore, the catalyst and membrane degradation models are finally coupled together. The assumptions for the bus operation analysis are outlined below.

1. The temperature and RH are assumed to remain constant throughout the load cycle. Certain variations in RH during the load cycles, resulting from changes in water production and heat generation due to transitions between high and low loads, are neglected. The RH is assumed to be 100% for all load cycle simulations. The RH is set at 100% throughout the load cycle to enhance the performance and lifetime of the membrane as the membrane is known to exhibit better performance and lifetime under higher RH levels.

2. The cell voltage drop over time is determined using the simplified Tafel kinetics approach, following the methodology outlined in section 2.3.

3. No hybridization with a battery system is implemented, and the entire required power for the vehicle operation is solely generated by the fuel cell.

The characteristics of the bus and fuel cell are described in Table 4.2.

For the SU/SD analysis, the model considers the average temperature and RH observed in the city of Victoria as representative of the ambient conditions. The average temperature and

RH in January and August in the city of Victoria are reported as 6℃ and 90% RH, and 18℃ and 73% RH, respectively [120]. They are taken as the typical ambient conditions in winter and summer. The duration of the SU/SD phase can depend on various factors, including the specific fuel cell system design such as sizes of heater and humidifier and operating conditions. In this thesis, different SU/SD durations are considered for each SU and SD: 30 s, 60 s, 90 s, 120 s. Figure 5.9 shows a schematic of the SU/SD and load cycles during real-world operation.

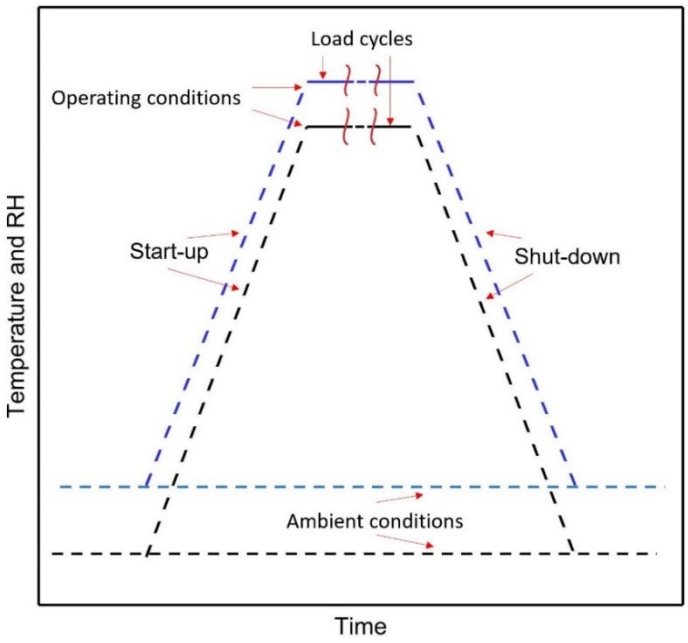

Figure 5.9: A schematic of the SU/SD and load cycles.

The stress distribution across the membrane is determined through finite element simulations and the maximum stress value across the membrane is extracted and utilized as input for the model. These simulations were carried out for realistic fuel cell conditions on the same MEA used for the ΔP-AMSTs when no pressure differential is applied (ΔP=0). A 1.5 MPa clamping pressure was applied to mimic the realistic fuel cell condition. The geometry of the MEA and the flow field plate is assumed according to [61]. The average lifetime of the simulations of different SU/SD durations and different ambient conditions for summer and winter are taken as the predicted lifetime for each case. Moreover, in order to maximize the lifetime of the fuel cell stack and meet the DOE lifetime target, the smallest stack that can meet the power demand is chosen. In Chapter 4, it was determined that smaller stacks tend to have lower UPLs, which can contribute to a longer lifetime by reducing the degradation rate. Figure 5.10 shows the mechanical and chemical degradation rates for a 132-kW stack operating at 90℃. The initial 60 s of this graph represents the start-up

phase, and the subsequent portion indicates the load cycle. The mechanical degradation of the fuel cell membrane is primarily observed during the SU/SD phase, which is characterized by rapid temperature and humidity variations. In contrast, during the load cycle, where the fuel cell operates at steady temperature and humidity conditions, the mechanical degradation was found to be negligible [100]. During the SU/SD phase, the mechanical degradation rates are significantly lower compared to the chemical degradation rates experienced during the load cycle. This can be attributed to the lower temperatures that the fuel cell operates at during the SU/SD phase, which reduces the severity of mechanical stresses on the membrane. The mechanical degradation was observed to be highly dependent on temperature (Figure 5.3), and lower temperatures during SU/SD can result in slower mechanical degradation rates. Additionally, the SU/SD cycles are noticeably shorter than the load cycles; thus, contribution of mechanical degradation to the overall degradation becomes even less important, as is likely the case for heavy duty vehicles. Figure 5.3 shows that severe RH cycles at elevated temperatures result in considerable mechanical degradation. However, the typical SU/SD cycle does not exhibit such extreme conditions. For instance, during a start-up cycle, the fuel cell initially operates at lower temperatures and relatively dry conditions. As the start-up progresses, both the temperature and relative humidity gradually increase.

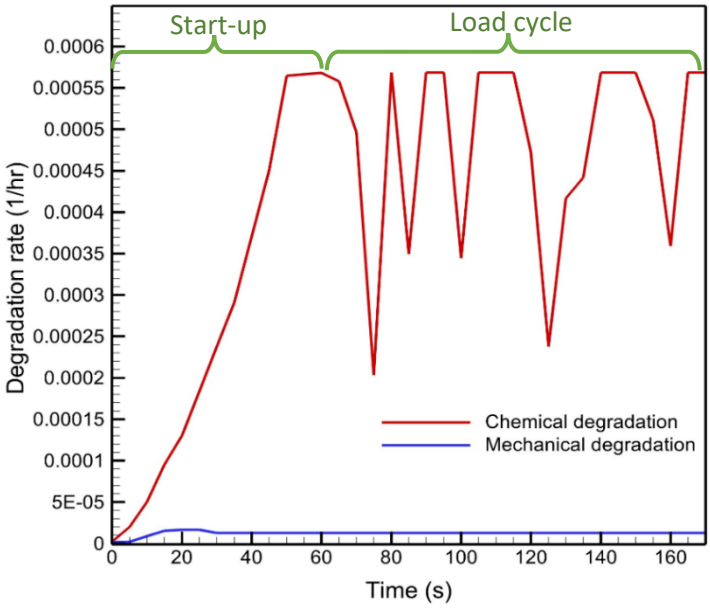

Figure 5.10: The variation of the mechanical and chemical degradation rates with time for a 132-kW stack operating at 90℃ under the transit bus drive cycle.

Figure 5.11a shows the obtained membrane lifetimes for different temperatures with and without considering the effect of voltage loss calculated through catalyst degradation model. Assuming the voltage degradation over time on the membrane lifetime causes the membrane to operate at lower degraded voltages over time, resulting in a longer lifetime compared to the scenario where this effect is neglected. The results show that lower temperatures escalate the effect of voltage loss on lifetime since stacks running at lower temperatures exhibit higher lifetimes which lead to increased voltage loss accumulation over time. This continuous voltage loss over time contributes to even longer lifetimes at lower temperatures. The continuous voltage drop over time due to fuel cell degradation is likely to occur during any vehicle operation under real-world drive cycles and should be included in the fuel cell lifetime predictions. It is also understood that the 132-kW stack can meet the DOE fuel cell bus lifetime target when operating at 70℃ or lower temperatures. Figure 5.11b displays the membrane lifetimes when operating within different stack sizes. As observed in the catalyst degradation analysis, larger stacks inflict greater UPLs, leading to lower membrane lifetimes. Similar to the case of cathode lifetime, the 132-kW stack is found to deliver the highest membrane lifetime.

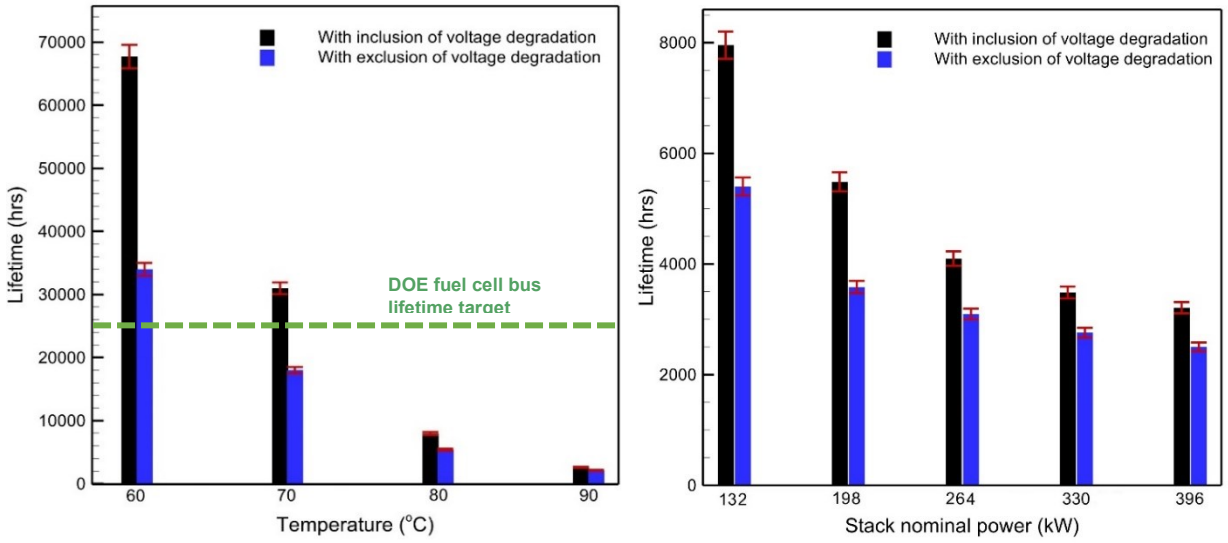

(a) (b)

Figure 5.11: The membrane lifetime under the transit bus operation; (a) for the 132-kW stack at different temperatures; (b) for different stack nominal powers at 80℃.

In this chapter, the developed membrane durability model was separately calibrated using experimental tests for mechanical and chemical degradation. Subsequently, the model was utilized to simulate the membrane lifetime under real-world transit bus operation conditions. It was observed that smaller stacks operating at lower temperatures exhibited greater durability. Furthermore, the voltage degradation resulting from ECSA drop was found to positively impact membrane durability.

Chapter 6: Overall stack lifetime and degradation mitigation strategies

Catalyst and membrane experience different degradation mechanisms and processes which can affect each other's performance and degradation. The cathode catalyst degradation involves phenomena such as platinum particle dissolution and redeposition which result in particle size growth, leading to a reduction in the ECSA. On the other hand, the membrane degradation includes mechanical degradation, chemical degradation, or a combination of both, resulting in fracture, tear, and gas crossover. The catalyst degradation affects the membrane performance and degradation by diffusing and depositing platinum ions into membrane and by cell voltage degradation. Since catalyst degradation and membrane degradation occur through different mechanisms and processes, their lifetimes may vary even when subjected to the same operating conditions. In this chapter, the lifetimes of the catalyst and membrane will first be compared under identical operating conditions to obtain valuable insights into their relative susceptibility to degradation. Then, the overall stack lifetime will be evaluated as a function of operating conditions to determine what factors limit its durability. Finally, strategies will be explored to enhance the stack lifetime through mitigation of lifetime-limiting factors. The findings of this chapter will be crucial in the design and optimization of fuel cell systems, as they help identify where additional attention and mitigation strategies should be focused. Figures 6.1a and 6.1b present the simulated cathode catalyst layer and membrane lifetime change with cell temperature and stack size under the same transit bus drive cycle, respectively. The 132-kW stack is chosen to investigate the effect of temperature on lifetime in Figure 6.1a as it was found to be the most durable stack against membrane and cathode degradation mechanisms. In almost all the cases, the membrane was found to be the more vulnerable component to degradation due to the severe chemical degradation during load cycle. The temperature and stack size affect the membrane and cathode lifetimes to different extents. The variation of temperature was found to affect the membrane lifetime more significantly than the cathode lifetime while change of stack size resulted in more cathode lifetime change.

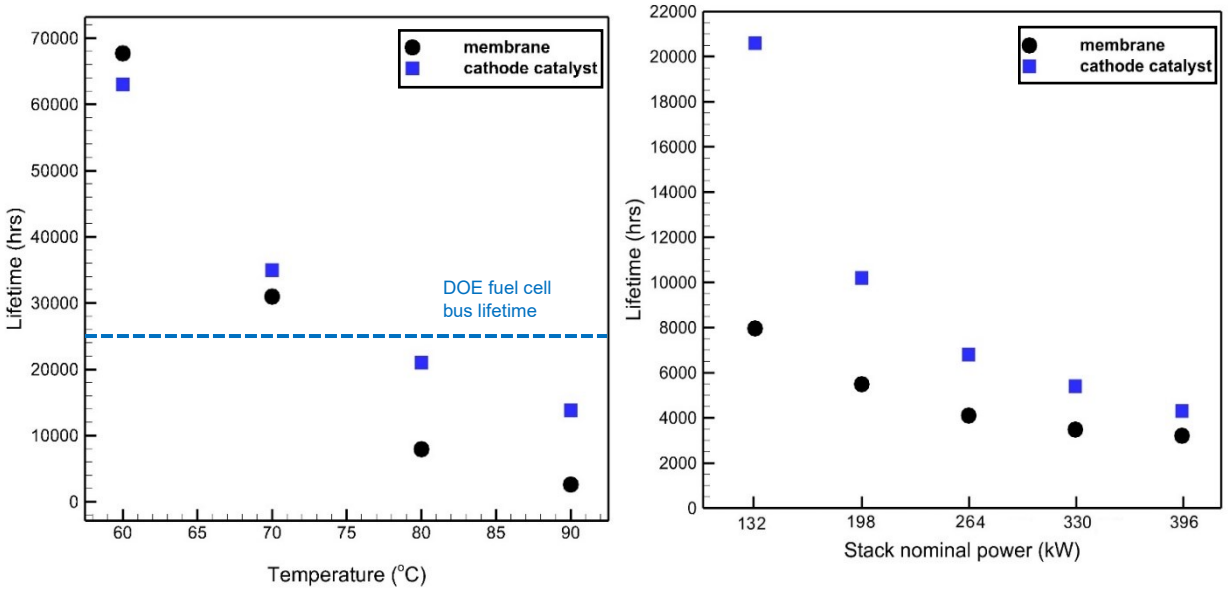

Figure 6.1: Simulated membrane and cathode lifetimes under the transit bus drive cycle (a) at different temperatures in a 132-kW stack; (b) in different stack sizes at 80 ℃.

According to Figure 6.1, the membrane and catalyst within the 132-kW stack operating at 70℃ or lower temperatures were the only cases to be observed to meet the lifetime targets set by the US DOE. The fuel cell components fell short of meeting the lifetime target in other cases. This highlights the need for the development and evaluation of degradation mitigation strategies to ensure long-term performance and durability of the fuel cell system. In this chapter, two degradation mitigation strategies are discussed and evaluated: lowering the cell temperature and using voltage clipping.

6.1. Reducing the cell temperature as a degradation mitigation strategy

Figure 6.1 shows that both catalyst and membrane lifetimes are significantly affected by the temperature. The lifetimes of catalyst and membrane non-linearly increases by decreasing the temperature. However, the dependency of membrane lifetime on temperature is more substantial compared to that of the catalyst. The non-linear increase in lifetimes with decreasing temperature suggests that operating the fuel cell at lower temperatures can lead to improved

durability and extended lifetimes for both the catalyst and membrane due to slower degradation kinetics at lower temperatures. For instance, both membrane and catalyst are found to meet the DOE lifetime requirement when operating at 70℃. However, they fall short of meeting the DOE lifetime target when running at 80℃. These results highlight the importance of temperature control in the fuel cell system. Furthermore, according to Figure 4.6, the fuel cell performance drop due to lowering the temperature from 80℃ to 70℃ is negligible; thus, fuel cell operation at 70℃ appears to be one effective approach to mitigate the degradation and meet the lifetime target. Lowering the cell temperature, however, may lead to a number of drawbacks such as lower efficiency which results in more hydrogen consumption, and a need for more efficient heat dissipation and water management. As the cell temperature decreases, it becomes more crucial to effectively manage and dissipate the excess heat generated during operation. On the other hand, according to Figure 4.6, the marginal performance trade-off at lower temperatures (such as 70°C) suggests that any surplus heat generated and water accumulation may not pose significant challenges and could be effectively managed.

6.2. Voltage clipping by fuel cell hybridization with a battery

In addition to high temperatures, excessive voltage also leads to high levels of degradation for both catalyst and membrane. Voltage clipping involves setting a predefined upper limit, known as the clipping voltage, to prevent the fuel cell from operating at excessively high voltages. By implementing voltage clipping, the system can avoid prolonged exposure to high voltages that can accelerate degradation processes. Setting the clipping voltage is critical in managing the balance between degradation and performance in fuel cell systems. The clipping voltage is chosen to prevent excessive degradation while still maintaining the required performance levels. The voltage and power drawn from the fuel cell stack are interconnected through the polarization curves. As the power drawn from the stack decreases, the voltage typically increases due to the non-linear characteristics of the polarization curve. Therefore, by setting a minimum power limit, the power drawn from the stack is restricted to a certain level, which in turn establishes a maximum voltage limit. The minimum power limit is set above the typical limit imposed by the operating conditions to ensure limiting the maximum voltage. Therefore, the excess power generated by the fuel cell after setting the minimum power limit should be stored in a battery. In addition, a smaller stack can be chosen when the fuel cell is hybridized with a battery since the stored energy in the battery can compensate for the lower power output of a smaller fuel cell stack during periods of high power demand. The maximum power that the smaller stack can provide

after hybridization is called the maximum power limit. The maximum power limit is in fact an indication of the new stack size. Figure 6.2 displays a schematic of how hybridization is applied (p_{max} and p_{min} denote the maximum and minimum power limits, respectively) and Figure 6.3 shows a schematic of a hybrid fuel cell-battery electric bus.

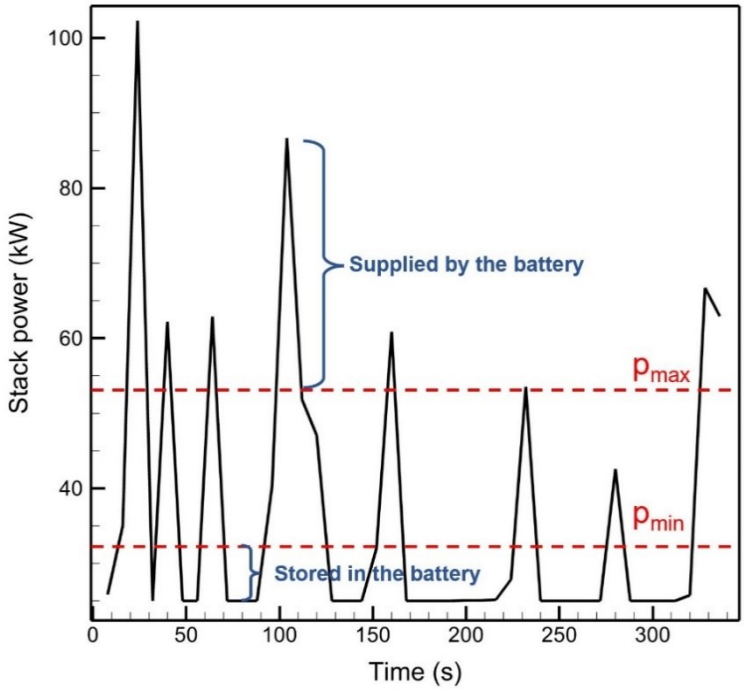

Figure 6.2: A schematic of power management in a hybridized system.

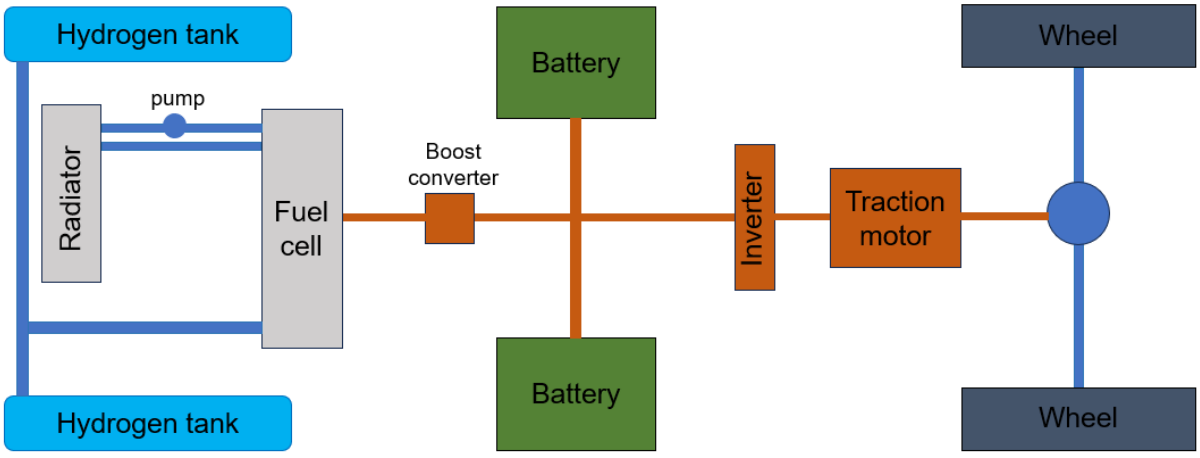

Figure 6.3: A schematic of a hybrid fuel cell-battery electric bus [114].

As mentioned earlier, the hybridization process results in the selection of a smaller fuel cell stack, which offers improved durability and cost-effectiveness. However, the smaller stack operates under different cell conditions to meet power demands efficiently. For example, the cells in a smaller stack tend to operate at lower voltages, higher current densities, and higher power densities compared to the ones in a larger stack to meet the similar power demand. This fact might have some unfavorable consequences for the fuel cell system such as drawing more current density since stacks operating at higher current densities will have lower voltage efficiencies. The higher current density might lead to more hydrogen consumption by the stack. A normalized hydrogen consumption variable is defined as the ratio of hydrogen consumption in any hybridized case to that in a non-hybridized case. Hydrogen consumption is proportional to the current density and stack size, therefore

$$\text{Normalized hydrogen consumption} = \frac{i_{avg,h} \times N_{cell,h} A_{cell,h}}{i_{avg} \times N_{cell} A_{cell}} \tag{6.1}$$

where $N_{cell,h}$, $A_{cell,h}$ are the number of cells and cell area after hybridization, respectively and $i_{avg,h}$ and i_{avg} are the average current densities over a drive cycle after and before the hybridization, respectively.

6.2.1. The optimization of the hybridized system

Hybridization is anticipated to enhance the fuel cell lifetime and reduce the fuel cell cost. Nonetheless, it might lead to an increase in hydrogen consumption which is an unfavorable consequence of hybridization. Since hybridization affects these functions differently, an optimization process is necessary to thoroughly investigate and optimize the overall fuel cell system. To this end, the multi-objective genetic algorithm is utilized where the objective functions are the fuel cell lifetime (which is the least lifetime between the membrane and cathode lifetimes) and the normalized hydrogen consumption. Fuel cell lifetime is implicitly obtained by running the developed cathode and membrane lifetime models during the genetic algorithm implementation. The design variables are the maximum and minimum power limits (p_{max} and p_{min}). The optimization assumptions are summarized as follows.

- the input energy stored in the battery is assumed to be approximately equal to the energy drawn from the battery and supplied to the system within a single drive

cycle. In this way, the battery will be designed to prevent overcharging and it will not fall short when needed.

- The battery degradation is not taken into consideration.
- The cell temperature is kept at 80℃.

Table 6.1 summarizes the defined optimization problem.

Table 6.1: Summary of the optimization of the hybridized system.

Objective functions	Fuel cell lifetime	Hydrogen consumption
Design variables	p_{max}	p_{min}
Condition	$E_{input,\ battery} = E_{output,\ battery}$	

Unlike traditional optimization, which focuses on a single objective function, multi-objective optimization considers multiple objectives simultaneously. These multiple objectives can conflict with each other. The goal is to find a set of solutions known as the Pareto frontier, representing the best trade-offs between the various objectives. These solutions cannot be improved in one objective without sacrificing another. There is no single optimal solution for multi-objective optimization problems. Instead, the goal is to provide the designers with a range of optimal solutions, allowing them to choose the one that best aligns with the design requirements and targets. Figure 6.4 shows the Pareto frontier, and Table 6.2 presents the details of the optimization results including the values of objective functions and corresponding design variables.

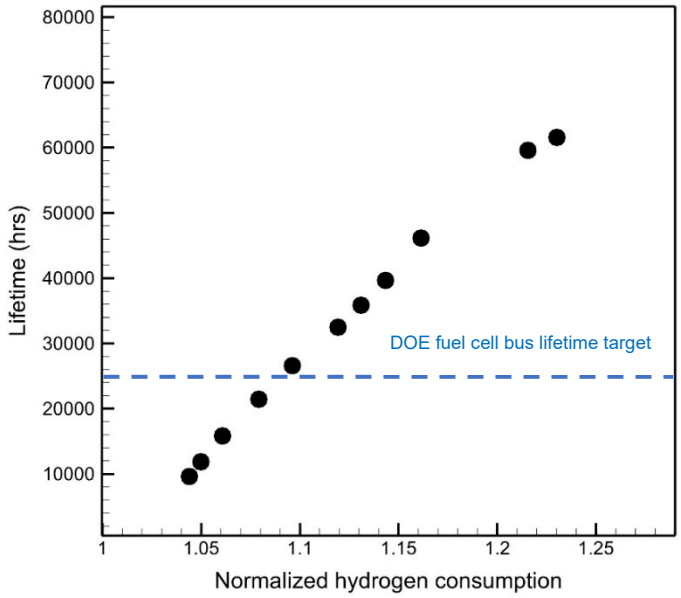

Figure 6.4: The resulting Pareto frontier of the optimization problem.

Table 6.2: The optimization results, values of objective functions, and corresponding design variables at Pareto frontier.

p_{max} (kW)	p_{min} (kW)	Normalized H_2 consumption	Lifetime (hrs)	Stored (or supplied) energy per drive cycle in the battery (kWh)
41.91	39.57	1.23	61600	9.93
42.41	39.39	1.22	59588	9.80
50.00	37.11	1.16	46156	8.18
54.45	35.91	1.14	39661	7.32
56.90	35.31	1.13	35880	6.90
59.11	34.78	1.12	32500	6.53
64.10	33.65	1.096	26605	5.74
70.18	32.52	1.08	21428	4.94
79.30	30.93	1.06	15840	3.84
93.20	29.15	1.05	11878	2.63
107.04	27.67	1.04	9617	1.65
no hybridization	no hybridization	1	7953	0

According to Figure 6.4, a hybridized fuel cell-battery system results in an improved fuel cell lifetime which comes with the expense of an increased hydrogen consumption rate. At a higher hybridization level, the fuel cell lifetime and hydrogen consumption rate increase. In this case, the

choice of hybridization level is dictated by the design requirements. For example, to meet the minimum fuel cell lifetime set by DOE (25,000 hours), the designer should choose specific power limits (p_{max} = 64.10 kW and p_{min} = 33.65 kW) for the fuel cell system. This selection ensures a fuel cell lifetime of 26,605 hours while minimizing the increase in hydrogen consumption rate due to hybridization (a 9.6% increase in hydrogen consumption rate). The hybridized fuel cell also generates extra heat due to lower efficiency. Table 6.2 shows the resulting specifications of each hybrid scenario and quantitatively demonstrates how fuel cell lifetime and hydrogen consumption increase with the level of hybridization. It also presents the stored energy in the battery within a drive cycle. According to the optimization assumption, the same energy is drawn from the battery within the same drive cycle. This energy can be considered as the chosen battery capacity. This way ensures that the selected battery capacity is sufficient to meet the energy demands of that specific hybridization level.

6.3. Model results comparison with the actual fuel cell bus operation

Although the lifetime models have been extensively validated with published experimental results, it is still valuable to compare the model predictions with real-world transit fuel cell bus operations. While there have been significant advancements in fuel cell technology and real-world applications, comprehensive studies examining the long-term performance and degradation of fuel cell buses in actual operational settings are relatively scarce. The high confidentiality surrounding the results and data from real-world fuel cell bus operations can be a significant factor hindering their publication. In many cases, fuel cell bus projects involve partnerships between private companies, government agencies, and research institutions. As a result, the data collected during these projects may be considered proprietary or sensitive due to commercial interests or contractual agreements. The collaboration between DOE and the National Renewable Energy Laboratory (NREL) has led to the publication of a report on the long-term operation of fuel cell transit buses [121]. The report evaluates the degradation of older buses that have been in operation since 2010. Specifically, the analysis focuses on 15 buses from the bus fleet operated by Alameda-Contra Costa Transit District (AC Transit) in Oakland, California. In their study, specific fuel cell system diagnostics were not available which made the process of degradation analysis challenging. However, they used the changes observed in the recorded fuel economy as a substitute or proxy for assessing the performance of the fuel cell system instead of the degraded

voltages. As the voltage decreases over time, the fuel cell's ability to generate power diminishes, potentially affecting the vehicle's ability to complete routes, especially those involving hills or challenging terrains; thus, reducing the fuel cell efficiency. The reduction in efficiency results in more fuel consumption to produce the same amount of power. Therefore, the fuel consumption will increase over time during the operation due to the degradation. The fuel economy records demonstrate that the fuel economy of these transit buses exhibited seasonal fluctuations but experienced a steady decline over time [121]. This reduction in fuel economy is attributed to the degradation of the fuel cell, which affected its efficiency and overall performance. This study shows that, on average, the fuel economy of the buses decreased by 1.3% for every 1,000 hours they were in operation, and the fuel cell buses lost approximately 20% of their initial fuel economy after an average of 17,000 hours of operation. The study revealed notable variations among the buses in terms of fuel economy decay rates and the time it took for a 20% loss in fuel economy. The fuel economy decay rate per 1000 hours exhibited a standard deviation of 0.4%, and the time to a 20% reduction in fuel economy has a standard deviation of 6,500 hours [121].

NREL's report does not provide essential information on decisive parameters such as cell temperature, stack specifications, drive cycle data, etc. that significantly influence fuel cell performance and degradation over time. Therefore, comparing the model results with the estimated lifetime provided by NREL presents specific challenges. In this thesis, the time to a 20% reduction in fuel economy (which is equivalent to the time to a 20% increase in the hydrogen consumption) is calculated for all the cases considering the voltage degradation over time. Voltage degradation results in a decreased output power over time, necessitating operation at higher currents to meet the power demands. Therefore, the fuel cell consumes more fuel over time due to degradation. Figure 6.5a shows the power density change with current density at different stages over time. The change of current density after 15% voltage drop at 0.5 A cm^{-2} while operating at a fixed power density of 0.4 W cm^{-2} is demonstrated as an example. The increase in current density over time during the drive cycle results in a higher consumed hydrogen. Figure 6.5b illustrates the correlation between voltage drop and the fuel consumption rise for a fuel cell bus operation with the drive cycle shown in Figure 4.5. The results suggest that a 20% increase in hydrogen consumption is equivalent to a 12.5% voltage drop.

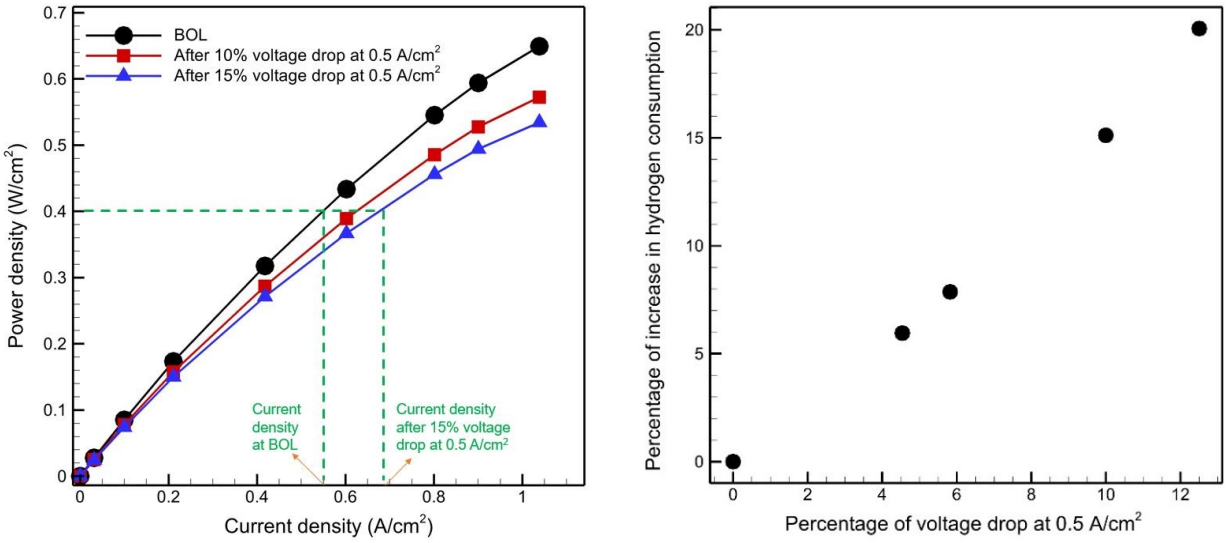

(a) (b)

Figure 6.5: (a) Power density change with current density at different stages over time; (b) hydrogen consumption rise with the voltage drop at 0.5 A cm^{-2}.

Following calculation of the fuel consumption rise over time, the time to a 20% increase in the hydrogen consumption is calculated for a number of cases, and the results are shown in Figure 6.6.

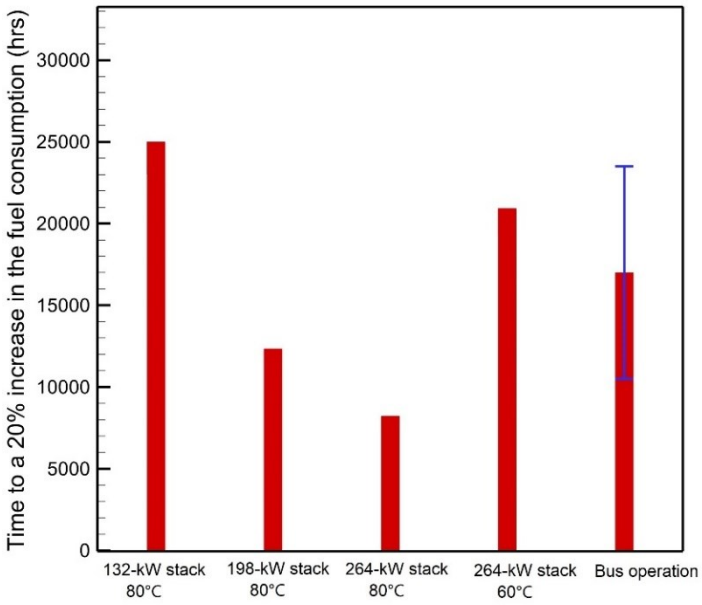

Figure 6.6: The time to a 20% increase in the fuel consumption for different scenarios.

Figure 6.6 reveals that the calculated times for different scenarios are relatively consistent with the range observed in real-world operation. The lack of details in the published results as well as the dependency of lifetime on the operating conditions and stack specifications make a more in-depth comparison challenging.

In this chapter, the membrane and catalyst lifetimes were compared under identical operating conditions. Then, degradation mitigation approaches such as operation at low temperatures and utilization of a fuel cell-battery hybridized system were investigated. A multi-objective genetic algorithm was employed to optimize the hybridized system. While operating at lower temperatures can effectively enhance the fuel cell lifetime, it may reduce fuel cell efficiency, necessitating more robust water management and heat removal strategies. Additionally, it was found that hybridized fuel cell systems can result in a smaller and more durable stack, albeit with higher hydrogen consumption and heat generation.

Chapter 7: Conclusions and recommendations

This thesis focuses on developing fundamental degradation models for PEMFC components (i.e., cathode catalyst and membrane) to predict their lifetimes under various lab conditions and real-world operations. The cathode catalyst and membrane experience different degradation mechanisms, and they fail under different criteria; therefore, their degradation mechanisms should be studied separately to independently develop their modeling procedures. Following the establishment of separate modeling frameworks for the catalyst and membrane degradation mechanisms, possible couplings between the degradation mechanisms of these two components have been integrated into the model.

Cathode catalyst degradation mechanisms primarily include platinum degradation and carbon corrosion. Carbon corrosion results in detachment of the platinum particles and their subsequent reattachment to the existing supported platinum particles. Notably, carbon corrosion was observed to have a significantly slower kinetic rate compared to the platinum degradation under the potentials below OCV. Platinum degradation is a critical factor contributing to the majority of cathode failures in fuel cells and involves the dissolution and redeposition of the platinum particles through electrochemical and chemical degradation mechanisms. The platinum particle size in the catalyst layer exhibits a wide range of variations and is not uniform. As per the Ostwald ripening phenomenon, smaller particles predominantly experience dissolution because of their lower dissolution equilibrium potential, leading to the formation of platinum ions. Subsequently, the generated platinum ions dominantly redeposit on the larger particles, causing an overall increase in the average particle size over time. This phenomenon contributes to the platinum particle growth over time, leading to a reduction in the available active surface area and catalytic performance of the cathode. Furthermore, an oxide coverage layer may form over platinum surface at high potentials as a result of the degradation. In this thesis, the platinum dissolution and redeposition, oxide coverage over the platinum surface and the platinum ion formation were modeled using the well-known Butler-Volmer approach.

A realistic observation of the platinum particle distribution is required to develop a catalyst degradation model. Therefore, two samples of the catalyst were taken for electron microscopy to study the structure of the platinum distribution. The first sample was a pristine catalyst processed after the catalyst ink preparation. The TEM images taken from the pristine sample revealed the platinum PSD observed from the carbon supported platinum particles. The second sample was related to a degraded sample that had undergone 25,000 AST cycles. The degraded sample

indicated non-uniform platinum PSDs at different regions across the catalyst. The analysis of the catalyst region near the membrane interface showed a lower platinum concentration compared to the middle of the catalyst. This observation is attributed to the migration and diffusion of platinum ions generated in proximity to the membrane interface. These platinum ions may move toward the membrane under the influence of electric fields and diffuse into the membrane, resulting in a decrease in the platinum concentration in that region.

Although the TEM and SEM images demonstrated the platinum ion movement within the catalyst and their deposition into the membrane, the results of the developed 0-D model agree well with the published results in the literature. Moreover, several studies in the literature have successfully utilized 0-D model which further justifies the usage of 0-D model in this thesis. To ensure the reliability of the model, the reaction rate constants were successfully calibrated using published degradation results from a range of AST cycles with varying UPLs, LPLs, and temperatures. The reaction rate constants were adjusted by comparing ECSA resulted from the model and the published results in the literature.

The calibrated catalyst degradation model was employed to simulate the platinum degradation under a real-world transit bus operation in the city of Victoria, B.C., Canada. The fuel cell bus recorded drive cycle was converted into the voltage profile using a typical polarization curve and stack specifications. The catalyst degradation was coupled with the performance degradation by calculating the voltage drop using simple Tafel kinetics and updating the polarization curve throughout the simulation. As the voltage decreases over time, the degradation process tends to slow down compared to the initial stages of the simulation. In addition, the effects of stack size and cell temperature were investigated on the catalyst degradation and lifetime. The estimation of cathode lifetimes was carried out by considering a 10% voltage drop at 0.5 A cm^{-2}. The investigation revealed that larger stacks tend to operate at higher voltages, resulting in higher catalyst degradation rates. Increasing the stack size from 132 to 396 kW at 80℃ led to a significant 79% reduction in the cathode lifetime under the transit bus drive cycle. Temperature was also identified as a major factor affecting cathode degradation, with higher temperatures leading to a substantial decline in cathode lifetime. Raising the temperature from 60 to 80℃ for a stack with a nominal power of 264 kW under transit bus operation resulted in a 61% reduction in cathode lifetime due to more pronounced platinum degradation rates at higher temperatures. Throughout the degradation simulations of different stacks at varying temperatures, electrochemical platinum dissolution emerged as the primary degradation mechanism, consistently contributing to over 99% of the overall degradation rate. These findings highlight the importance of stack size and

temperature considerations in assessing and predicting fuel cell cathode lifetimes, providing crucial insights for optimizing fuel cell system performance and durability. To enhance the cathode lifetime, it is recommended to explore smaller stacks operating at lower temperatures, provided that they meet the required power demand. Among the investigated scenarios, the smallest stack (132 kW) operating at lower temperatures (60 or 70℃) was observed to fulfill the US DOE's 25,000-hour fuel cell transit bus lifetime target for cathode catalyst durability. However, this approach may result in a reduced maximum power output from the fuel cell stack, potentially impacting vehicle acceleration and overall power performance. Despite this trade-off, opting for a smaller stack could yield benefits in terms of lower capital costs, ultimately improving the system's overall economic viability.

The membrane degradation is predominantly affected by mechanical and chemical degradation mechanisms. The mechanical membrane degradation occurs due to cyclic mechanical stresses caused by continuous variation in RH and temperatures while the chemical membrane degradation is a result of radical attack on the membrane at high potentials. In this thesis, a statistical model for membrane degradation was developed based on the fibrillar morphology of the membrane. The membrane was assumed to be composed of a network of connected bundles, with each bundle containing a certain number of ionomer chains. Then, the overall breaking probability of each ionomer chain was determined by separately considering mechanical and chemical degradation rates. Mechanical degradation rate was defined as the inverse of the thermally activated breaking time of a C-C bond in ionomer chains while the chemical degradation rate was taken to be a parameter which is a function of voltage, temperature, and RH. A bundle is deemed to have failed when all its ionomer chains have experienced failure. The stress is redistributed non-uniformly following the failure of a bundle, leading to increased stress on the adjacent bundles. The clusters of connected failed bundles represent microcrack within the membrane. The membrane is assumed to have failed when the longest path along the clusters exceeds a critical threshold value. The model is first successfully calibrated with the empirical results obtained from the fuel cell degradation tests under pure mechanical and chemical degradation mechanisms. The results of ΔP-AMSTs on a mechanically reinforced membrane were used to study the impact of applied pressure differential and temperature on pure mechanical membrane degradation. These tests covered a wide range of stresses and temperatures, providing valuable data for calibrating the model using the genetic optimization algorithm. The chemical degradation mode of the model is accurately calibrated using the AMDT results obtained for a wide range of temperatures and cell voltages. The results

showed that the chemical membrane degradation is significantly influenced by the cell voltage and temperature. The fully calibrated membrane degradation model was then utilized to simulate the membrane degradation under the real-world transit bus operation. The first finding of membrane degradation analysis under the bus drive cycle is that under pure mechanical degradation, crack propagation occurs noticeably rapidly after the formation of cracks, leading to membrane failure shortly after the onset of cracking. This behavior is attributed to the stress concentration around the failed bundle across the membrane. The bundles adjacent to the failed ones experience higher stress levels compared to the farther bundles, leading to rapid crack propagation and subsequent membrane failure. On the other hand, pure chemical membrane degradation follows a more gradual trend over time due to the absence of mechanical degradation. Combined chemo-mechanical membrane degradation yields the shortest lifetime compared to pure mechanical and chemical degradation cases when implemented separately. The even distribution of chemical degradation rates across all bundles prevents abrupt cluster growth and membrane failure at a specific region after the breaking of first bundle. Therefore, it leads to a more gradual and scattered bundle failure pattern over time compared to the pure mechanical degradation case. Following the full calibration of the membrane degradation model, the transit bus drive cycle was employed to assess the membrane durability under real-world operating conditions. The membrane degradation model was coupled with the catalyst degradation model to account for the voltage drop over time due to the cathode degradation. During the transit bus load cycle operation, no mechanical membrane degradation is observed because the temperature and RH are maintained constant. The only degradation affecting the membrane during the load cycles is the chemical degradation caused by the applied cell voltages. Mechanical degradation solely occurs during SUSD cycles due to variations of temperature and RH. However, the results show that the rapid RH variation during low temperatures at SUSD leads to minimal mechanical degradation rates during SUSD compared to the chemical degradation rates during the load cycles. Cell temperature was identified as a critical factor affecting the membrane lifetime. Lowering the cell temperature from 90 to 70℃ resulted in a nearly 11-time increase in membrane lifetime under the transit bus drive cycle. Notably, the 132-kW fuel cell stack operating at 70℃ or below appears to meet the DOE 25,000-hour lifetime target for fuel cell buses. The inclusion of voltage drop over time due to cathode degradation resulted in higher lifetimes, especially at lower temperatures. Therefore, voltage degradation during operation was observed to be a significant phenomenon affecting the fuel cell lifetime which is expected to occur during any real-world vehicle operation and should be considered in the fuel cell lifetime prediction analyses. As observed in the cathode catalyst lifetime, smaller stacks contribute to a longer

membrane lifetime by yielding lower UPLs. However, the utilization of smaller stacks comes at the expense of higher hydrogen consumption to meet the same power demand.

The analysis of transit bus degradation using various stack sizes and temperatures showed that the DOE lifetime target was not achieved in the majority of scenarios. Consequently, two degradation mitigation strategies were proposed: reducing the cell temperature and implementing fuel cell-battery hybridization. Lowering the temperature proved to be an effective approach, as a 132 kW-stack operating at 70℃ met the DOE lifetime target. Moreover, integrating a battery as part of the hybrid system led to a smaller stack size, which was anticipated to enhance the fuel cell lifetime, albeit with a higher hydrogen consumption. To address this trade-off, minimum and maximum power limits were established, and a multi-objective optimization was implemented using the genetic algorithm. The results indicated that hybridization proved to be a viable approach to enhance the fuel cell lifetime, successfully meeting the DOE lifetime target.

Finally, the findings from this thesis were validated by comparing them with actual fuel cell bus operation data. Despite the lack of specific details on bus operating conditions, such as cell temperature, the estimated fuel cell lifetimes demonstrated a satisfactory agreement with the realistic bus operation results. This successful validation supports the reliability of the developed models.

The findings of this thesis recommend that operating fuel cell transit buses at lower temperatures, without compromising the performance, is a promising strategy to meet the lifetime targets. Additionally, hybridization was identified as a viable approach to enhance fuel cell lifetime although it comes at the expense of increased fuel consumption and added complexity with a battery system. Ultimately, the designers must carefully evaluate these trade-offs and make a well-informed decision on which scenario to choose based on their specific requirements and priorities associated with their applications.

For future work, studying the impact of hold times on catalyst degradation within an AST cycle could provide more valuable insights into the concurrent interaction of platinum degradation and oxide formation. Additionally, investigating the performance and degradation of batteries within a fuel cell-battery hybridized system is crucial to comprehend their effects on fuel cell design and overall system efficiency. Furthermore, to address the trade-offs between the fuel cell system cost, durability, and the operating cost (including fuel consumption), an analysis of vehicle lifecycle cost is proposed.

References

[1] A. Chrisafis and A. Vaughan, "France to ban sales of petrol and diesel cars by 2040," *The Guardian,* vol. 6, no. 7, 2017.

[2] S. Swinford, "Diesel and petrol car ban: Plan for 2040 unravels as 10 new power stations needed to cope with electric revolution," *The Telegraph,* vol. 27, pp. 675-690, 2017.

[3] C. Bonnet, S. Didierjean, N. Guillet, S. Besse, T. Colinart and P. Carré, "Design of an 80 kWe PEM fuel cell system: Scale up effect investigation," *Journal of Power Sources,* vol. 182, no. 2, pp. 441-448, 2008.

[4] F. Wang, D. Yang, B. Li, H. Zhang, C. Hao, F. Chang and J. Ma, "Investigation of the recoverable degradation of PEM fuel cell operated under drive cycle and different humidities," *International journal of hydrogen energy,* vol. 39, no. 26, pp. 14441-14447, 2014.

[5] U. DOE, *3.4 Fuel Cells, FUEL CELL Technol. off,* MULTI-YEAR Res. Dev. Demonstr. PLAN, 2016, pp. 1-58.

[6] P. Urchaga, T. Kadyk, S. G. Rinaldo, A. O. Pistono, J. Hu, W. Lee, C. Richards, M. H. Eikerling and C. A. Rice, "Catalyst degradation in fuel cell electrodes: accelerated stress tests and model-based analysis," *Electrochimica Acta,* vol. 176, pp. 1500-1510, 2015.

[7] M. Kang, J. Sim and K. Min, "Analysis of performance degradation on the components in polymer electrolyte membrane fuel cell by dissecting the oxygen diffusion region," *Journal of Power Sources,* vol. 552, p. 232236, 2022.

[8] L. Fan, J. Zhao, X. Luo and Z. Tu, "Comparison of the performance and degradation mechanism of PEMFC with Pt/C and Pt black catalyst," *International Journal of Hydrogen Energy,* vol. 47, no. 8, pp. 5418-5428, 2022.

[9] Z.-B. Wang, P.-J. Zuo, X.-P. Wang, J. Lou, B.-Q. Yang and G.-P. Yin, "Studies of performance decay of Pt/C catalysts with working time of proton exchange membrane fuel cell," *Journal of Power Sources,* vol. 184, no. 1, pp. 245-250, 2008.

[10] E. M. Koltsova, V. A. Vasilenko, A. I. Shcherbakov, E. A. Fokina and V. A. Bogdanovskaya, "Mathematical simulation of PEMFC platinum cathode degradation accounting catalyst's nanoparticles growth," *Chemical Engineering Transactions,* vol. 70, pp. 1303-1308, 2018.

[11] S. Zhang, X.-Z. Yuan, J. N. C. Hin, H. Wang, K. A. Friedrich and M. Schulze, "A review of platinum-based catalyst layer degradation in proton exchange membrane fuel cells," *Journal of Power Sources,* vol. 194, no. 2, pp. 588-600, 2009.

[12] X. Wang, W. Li, Z. Chen, M. Waje and Y. Yan, "Durability investigation of carbon nanotube as catalyst support for proton exchange membrane fuel cell," *Journal of Power Sources,* vol. 158, no. 1, pp. 154--159, 2006.

[13] S. G. Rinaldo, W. Lee, J. Stumper and M. Eikerling, "Catalyst degradation: nanoparticle population dynamics and kinetic processes," *ECS Transactions,* vol. 50, no. 2, p. 1505, 2013.

[14] M. Inaba, T. Kinumoto, M. Kiriake, R. Umebayashi, A. Tasaka and Z. Ogumi, "Gas crossover and membrane degradation in polymer electrolyte fuel cells," *Electrochimica Acta,* vol. 51, no. 26, pp. 5746-5753, 2006.

[15] M. Messing, "Empirical modeling of fuel cell durability: Cathode catalyst layer degradation," *Simon Fraser University,* 2017.

[16] H. A. Baroody and E. Kjeang, "Predicting Platinum Dissolution and Performance Degradation under Drive Cycle Operation of Polymer Electrolyte Fuel Cells," *Journal of The Electrochemical Society,* vol. 168, no. 4, p. 044524, 2021.

[17] R. O'hayre, S.-W. Cha, W. Colella and F. B. Prinz, Fuel cell fundamentals, John Wiley \& Sons, 2016.

[18] L. Cindrella, A. M. Kannan, J. Lin, K. Saminathan, Y. Ho, C. Lin and J. Wertz, "Gas diffusion layer for proton exchange membrane fuel cells—A review," *Journal of Power Sources,* vol. 194, no. 1, pp. 146-160, 2009.

[19] S. Park, J.-W. Lee and B. N. Popov, "A review of gas diffusion layer in PEM fuel cells: Materials and designs," *International Journal of Hydrogen Energy,* vol. 37, no. 7, pp. 5850-5865, 2012.

[20] E. Middelman, W. Kout, B. Vogelaar, J. Lenssen and E. De Waal, "Bipolar plates for PEM fuel cells," *Journal of Power Sources,* vol. 118, no. 1-2, pp. 44-46, 2003.

[21] A. Hermann, T. Chaudhuri and P. Spagnol, "Bipolar plates for PEM fuel cells: A review," *International journal of hydrogen Energy,* vol. 30, no. 12, pp. 1297-1302, 2005.

[22] M. Messing and E. Kjeang, "Empirical modeling of cathode electrode durability in polymer electrolyte fuel cells," *Journal of Power Sources,* vol. 451, p. 227750, 2020.

[23] J. Stoll, F. P. Orfino, M. Dutta and E. Kjeang, "Four-Dimensional identical-location X-ray imaging of fuel cell degradation during start-up/shut-down cycling," *Journal of The Electrochemical Society,* vol. 168, no. 2, p. 024516, 2021.

[24] A. Pokhrel, E. Kjeang, M. Dutta, F. Orfino and M. El Hannach, "3D Failure Analysis of PEM Fuel Cell Catalyst Layers Using Multi-Length Scale X-Ray Computed Tomography," in *Electrochemical Society Meeting Abstracts 228*, 2015.

[25] R. T. White, A. Wu, M. Najm, F. P. Orfino, M. Dutta and E. Kjeang, "4D in situ visualization of electrode morphology changes during accelerated degradation in fuel

cells by X-ray computed tomography," *Journal of Power Sources,* vol. 350, pp. 94-102, 2017.

[26] J. Li, P. He, K. Wang, M. Davis and S. Ye, "Characterization of catalyst layer structural changes in PEMFC as a function of durability testing," *ECS transactions,* vol. 3, no. 1, p. 743, 2006.

[27] L. Kim, C. G. Chung, Y. W. Sung and J. S. Chung, "Dissolution and migration of platinum after long-term operation of a polymer electrolyte fuel cell under various conditions," *Journal of Power Sources,* vol. 183, no. 2, pp. 524-532, 2008.

[28] M. Darab, A. O. Barnett, G. Lindbergh, M. S. Thomassen and S. Sunde, "The influence of catalyst layer thickness on the performance and degradation of PEM fuel cell cathodes with constant catalyst loading," *Electrochimica Acta,* vol. 232, pp. 505-516, 2017.

[29] A. Kneer, N. Wagner, C. Sadeler, A.-C. Scherzer and D. Gerteisen, "Effect of dwell time and scan rate during voltage cycling on catalyst degradation in PEM fuel cells," *Journal of The Electrochemical Society,* vol. 165, no. 10, p. F805, 2018.

[30] A. Kneer, J. Jankovic, D. Susac, A. Putz, N. Wagner, M. Sabharwal and M. Secanell, "Correlation of changes in electrochemical and structural parameters due to voltage cycling induced degradation in PEM fuel cells," *Journal of The Electrochemical Society,* vol. 165, no. 6, p. F3241, 2018.

[31] H. Yoshida, T. Kinumoto, Y. Iriyama, Y. Uchimoto and Z. Ogumi, "XAS study for degradation mechanism of Pt/C catalyst during potential cycling test," *ECS Transactions,* vol. 11, no. 1, p. 1321, 2007.

[32] D. Bernhard, T. Kadyk, U. Krewer and S. Kirsch, "How platinum oxide affects the degradation analysis of PEM fuel cell cathodes," *International Journal of Hydrogen Energy,* vol. 46, no. 26, pp. 13791-13805, 2021.

[33] K. Khedekar, M. Rezaei Talarposhti, M. M. Besli, S. Kuppan, A. Perego, Y. Chen, M. Metzger, S. Stewart, P. Atanassov, N. Tamura and others, "Probing Heterogeneous Degradation of Catalyst in PEM Fuel Cells under Realistic Automotive Conditions with Multi-Modal Techniques," *Advanced Energy Materials,* vol. 11, no. 35, p. 2101794, 2021.

[34] R. Lin, B. Li, Y. Hou and J. Ma, "Investigation of dynamic driving cycle effect on performance degradation and micro-structure change of PEM fuel cell," *International Journal of Hydrogen Energy,* vol. 34, no. 5, pp. 2369-2376, 2009.

[35] M. Mayur, S. Strahl, A. Husar and W. G. Bessler, "A multi-timescale modeling methodology for PEMFC performance and durability in a virtual fuel cell car," *International Journal of Hydrogen Energy,* vol. 40, no. 46, pp. 16466-16476, 2015.

[36] M. Mayur, M. Gerard, P. Schott and W. G. Bessler, "Lifetime prediction of a polymer electrolyte membrane fuel cell under automotive load cycling using a physically-based catalyst degradation model," *Energies,* vol. 11, no. 8, p. 2054, 2018.

[37] R. M. Darling and J. P. Meyers, "Kinetic model of platinum dissolution in PEMFCs," *Journal of the Electrochemical Society,* vol. 150, no. 11, p. A1523, 2003.

[38] Y. Ao, S. Laghrouche, D. Depernet and K. Chen, "Lifetime prediction for proton exchange membrane fuel cell under real driving cycles based on platinum particle dissolve model," *International Journal of Hydrogen Energy,* vol. 45, no. 56, pp. 32388-32401, 2020.

[39] F. Hiraoka, Y. Kohno, K. Matsuzawa and S. Mitsushima, "A simulation study of Pt particle degradation during potential cycling using a dissolution/deposition model," *Electrocatalysis,* vol. 6, no. 1, pp. 102--108, 2015.

[40] T. Takeshita, H. Murata, T. Hatanaka and Y. Morimoto, "Analysis of Pt catalyst degradation of a PEFC cathode by TEM observation and macro model simulation," *ECS Transactions,* vol. 16, no. 2, p. 367, 2008.

[41] W. Bi and T. F. Fuller, "Modeling of PEM fuel cell Pt/C catalyst degradation," *Journal of Power Sources,* vol. 178, no. 1, pp. 188-196, 2008.

[42] E. F. Holby and D. Morgan, "Application of Pt nanoparticle dissolution and oxidation modeling to understanding degradation in PEM fuel cells," *Journal of The Electrochemical Society,* vol. 159, no. 5, p. B578, 2012.

[43] Y. Li, K. Moriyama, W. Gu, S. Arisetty and C. Wang, "A one-dimensional Pt degradation model for polymer electrolyte fuel cells," *Journal of The Electrochemical Society,* vol. 162, no. 8, p. F834, 2015.

[44] A. Baricci, M. Bonanomi, H. Yu, L. Guetaz, R. Maric and A. Casalegno, "Modelling analysis of low platinum polymer fuel cell degradation under voltage cycling: Gradient catalyst layers with improved durability," *Journal of Power Sources,* vol. 405, pp. 89-100, 2018.

[45] V. A. Kovtunenko and L. Karpenko-Jereb, "Study of voltage cycling conditions on Pt oxidation and dissolution in polymer electrolyte fuel cells," *Journal of Power Sources,* vol. 493, p. 229693, 2021.

[46] W. Zheng, L. Xu, Z. Hu, Y. Zhao, J. Li and M. Ouyang, "Dynamic modeling of Pt degradation and mitigation strategies in polymer electrolyte membrane fuel cells," *eTransportation,* vol. 12, p. 100171, 2022.

[47] N. Macauley, D. D. Papadias, J. Fairweather, D. Spernjak, D. Langlois, R. Ahluwalia, K. L. More, R. Mukundan and R. L. Borup, "Carbon corrosion in PEM fuel cells and the development of accelerated stress tests," *Journal of The Electrochemical Society,* vol. 165, no. 6, pp. F3148--F3160, 2018.

[48] E. Antolini, "Formation, microstructural characteristics and stability of carbon supported platinum catalysts for low temperature fuel cells," *Journal of materials science,* vol. 38, no. 14, pp. 2995--3005, 2003.

[49] H. Tang, Z. Qi, M. Ramani and J. F. Elter, "PEM fuel cell cathode carbon corrosion due to the formation of air/fuel boundary at the anode," *Journal of Power Sources,* vol. 158, no. 2, pp. 1306--1312, 2006.

[50] K. H. Kangasniemi, D. Condit and T. Jarvi, "Characterization of vulcan electrochemically oxidized under simulated PEM fuel cell conditions," *Journal of The Electrochemical Society,* vol. 151, no. 4, p. E125, 2004.

[51] Y. Singh, F. P. Orfino, M. Dutta and E. Kjeang, "3D failure analysis of pure mechanical and pure chemical degradation in fuel cell membranes," *Journal of The Electrochemical Society,* vol. 164, no. 13, p. F1331, 2017.

[52] A. Kusoglu, A. M. Karlsson, M. H. Santare, S. Cleghorn and W. B. Johnson, "Mechanical response of fuel cell membranes subjected to a hygro-thermal cycle," *Journal of power sources,* vol. 161, no. 2, pp. 987-996, 2006.

[53] U. Beuscher, S. J. Cleghorn and W. B. Johnson, "Challenges for PEM fuel cell membranes," *International Journal of Energy Research,* vol. 29, no. 12, pp. 1103-1112, 2005.

[54] R. M. Khorasany, M.-A. Goulet, A. S. Alavijeh, E. Kjeang, G. G. Wang and R. Rajapakse, "On the constitutive relations for catalyst coated membrane applied to in-situ fuel cell modeling," *Journal of Power Sources,* vol. 252, pp. 176-188, 2014.

[55] H. Tang, S. Peikang, F. Wang and M. Pan, "A degradation study of Nafion proton exchange membrane of PEM fuel cells," *Journal of Power Sources,* vol. 170, no. 1, pp. 85-92, 2007.

[56] X. Huang, R. Solasi, Y. Zou, M. Feshler, K. Reifsnider, D. Condit, S. Burlatsky and T. Madden, "Mechanical endurance of polymer electrolyte membrane and PEM fuel cell durability," *Journal of Polymer Science Part B: Polymer Physics,* vol. 44, no. 16, pp. 2346-2357, 2006.

[57] Y. Tang, M. H. Santare, A. M. Karlsson, S. Cleghorn and W. B. Johnson, "Stresses in proton exchange membranes due to hygro-thermal loading," pp. 119-124, 2006.

[58] A. Kusoglu, A. M. Karlsson, M. H. Santare, S. Cleghorn and W. B. Johnson, "Mechanical behavior of fuel cell membranes under humidity cycles and effect of swelling anisotropy on the fatigue stresses," *Journal of Power Sources,* vol. 172, no. 2, pp. 345-358, 2007.

[59] M. N. Silberstein, P. V. Pillai and M. C. Boyce, "Biaxial elastic–viscoplastic behavior of Nafion membranes," *Polymer,* vol. 52, no. 2, pp. 529-539, 2011.

[60] R. M. Khorasany, E. Kjeang, G. Wang and R. Rajapakse, "Simulation of ionomer membrane fatigue under mechanical and hygrothermal loading conditions," *Journal of Power Sources,* vol. 279, pp. 55-63, 2015.

[61] R. Khorasany, Y. Singh, A. S. Alavijeh, R. Rajapakse and E. Kjeang, "In-situ simulation of membrane fatigue in polymer electrolyte fuel cells," *International Journal of Hydrogen Energy,* vol. 42, no. 16, pp. 11838-11844, 2017.

[62] R. M. Khorasany, A. S. Alavijeh, E. Kjeang, G. Wang and R. Rajapakse, "Mechanical degradation of fuel cell membranes under fatigue fracture tests," *Journal of Power Sources,* vol. 274, pp. 1208-1216, 2015.

[63] A. S. Alavijeh, S. Bhattacharya, O. Thomas, C. Chuy and E. Kjeang, "A rapid mechanical durability test for reinforced fuel cell membranes," *Journal of Power Sources Advances,* vol. 2, p. 100010, 2020.

[64] M. W. Verbrugge, R. F. Hill and E. W. Schneider, "Composite membranes for fuel-cell applications," *AIChE journal,* vol. 38, no. 1, pp. 93-100, 1992.

[65] D. Ramani, Y. Singh, R. T. White, M. Wegener, F. P. Orfino, M. Dutta and E. Kjeang, "4D in situ visualization of mechanical degradation evolution in reinforced fuel cell membranes," *International Journal of Hydrogen Energy,* vol. 45, no. 16, pp. 10089-10103, 2020.

[66] A. S. Alavijeh, R. M. Khorasany, Z. Nunn, A. Habisch, M. Lauritzen, E. Rogers, G. G. Wang and E. Kjeang, "Microstructural and mechanical characterization of catalyst coated membranes subjected to in situ hygrothermal fatigue," *Journal of The Electrochemical Society,* vol. 162, no. 14, p. F1461, 2015.

[67] V. A. Sethuraman, J. W. Weidner, A. T. Haug, S. Motupally and L. V. Protsailo, "Hydrogen peroxide formation rates in a PEMFC anode and cathode: Effect of humidity and temperature," *Journal of The Electrochemical Society,* vol. 155, no. 1, p. B50, 2007.

[68] L. Ghassemzadeh, K.-D. Kreuer, J. Maier and K. Müller, "Chemical degradation of Nafion membranes under mimic fuel cell conditions as investigated by solid-state NMR spectroscopy," *The Journal of Physical Chemistry C,* vol. 114, no. 34, pp. 14635-14645, 2010.

[69] V. O. Mittal, H. R. Kunz and J. M. Fenton, "Membrane degradation mechanisms in PEMFCs," *Journal of The Electrochemical Society,* vol. 154, no. 7, p. B652, 2007.

[70] J. Healy, C. Hayden, T. Xie, K. Olson, R. Waldo, M. Brundage, H. Gasteiger and J. Abbott, "Aspects of the chemical degradation of PFSA ionomers used in PEM fuel cells," *Fuel cells,* vol. 5, no. 2, pp. 302-308, 2005.

[71] N. Macauley, M. Watson, M. Lauritzen, S. Knights, G. G. Wang and E. Kjeang, "Empirical membrane lifetime model for heavy duty fuel cell systems," *Journal of Power Sources,* vol. 336, pp. 240-250, 2016.

[72] S. Kundu, M. W. Fowler, L. C. Simon, R. Abouatallah and N. Beydokhti, "Degradation analysis and modeling of reinforced catalyst coated membranes operated under OCV conditions," *Journal of Power Sources,* vol. 183, no. 2, pp. 619-628, 2008.

[73] A. Shah, T. Ralph and F. Walsh, "Modeling and simulation of the degradation of perfluorinated ion-exchange membranes in PEM fuel cells," *Journal of The Electrochemical Society,* vol. 156, no. 4, p. B465, 2009.

[74] K. H. Wong and E. Kjeang, "Macroscopic in-situ modeling of chemical membrane degradation in polymer electrolyte fuel cells," *Journal of the Electrochemical Society,* vol. 161, no. 9, p. F823, 2014.

[75] K. H. Wong and E. Kjeang, "Mitigation of chemical membrane degradation in fuel cells: understanding the effect of cell voltage and iron ion redox cycle," *ChemSusChem,* vol. 8, no. 6, pp. 1072-1082, 2015.

[76] K. H. Wong and E. Kjeang, "In-situ modeling of chemical membrane degradation and mitigation in ceria-supported fuel cells," *Journal of the Electrochemical Society,* vol. 164, no. 12, p. F1179, 2017.

[77] A. Sadeghi Alavijeh, M.-A. Goulet, R. Khorasany, J. Ghataurah, C. a. L. M. Lim, E. Kjeang, G. Wang and R. Rajapakse, "Decay in mechanical properties of catalyst coated membranes subjected to combined chemical and mechanical membrane degradation," *Fuel cells,* vol. 15, no. 1, pp. 204-213, 2015.

[78] Y. Singh, F. P. Orfino, M. Dutta and E. Kjeang, "3D visualization of membrane failures in fuel cells," *Journal of Power Sources,* vol. 345, pp. 1-11, 2017.

[79] Y.-H. Lai, K. M. Rahmoeller, J. H. Hurst, R. S. Kukreja, M. Atwan, A. J. Maslyn and C. S. Gittleman, "Accelerated stress testing of fuel cell membranes subjected to combined mechanical/chemical stressors and cerium migration," *Journal of the Electrochemical Society,* vol. 165, no. 6, p. F3217, 2018.

[80] D. Ramani, Y. Singh, F. P. Orfino, M. Dutta and E. Kjeang, "Characterization of membrane degradation growth in fuel cells using X-ray computed tomography," *Journal of The Electrochemical Society,* vol. 165, no. 6, p. F3200, 2018.

[81] Y. Chen, Y. Singh, D. Ramani, F. P. Orfino, M. Dutta and E. Kjeang, "4D imaging of chemo-mechanical membrane degradation in polymer electrolyte fuel cells-Part 1: Understanding and evading edge failures," *Journal of Power Sources,* vol. 230674, p. 520, 2022.

[82] P. É. A. Melchy and M. Eikerling, "Physical theory of ionomer aggregation in water," *Physical Review E,* vol. 89, no. 3, p. 032603, 2014.

[83] P. É. A. Melchy and M. Eikerling, "Theory of fracture formation in a heterogeneous fibrillar membrane," *Journal of Physics: Condensed Matter,* vol. 27, no. 32, p. 325103, 2015.

[84] N. S. Khattra, M. El Hannach, K. H. Wong, M. Lauritzen and E. Kjeang, "Estimating the durability of polymer electrolyte fuel cell membranes using a fracture percolation model," *Journal of The Electrochemical Society,* vol. 167, no. 1, p. 013528, 2019.

[85] A. Kregar, M. Gatalo, N. Maselj, N. Hodnik and T. Katrasnik, "Temperature dependent model of carbon supported platinum fuel cell catalyst degradation," *Journal of Power Sources,* vol. 514, p. 230542, 2021.

[86] M. Pourbaix, Atlas of electrochemical equilibria in aqueous solutions, Elsevier, 1967.

[87] H. A. Baroody, D. B. Stolar and M. H. Eikerling, "Modelling-based data treatment and analytics of catalyst degradation in polymer electrolyte fuel cells," *Electrochimica Acta,* vol. 283, pp. 1006-1016, 2018.

[88] A. Kregar, G. Tavcar, A. Kravos and T. Katrasnik, "Predictive system-level modeling framework for transient operation and cathode platinum degradation of high temperature proton exchange membrane fuel cells," *Applied Energy,* vol. 263, p. 114547, 2020.

[89] H. S. Wroblowa and G. Razumney, "Electroreduction of oxygen: A new mechanistic criterion," *Journal of Electroanalytical Chemistry and Interfacial Electrochemistry,* vol. 69, no. 2, pp. 195-201, 1976.

[90] K. Schmidt-Rohr and Q. Chen, "Parallel cylindrical water nanochannels in Nafion fuel-cell membranes," *Nature materials,* vol. 7, no. 1, pp. 75-83, 2008.

[91] L. Rubatat, G. Gebel and O. Diat, "Fibrillar structure of Nafion: Matching Fourier and real space studies of corresponding films and solutions," *macromolecules,* vol. 37, no. 20, pp. 7772-7783, 2004.

[92] S. Zhurkov and V. Korsukov, "Atomic mechanism of fracture of solid polymers," *Journal of Polymer Science: Polymer Physics Edition,* vol. 12, no. 2, pp. 385-398, 1974.

[93] E. Sacher, "Effect of molecular motions on time-dependent fracture," *Journal of Macromolecular Science, Part B: Physics,* vol. 15, no. 1, pp. 171-181, 1978.

[94] A. C. Hansen and J. Baker-Jarvis, "A rate dependent kinetic theory of fracture for polymers," *International Journal of Fracture,* vol. 44, pp. 221-231, 1990.

[95] M. El Hannach, K. H. Wong, Y. Singh and E. Kjeang, "Correlation Between Crack Initiation and Chemical Decomposition in the Ionomer Membrane of Polymer Electrolyte Fuel Cells," in *Electrochemical Society Meeting Abstracts 230*, 2016.

[96] M. El Hannach, K. H. Wong, Y. Singh, N. S. Khattra and E. Kjeang, "Modeling of Coupled Mechanical and Chemical Degradation of the Ionomer Membrane in Polymer Electrolyte Fuel Cells," in *Electrochemical Society Meeting Abstracts 233*, 2018.

[97] A. Hansen and P. Hemmer, "Burst avalanches in bundles of fibers: Local versus global load-sharing," *Physics Letters A,* vol. 184, no. 6, pp. 394-396, 1994.

[98] P. Ahmadi and E. Kjeang, "Realistic simulation of fuel economy and life cycle metrics for hydrogen fuel cell vehicles," *International Journal of Energy Research,* vol. 41, no. 5, pp. 714-727, 2017.

[99] T. Gillespie, Fundamentals of vehicle dynamics, SAE international, 1992.

[100] P. Zihrul, I. Hartung, S. Kirsch, G. Huebner, F. Hasch{\'e} and H. A. Gasteiger, "Voltage cycling induced losses in electrochemically active surface area and in H2/air-performance of PEM fuel cells," *Journal of The Electrochemical Society,* vol. 163, no. 6, p. F492, 2016.

[101] N. Macauley, A. S. Alavijeh, M. Watson, J. Kolodziej, M. Lauritzen, S. Knights, G. Wang and E. Kjeang, "Accelerated membrane durability testing of heavy duty fuel cells," *Journal of the Electrochemical Society,* vol. 162, no. 1, p. F98, 2014.

[102] A. Mohammed and A. Abdullah, "Scanning electron microscopy (SEM): A review," *Proceedings of the 2018 International Conference on Hydraulics and Pneumatics—HERVEX, Băile Govora, Romania,* vol. 2018, pp. 7-9, 2018.

[103] S. J. Pennycook and P. D. Nellist, Scanning transmission electron microscopy: imaging and analysis, Springer Science, 2011.

[104] P. G. Corradini, F. I. Pires, V. A. Paganin, J. Perez and E. Antolini, "Effect of the relationship between particle size, inter-particle distance, and metal loading of carbon supported fuel cell catalysts on their catalytic activity," *Journal of Nanoparticle Research,* vol. 14, pp. 1-9, 2012.

[105] P. Ferreira, Y. Shao-Horn, D. Morgan, R. Makharia, S. Kocha and H. Gasteiger, "Instability of Pt/ C electrocatalysts in proton exchange membrane fuel cells: a mechanistic investigation," *Journal of the Electrochemical Society,* vol. 152, no. 11, p. A2256, 2005.

[106] M. Uchimura, S. Sugawara, Y. Suzuki, J. Zhang and S. S. Kocha, "Electrocatalyst durability under simulated automotive drive cycles," *Ecs Transactions,* vol. 16, no. 2, p. 225, 2008.

[107] S. S. Kocha, Electrochemical degradation: electrocatalyst and support durability, Academic Press Oxford, 2012, pp. 89-214.

[108] M. Shojayian and E. Kjeang, "Simulation of cathode catalyst durability under fuel cell vehicle operation--Effects of stack size and temperature," *Journal of Power Sources,* vol. 591, p. 233820, 2024.

[109] A. Pourahmadiyan, P. Ahmadi and E. Kjeang, "Dynamic simulation and life cycle greenhouse gas impact assessment of CNG, LNG, and diesel-powered transit buses in British Columbia, Canada," *Transportation Research Part D: Transport and Environment,* vol. 92, p. 102724, 2021.

[110] K. Chandler and B. Eudy, "Thunder power bus evaluation at sun line transit agency, prepared for the DOE," *Contract No. DOE/GO-102003-1786,* 2003.

[111] A. A. Pesaran, Y. O. Parent and D. Bharathan, "Non-CFC air conditioning for transit buses," *SAE transactions,* pp. 750-759, 1992.

[112] C. Wang, M. Ricketts, A. P. Soleymani, J. Jankovic, J. Waldecker and J. Chen, "Effect of carbon support characteristics on fuel cell durability in accelerated stress testing," *Journal of The Electrochemical Society,* vol. 168, no. 4, p. 044507, 2021.

[113] H. Sun, H. Liu and L.-J. Guo, "PEM fuel cell performance and its two-phase mass transport," *Journal of Power Sources,* vol. 143, no. 1-2, pp. 125-135, 2005.

[114] Y. Wang, S. J. Moura, S. G. Advani and A. K. Prasad, "Power management system for a fuel cell/battery hybrid vehicle incorporating fuel cell and battery degradation," *International Journal of Hydrogen Energy,* vol. 44, no. 16, pp. 8479-8492, 2019.

[115] S. G. Ji, H. C. Kwon, T.-H. Kim, U. Sim and C. H. Choi, "Does the Encapsulation Strategy of Pt Nanoparticles with Carbon Layers Really Ensure Both Highly Active and Durable Electrocatalysis in Fuel Cells?," *ACS Catalysis,* vol. 12, no. 12, pp. 7317-7325, 2022.

[116] M. Mazrouei Sebdani, E. Kjeang and H. Baroody, "Modeling and Simulation of the Mechanical Properties of Reinforced Fuel Cell Membranes," in *Electrochemical Society Meeting Abstracts 241*, 2022.

[117] C. G'sell, A. Dahoun, J. Hiver and C. Poinsot, "Creep and yield behaviour of semi-crystalline polyethylene in uniaxial tension," in *IUTAM Symposium on Micromechanics of Plasticity and Damage of Multiphase Materials: Proceedings of the IUTAM Symposium held in Sèvres, Paris, France, 29 August-1 September 1995*, Springer, 1996, pp. 75-82.

[118] A. Kusoglu, Y. Tang, M. H. Santare, A. M. Karlsson, S. Cleghorn and W. B. Johnson, "Stress-strain behavior of perfluorosulfonic acid membranes at various temperatures and humidities: Experiments and phenomenological modeling," *Journal of Fuel Cell Science and Technology,* vol. 6, no. 1, 2009.

[119] N. S. Khattra, S. Bhattacharya, M. V. Lauritzen and E. Kjeang, "Residual fatigue life modeling of fuel cell membranes," *Journal of Power Sources,* vol. 477, p. 228714, 2020.

[120] "The Weather Network," [Online]. Available: https://www.theweathernetwork.com/ca/weather/british-columbia/victoria.

[121] L. Eudy and M. Post, "Fuel Cell Buses in U.S. Transit Fleets: Current Status 2020," National Renewable Energy Laborator, 2021.

Appendix A. Performance loss due to membrane and cathode degradation

In this section, the performance loss due to cathode and membrane degradation processes will be compared. To this end, an AMDT conducted by the Reference [101] is assumed. This test was carried out at a constant voltage of 0.9 V, temperature of 85℃ and RH of 100%, and was finished after around 900 hours. The developed catalyst degradation model is employed to estimate the cathode degradation under the abovementioned conditions. Figure A1 shows the resulting ECSA loss and fraction of oxide coverage change with time. The observed ECSA loss is significantly smaller compared to the cases with potential cycling. The reason is attributed to the extensive oxide coverage formed over the platinum surface at high constant voltage (Figure A1b) which prevents substantial platinum degradation. Figure A1b indicates a constant large oxide coverage due to the constant voltage at the last stages of simulation.

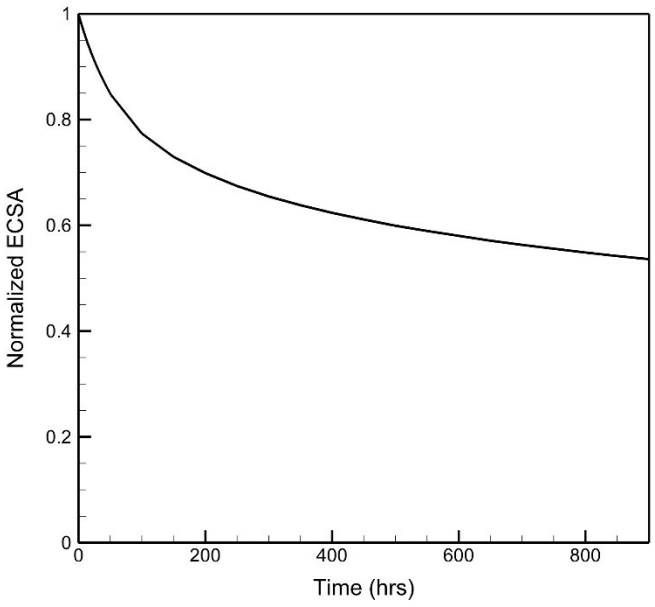

(a)

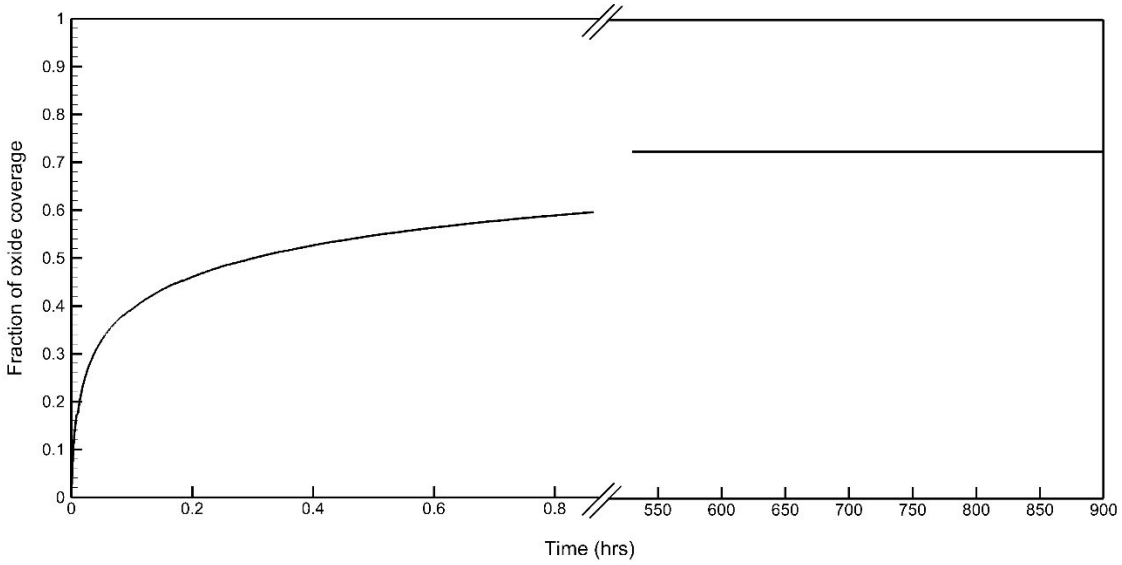

(b)

Figure A1: (a) ECSA degradation; (b) fraction of oxide coverage change with time at 0.9 V, 85℃ and 100% RH.

Figure A2 displays the measured polarization curves at BOL and EOT presented by [101]. The voltage loss obtained from this experiment is considered as the total voltage loss due to membrane and cathode catalyst degradation processes.

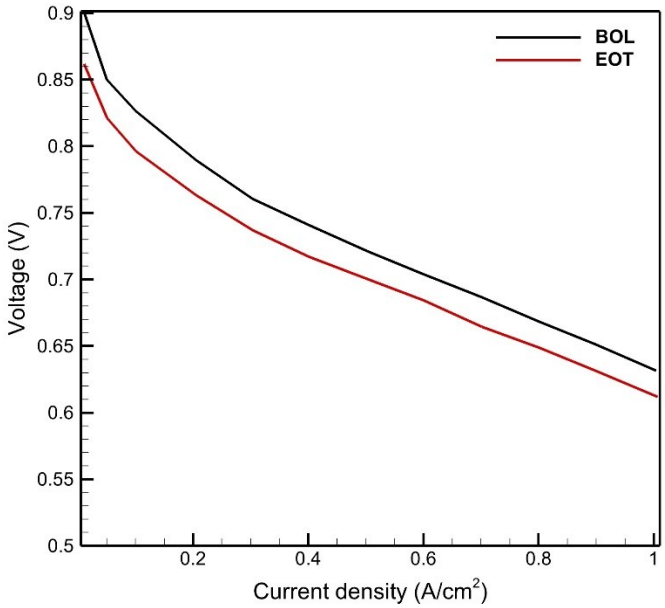

Figure A2: Polarization curves at BOL and EOT resulted from the AMDT [101].

The voltage drop calculated using the cathode degradation model is subtracted from the total voltage loss to find the contribution of membrane degradation to the performance loss. Figure A3 depicts the percentage of the membrane degradation contribution to the voltage loss at EOT for each current density.

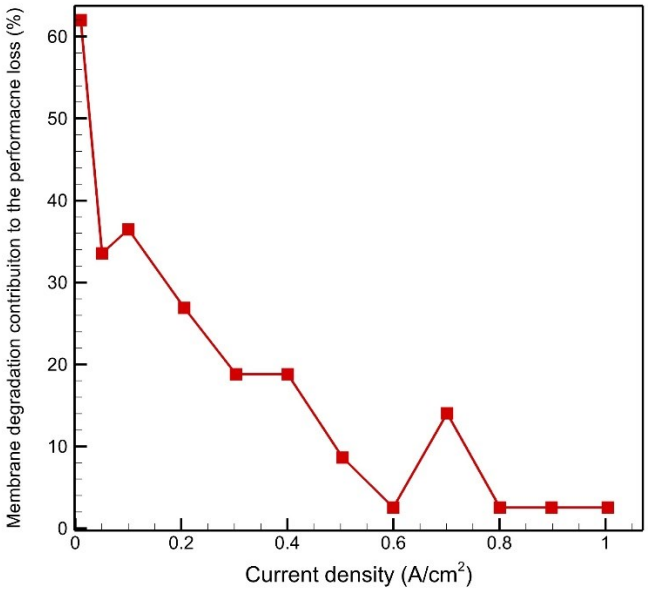

Figure A3: the percentage of the membrane degradation contribution to the voltage loss at EOT for the AMDT implemented at 0.9 V, 85℃ and 100% RH.

According to the Figure A3, the contribution of the membrane degradation to the performance loss is small especially for the higher current densities (greater than 0.3 A cm^{-2}). Higher voltages near OCV are mostly affected by the membrane degradation effects. It should be noted that these results are associate with the EOT which marks the end of life for membrane. During the experiment until the midlife, the membrane degradation effect on the performance loss even for the higher voltages is negligible, and the performance degradation is dominantly governed by the cathode degradation for a wide range of voltages [101].

Appendix B. The epoxy preparation for TEM images

A block of MEDIUM hardness can be obtained by using the following formula based on a batch of 10 grams without the flexibilizer, DER 736:

Table B1

	(medium)	(harder)	(softer)	(rapid)
ERL 4221	4.10g			
Diglycidyl ether of Polypropyleneglycol (DER® 736)	1.43g	0.95g	1.90g	
Nonenyl succinic anhydride (NSA)	5.90g			
Dimethylaminoethanol (DMAE)	0.1g			0.2g

A harder block can be produced by decreasing the DER® 736 component to 0.95 g in the above formula; a softer block by increasing the DER® 736 to 1.90 g.

Preparation:

Ensure precise measurement of the ingredients into a beaker. The quantities specified in the initial column are intended for firm blocks. Adjust the DER® 736 to 0.95g for harder blocks, and increase it to 1.90g for softer blocks. Increase the DMAE For a rapid cure. Add the catalyst (dimethylaminoethanol) last, after thoroughly blending the other components. If bubbles prove problematic, resolve the issue by placing the beaker into a desiccator under a gentle vacuum.

Use either ethyl alcohol, acetone, tert-butyl alcohol, isopropyl alcohol, or propylene oxide for dehydration. When using ethanol and propylene oxide, exercise caution to eliminate all propylene oxide when transferring the specimen, as this volatile liquid can quickly evaporate, leaving the specimen dry. For infiltration, replace the solvent with a 1:1 mixture of solvent and

embedding medium, gently mixing for at least 30 minutes at room temperature. Subsequently, drain or pipette out the 1:1 mixture and substitute it with the 100% complete embedding medium for an additional 30-minute infiltration, preferably uncovered to allow any remaining solvent to evaporate. A second 30-minute infiltration with the 100% embedding medium is advisable. Transfer specimens to clean, dry capsules, which are then filled with fresh embedding medium. Achieve overnight polymerization at 60ºC. For rapid polymerization in 3 hours at 70ºC, increase the amount of catalyst (DMAE) to 0.2g in the formula mentioned above.

References:

Spurr, AR, J Ultrastructure Research 26, 31 (1969)

Spurr, AR & Harris, WM, Am. J Botany, 55 (1968)

Seligman, AM, et al, J Histochem and Cytochem, 15,1 (1967)

Richardson, KL, et al, Stain Technology, 35, 313 (1960)

Nemeth, F, Proc. 30th Ann Electron Micro Soc Amer, 697, L.A. (1972)